BEAM BREAKUP INSTABILITY AND COHERENT SYNCHROTRON RADIATION LIMITS OF THE PARTICLE ACCELERATOR CBETA

A Dissertation

Presented to the Faculty of the Graduate School

of Cornell University

in Partial Fulfillment of the Requirements for the Degree of

Doctor of Philosophy

by

William Lou

May 2020

BEAM BREAKUP INSTABILITY AND COHERENT SYNCHROTRON RADIATION LIMITS OF THE PARTICLE ACCELERATOR CBETA

William Lou, Ph.D.

Cornell University 2020

The construction of Cornell BNL Energy-Recovery-Linac Test Accelerator (CBETA) was completed at Cornell University's Wilson Laboratory in 2019. CBETA is designed to accelerate electrons from 6 MeV to 150 MeV in four linac passes using a single Fixed Field Alternating gradient (FFA) return beamline accepting all energies from 42 to 150 MeV. Energy recovery is achieved by decelerating the beam within the Superconducting Radio Frequency (SRF) cavities, in which the beam returns energy to the electromagnetic field. Energy recovery allows CBETA to produce a beam current much higher than with conventional storage rings.

This thesis focuses on two important limits of CBETA: the beam current limit due to Beam Breakup (BBU) instability and the bunch charge limit due to Coherent Synchrotron Radiation (CSR) effects. For BBU, elementary theories are revisited to benchmark the simulation codes. Additional theory regarding the scaling law of the threshold current and the effect of chromaticity are also investigated. For CSR, a new "2-bend" theory has been developed by extending the conventional 1-bend theory using the Lienard-Wiechert formula. The new theory is essential to describe CSR wake propagation when magnets are located close to each other, as in CBETA. These new theories could benefit designs and researches of future ERLs. For both topics, extensive simulations have been performed using the software developed by Cornell University, Bmad.

BIOGRAPHICAL SKETCH

William Lou was born in Los Angeles in January 1991. After being raised up in Taiwan for 15 years, William immigrated to Vancouver, where he completed high school and his undergraduate degree at University of British Columbia. With a major in Engineering Physics and a minor in honour mathematics, William graduated in 2014 and moved to Ithaca to pursue a Ph.D. degree in physics at Cornell University.

This document is dedicated to all ERL designers and users.

ACKNOWLEDGEMENTS

I would like to thank the entire CBETA team, especially three particular individuals. The first person is my advisor professor Georg Hoffstaetter, who provided the research opportunities and financial support. The second person is Christopher Mayes, who provided academic knowledge and professional guidance. The third person is David Sagan, who provided technical assistance with simulation software $Bmad$. Honorable mentions include Dejan Trbojevic, Scott Berg, Adam Bartnik, Colwyn Gulliford, and Kirsten Deitrick.

TABLE OF CONTENTS

LIST OF TABLES

LIST OF FIGURES

CHAPTER 1

INTRODUCTION

1.1 ERL and CBETA

Energy recovery linacs (ERLs) open up a new regime of beam parameters with large current and simultaneously small emittances, bunch lengths, and energy spread. The Cornell BNL ERL Test Accelerator (CBETA) is the first accelerator constructed to analyze the potential of multi-turn ERLs with superconducting SRF accelerating cavities [1]. New beam parameters of ERLs allow for new experiments such as nuclear and high energy colliders, electron coolers, internal scattering experiments, X-ray sources or Compton backscattering sources for nuclear or X-ray physics [2][3][4]. By recirculating charged beams back into the accelerating cavities, energy can be recovered from the beams to the electromagnetic fields of the cavities. Energy recovery allows an ERL to operate at a much higher current than conventional linacs, where the current is limited by the power consumption by the cavities. While electron beams recirculate for thousands of turns in storage rings, they travel only a few turns in an ERL before being dumped. The short circulation time allows beam emittances to be as small as for a linac. The potentials for high beam current with simultaneously low emittances allows an ERL to deliver unprecedented beam parameters.

CBETA has been constructed at Cornell University's Wilson Laboratory. This is a collaboration with BNL, and will be the first multipass ERL with a Fixed Field Alternating (FFA) lattice. It serves as a prototype accelerator for electron coolers of Electron Ion Colliders (EICs), and the EIC project proposed at BNL will benefit from this new accelerator [5]. Fig. 1.1 shows the design layout of

CBETA. At full operation, CBETA is a 4-turn ERL with maximum electron beam energy of 150 MeV. This has been achieved by first accelerating the electron beam to 6 MeV by the injector (IN). The beam is then accelerated by the Main Linac Cryomodule (MLC) cavities (LA) four times to reach 150 MeV, then the beam is decelerated four times down to 6 MeV before stopped (BS). The beam passes through the MLC cavities for a total of eight times, each time with an energy gain of $\pm$36 MeV. The field energy in the cavities is transferred to the beam during acceleration, and recovered during deceleration. Transition from acceleration to deceleration is achieved by adjusting the path-length of the forth recirculation turn to be an odd multiple of half of the RF wavelength. The path-length of all the other turns is exactly an integer multiple of the RF wavelength. CBETA can also operate as a 3-turn, 2-turn, or 1-turn ERL with properly adjusted configuration. In July 2019, 1-turn energy recovery was achieved with a recovery efficiency of 99.6% up to $8\,\mu A$ [6]. In December 2019, 4-turn recirculation was achieved.

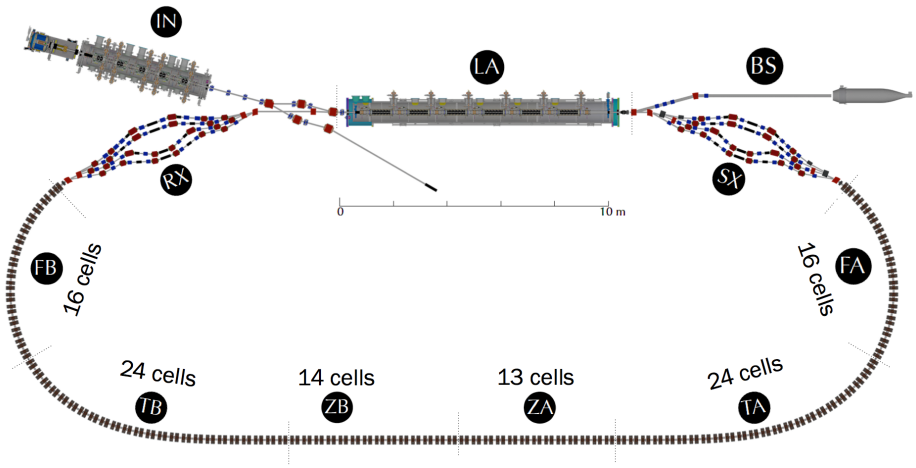

Figure 1.1: Layout of CBETA. The sections labeled (IN) and (LA) are the injector and MLC cavities respectively. Sections (FA), (TA), (ZA), (ZB), (TB), and (FB) form the FFA beamline which can accommodate four recirculating orbits with energy ranging from 42 MeV to 150 MeV. Sections (SX) and (RX) are splitters which control the path-length of each recirculation pass.

1.2 Beam Breakup Instability

Unlike conventional storage rings with non-superconducting cavities, the beam current in ERLs is no longer limited by the power consumption in the cavities. However, there will be new, higher limits to the current. These are Higher Order Modes (HOMs) heating and the recirculative Beam Breakup (BBU) instability. BBU occurs in recirculating accelerators as the recirculated beam bunches interact with the HOMs in the accelerating cavities. The most relevant HOMs for BBU are the dipole HOMs which give a transverse kick to the bunches. The off-orbit bunches return to the same cavity and excite the dipole HOMs which can kick the subsequent bunches further in the same direction. The effect can build up and can eventually result in beam loss. With a larger beam current the effect becomes stronger, so BBU is a limiting factor on the maximum achievable current, called the threshold current I_{th}. With multiple recirculation passes, bunches interact with cavities for multiple times, and the I_{th} can significantly decrease [7]. The low and high target currents of CBETA are 1 mA and 40 mA respectively, for both the 1-turn mode and 4-turn mode. Simulations are required to check whether the I_{th} is above these target values.

1.3 Coherent Synchrotron Radiation

Synchrotron radiation occurs when an electron traverses a curved trajectory, and the radiation emitted can give energy kicks to the other electrons in the same bunch. While the high frequency components of the radiation spectrum tend to add up incoherently, the low frequency components, with wavelength on the order of the bunch length, can add coherently. These are termed incoher-

ent and coherent synchrotron radiation respectively (ISR and CSR). While the total intensity for ISR scales linearly with the number of charged particles (N_p), it scales as N_p^2 for CSR.

For an ERL which aims for high beam quality like CBETA, CSR can pose detrimental effects on the beam bunches, including energy loss, increase in energy spread, and potentially the micro-bunching instability [24]. It is therefore important to run CSR simulations for CBETA, and investigate potential ways for mitigation.

1.4 Orbit Correction and Tolerance Study

Orbit correction simulation allows us to find the tolerance of an accelerator lattice subjected to various errors. Common error sources include non-ideal magnet positioning and alignment, undesired multipole field strengths, and offsets of Beam Position Monitors (BPMs). In order to fix the altered orbits, dipole kickers as correctors are allocated throughout the lattice. A common approach for orbit correction is the Singular Value Decomposition (SVD) optimization, which calculates the linear response matrices between the BPMs and correctors, and minimizes the residual orbit in the least square sense [35].

In CBETA there are BPMs and correctors located within the FFA beamline and all the splitter lines. Since there are four coexisting orbits in the FFA, the correction scheme must aim to correct all four of them simultaneously. As the error magnitudes increase, the beam size and emittance after correction could still undesirably increase. Our goal is to find the "individual limit" of each error type beyond which the increases become unacceptable. Typically this limit is

reached before the orbits become un-correctable. Similarly we can also find the "combined limit" of various errors. The definition of these limits and further details are included in the orbit correction chapter.

1.5 Bmad

Cornell University has developed a simulation software called Bmad to model relativistic beam dynamics in customized accelerator lattices [8]. Having been developed to model the storage ring CESR at Cornell, Bmad has also been used to design and optimize the CBETA lattice.

Most simulation results presented in this thesis come from Bmad. For orbit correction, Bmad can readily calculate the response matrices from the correctors and BPMs assigned by the users. The required SVD optimizer has also been implemented in Bmad. With the ability to track charged bunches through a lattice, Bmad has subroutines established to specifically simulate BBU and CSR effects. While BBU simulation tracks a beam of bunches through recirculated cavity(s) and calculates the HOM voltage(s) over time, CSR simulation tracks one bunch with a large number of particles and calculates the CSR energy kicks within the bunch for every time step. Both simulations involve several parameter choices, and can be computationally intensive. Further simulation details are included in the respective chapters of BBU and CSR.

CHAPTER 2

CBETA

Fig. 1.1 shows the main sections of CBETA. This chapter briefly describes the sections which are important to the topics in this thesis, including the MLC cavities, FFA beamline, and the splitter sections. The detailed descriptions on all the components can be found in [1].

2.1 MLC cavities

Fig. 2.1 shows the CBETA MLC, which comprises of six 7-cell SRF cavities with a fundamental frequency of 1.3 GHz. Fig 2.2 shows the design of one such cavity.

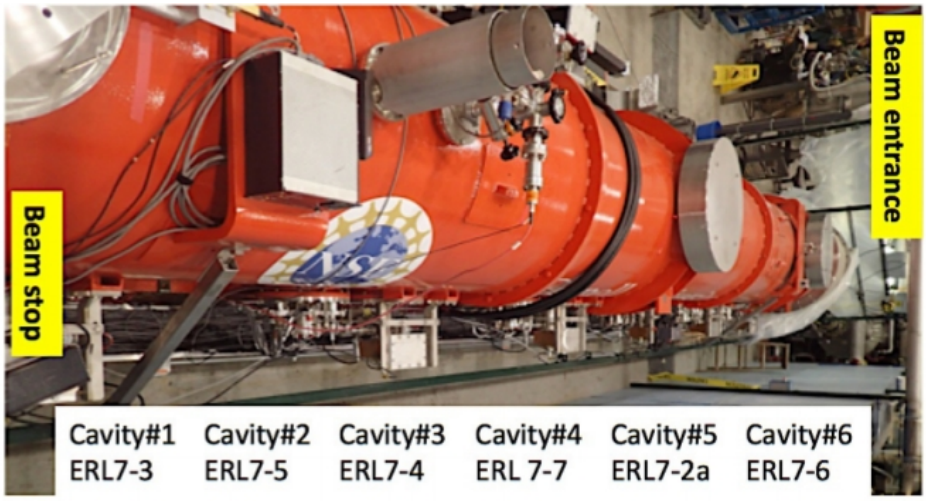

Figure 2.1: The CBETA MLC during commissioning in May 2017. Image credit to [5].

Each cavity is powered via an individual solid state amplifier, with an average power of 5 kW per amplifier. To enable high current ERL operation, HOM absorbers are placed in between the cavities to suppress the HOMs down to typically $Q \sim 10^4$. Details on the HOM spectra are discussed in the BBU chapter.

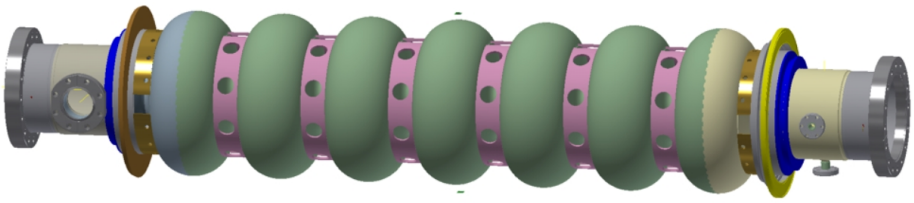

Figure 2.2: Design of one 7-cell cavity in the MLC. Image credit to [34].

2.2 FFA beamline

The FFA beamline consists of the FFA arcs (FA and FB), the transition sections (TA and TB), and the straight sections (ZA and ZB). Each of these sections consists of multiple FFA cells, and each cell comprises of one pure focusing quadrupole magnet (QF) and one defocusing quadrupole magnet with an additional dipole component (BD). In reality the magnets are permanent Halbach type magnets with primarily dipole and quadrupole field components in the good field region [30]. Fig. 2.3 shows the orbits of the four design energies inside the first half of the FFA beamline. Section FA consists of 16 periodic cells (See Fig. 2.4), and the orbits and beam optics and also periodic. The periodicity breaks at the transition section TA, and all four orbits reach zero value at the straight section ZA.

Fig. 2.5 shows the cross sections of the QF and BD magnets in FA. The detailed calculation of the magnetic fields can be found in [30]. Because the four orbits have different horizontal offsets, they see different equivalent dipole fields. Note that the FFA lattice accepts beams with a continuous range of energies, not just the four design energies. Bmad simulations show that the acceptable energy ranges from 38 MeV to 240 MeV.

The FFA beamlinie plays an important roles in all topics of the thesis. For

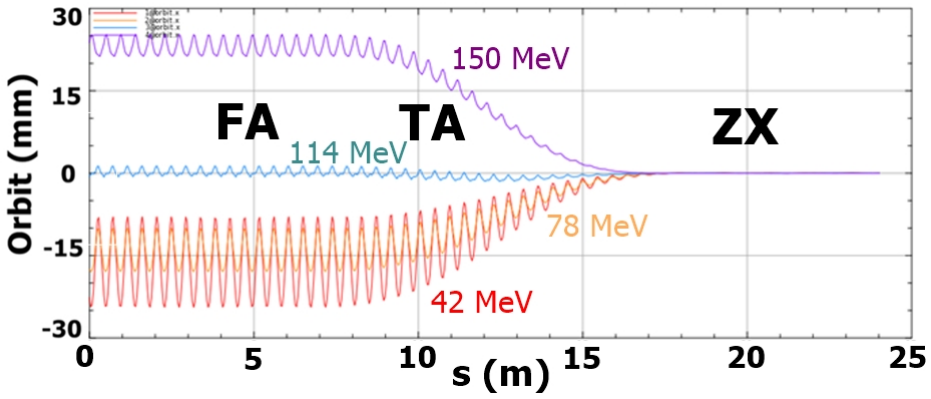

Figure 2.3: (Color) The orbits of the four design energies inside the first half of the FFA beamline, including FA, TA, and ZA. The second half (not included) has approximately mirrored orbits and optics.

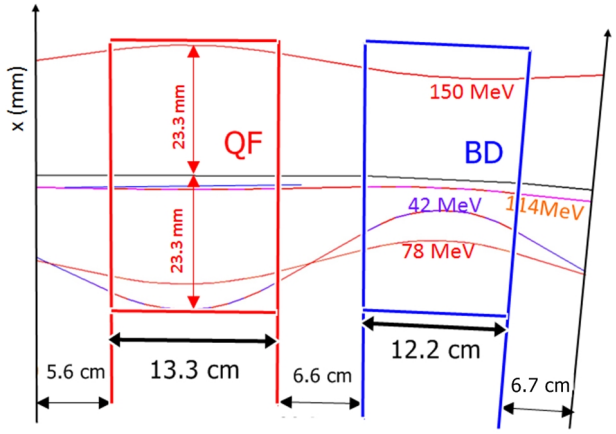

Figure 2.4: The top view of one FA cell showing the four orbits with energy ranging from 42 MeV to 150 MeV. The cell bends the reference geometry by 5 degrees.

BBU instability, the threshold current depends on the beam optics and the natural chromaticities of the four orbits. For CSR, the bunches undergo the most curved trajectories in the FA and FB section, which contribute significant CSR effects. For orbit correction, majority of the BPMs and orbit correctors are located in the beamline.

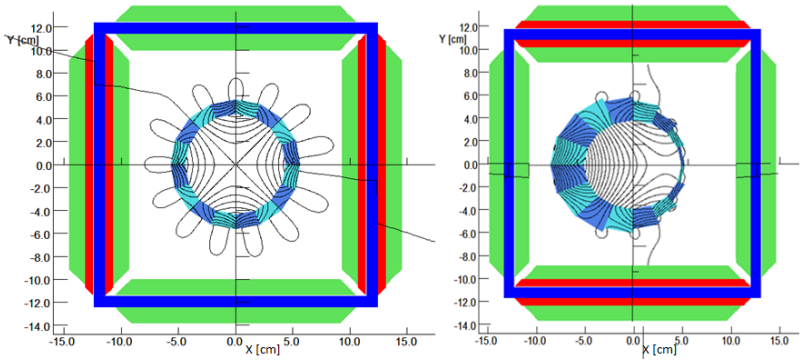

Figure 2.5: (Color) The cross sections of the QF, a pure focusing Halbach quadrupole magnet (left), and the BD, a defocusing quadrupole magnet with a dipole component (right) in the FA section. Both magnets have window framed electromagnets as correctors, which can provide a normal dipole (red areas) and a normal quadrupole (green areas) field.

2.3 Splitter sections

The two splitter sections SX and RX consist of non-permanent dipole and quadrupole magnets. Fig. 2.6 shows the design layout of the SX section. To distinguish between the four energy passes, the four lines in SX (RX) are named S1 (R1) for 42 MeV, S2 (R2) for 78 MeV, S3 (R3) for 114 MeV, and S4 (R4) for 150 MeV. One primary function of the splitters is to adjust the recirculation path length of each pass. This allows the operators to switch between the 1-turn, 2-turn, 3-turn, and 4-turn mode of CBETA.

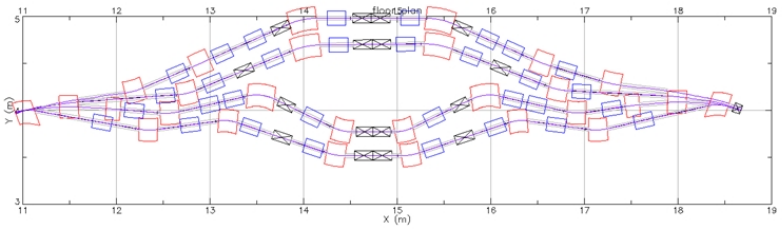

Figure 2.6: The top view of the SX splitter section. The red blocks are dipole magnets, and the blue ones are quadrupole magnets. From bottom to top, the four lines are named S1, S2, S3, and S4.

During the design phase of CBETA, the orbits and beam optics in the MLC and FFA beamline are fixed first. Therefore, another primary function of the splitters is to steer the orbits and match the optics of the four beams between the MLC and FFA. Each splitter line has 8 quadruple magnets, and for each energy pass there are 6 optical parameters to be matched to: $\beta_x, \alpha_x, \beta_y, \alpha_y, \eta_x$, and η'_x (Twiss parameters and dispersion). Fig. 2.7 shows an optical solutions found for the S4 line using a numerical optimizer in Bmad.

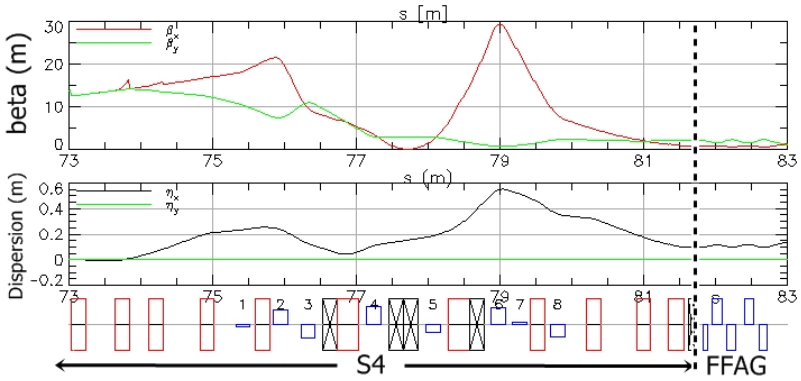

Figure 2.7: An example S4 splitter line configuration with optics matched into the FFA arc using 8 quadrupole magnets.

Another important quantity to be concerned is the r_{56} contribution from the FFA beamline. For each recirculation pass to be isochronous, we need the total r_{56} to be zero. This requires the r_{56} contribution from the SX and RX lines to cancel the FFA contribution for each of the four design energies. For instance, the r_{56} contribution from the FFA of the 42 MeV orbit is -19.9 mm, so S1 and R1 together need to contribute +19.9 mm. This adds one extra constraint on the optics matching for each splitter line, and therefore increases the difficulty to find an optical solution. A few quadrupole magnets with greater gradient (20 T/m) are sometimes required.

In terms of the topics in this thesis, the splitter sections are important to orbit correction and BBU instability. Chapter IV will show that the freedom in vary-

ing beam optics allows potential improvement of the BBU threshold current.

2.4 4-turn design optics and beam tracking

Fig. 2.8 shows the full beam optics of the 4-turn lattice. The beta functions and dispersion are computed about the design particle. The transverse beam sizes and bunch length come from tracking a "GPT beam" of 100k particles starting from the end of the LINAC pass 1 (42 MeV). The GPT beam comes from GPT tracking which accounts for space charge effect at low energy, up to 42 MeV. The phase space distributions and further details can be found in the CSR chapter.

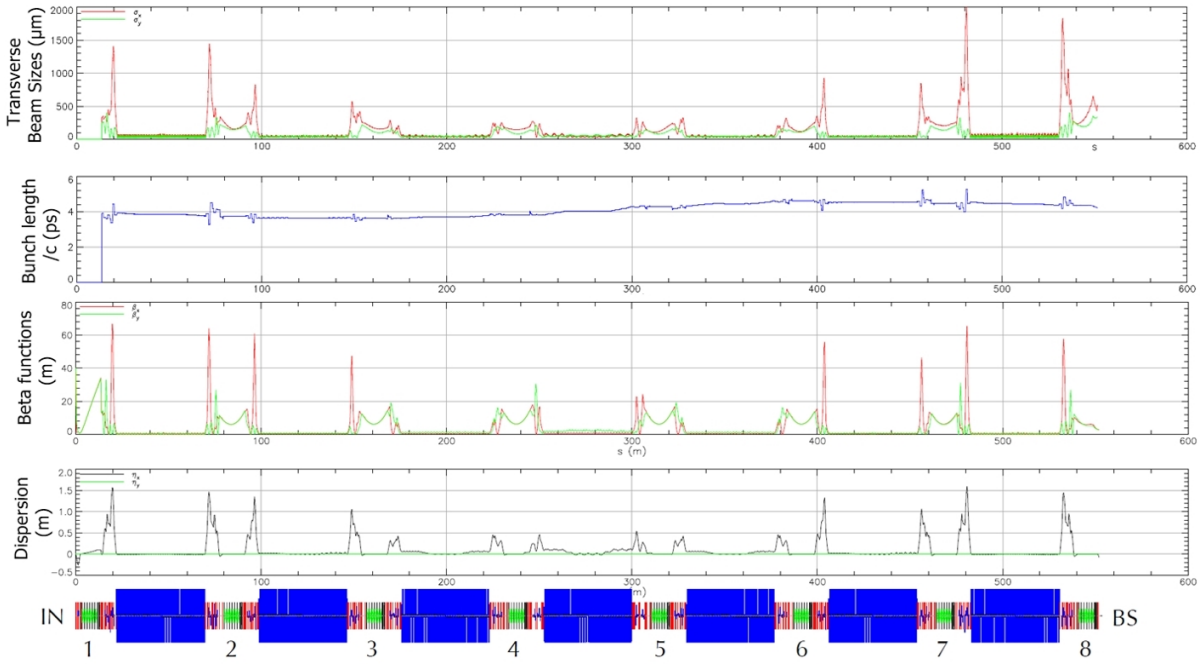

Figure 2.8: The beam optics of the full 4-turn lattice.

CHAPTER 3

BEAM BREAKUP INSTABILITY

3.1 BBU theory V.S BMAD Simulation

We will first revisit the general BBU theory developed in [7] and [17] to check the validity of BMAD simulations by comparing the results to the theory predictions. Benchmarking with numerical code has been performed in [7] for the most elementary BBU configuration (one dipole-HOM with one recirculation) using the recirculation arc time t_r as the variable. However, CBETA is a multi-pass ERL with multiple cavities. To ensure Bmad simulation results are representative, we also benchmark the code with more complicated configurations with various t_r. This has not been done in previous publications. Furthermore, by using similar lattice and HOM parameters across the configurations, one could compare the effect on the I_{th} in a consistent fashion. We believe these benchmarking results will be important to CBETA as well as future multi-pass ERLs which concern BBU.

We will focus on four configurations (cases) of which analytic formulas for I_{th} are available from [7] and [17]:

Case A: One dipole-HOM with $N_p = 2$,

Case B: One dipole-HOM with $N_p = 4$,

Case C: One dipole-HOM in two different cavities with $N_p = 2$, and

Case D: Two polarized dipole-HOMs in one cavity with $N_p = 2$.

Since the theory assumes thin-lens cavities, it is inaccurate to benchmark with the CBETA lattice whose cavities are each 1 m long. Instead we make a simple lattice with only thin-lens cavities and a recirculation arc with fixed optics. The following subsections compare the simulation results to theoretical formulas for the four cases.

3.1.1 One dipole-HOM with $N_p = 2$

Case A is the most elementary case for BBU. Assuming that the injected current I_0 consists of a continuous stream of bunches with a constant charge and separated by a constant time interval t_b, then the time-dependent HOM voltage $V(t)$ must satisfy, for any positive integer n, the recursive equation [7]:

$$V(nt_b + t_r) = I_0 \frac{e}{c} t_b T_{12} \sum_{m=0}^{\infty} W(mt_b) V([n-m]t_b), \tag{3.1}$$

in which $W(\tau)$ is the long range wake function characterized by the HOM parameters:

$$W(\tau) = \left(\frac{R}{Q}\right)_\lambda \frac{\omega_\lambda^2}{2c} e^{-(\omega_\lambda/2Q_\lambda)\tau} \sin(\omega_\lambda \tau). \tag{3.2}$$

All the related symbols are listed in Table 3.1, which closely follows the nomenclature used in [7]. The bunches arrive in the cavity at times nt_b, where they receive a transverse kick proportional to $V(nt_b)$, which then describes the transverse offset of successive bunches in the return loop. The Fourier transform

$$\tilde{V}^{\Sigma}(\omega) = t_b \sum_{n=-\infty}^{\infty} V(nt_b) e^{i\omega n t_b} \tag{3.3}$$

is zero for every ω except when the following dispersion relation is satisfied:

$$\frac{1}{I_0} = D(\omega), \tag{3.4}$$

$$D(\omega) = \frac{e}{c} t_b T_{12} e^{i\omega n_r t_b} w(\delta, \omega). \tag{3.5}$$

Symbol	SI Unit	Definition or Meaning
e	C	Elementary charge
c	m/s	Speed of light
t_{RF}	s	Fundamental RF period
t_b	s	Injected bunch time spacing ($> t_{\text{RF}}$)
t_r	s	Recirculation arc time (typically $> t_b$)
n_r	-	$n_r = \text{Top}[t_r/t_b]$, integer
δ	-	$\delta = (t_r/t_b - n_r) \in [0, 1)$ For an ERL $\delta \approx 0.5$
ω_λ	rad/s	HOM radial frequency
$(R/Q)_\lambda$	Ω	normalized HOM Shunt Impedance
Q_λ	-	HOM quality factor
T_{12}	s/kg	The T_{12} element of the transfer matrix of the recirculation arc
$W(\tau)$	V/mC	Long range wake function (see Eq. (3.2))
$w(\delta, \omega)$	V/mC	Sum over all wakes (see Eq. (3.6))
I_0	A	Measured current at the injector
ϵ	-	$\epsilon = (\omega_\lambda / 2Q_\lambda) t_b$
κ	CsΩ/m^2	$\kappa = t_b (e/c^2)(R/Q)_\lambda (\omega_\lambda^2/2)$

Table 3.1: A list of important quantities in the elementary BBU theory (one dipole-HOM, $N_p = 2$). ϵ is a measure of HOM decay in the time scale of t_b.

The function $w(\delta, \omega)$ sums the contribution of all the long range wakes in the frequency domain:

$$w(\delta, \omega) \equiv \sum_{n=0}^{\infty} W([n + \delta] t_b) e^{i\omega n t_b}. \tag{3.6}$$

As a current, I_0 is a real number, and for a fixed I_0 there is a set of complex values of ω which satisfy Eq. (3.5). For a small I_0 the voltage is stable, which means all the ω values have a negative imaginary part. If we keep increasing I_0, eventually instability will occur due to great excitement. This is reflected by the ωs that have positive imaginary parts. At the onset of instability, one of the ω is crossing the real axis (i.e. is real), and the corresponding current I_0

is then the threshold current I_{th}. While it's difficult to find the ω values for a given I_0, it's easy to compute $D(\omega)$ given a real ω. Most values computed will be complex and therefore correspond to an unphysical I_0. The largest real value of $D(\omega)$ determines the I_{th}. Due to the periodicity and symmetry in Eq. (3.5), it is sufficient to check ω in just $[0, \pi/t_b)$ or any equivalent interval. Mathematically this can be written as:

$$\frac{1}{I_{\text{th}}} = \max_{\omega}[D(\omega),\ D(\omega) \in \Re,\ \omega \in [0, \pi/t_b)]. \tag{3.7}$$

Eq. (3.5), combined with Eq. (3.7), is called the "general analytic formula" to determine the I_{th} for case A. For a representative comparison between theory and simulation, we check how I_{th} varies with t_r while holding t_b constant. The matrix element T_{12} and the HOM properties are also held constant. Fig. 3.1 shows the comparison result. Clearly BMAD's simulation agrees well with the general analytic formula, in both the regions with a high I_{th} (the crest) and low I_{th} (the trough).

If the HOM decay is insignificant on the time scale of t_b ($\epsilon \ll 1$), then Eq. (3.5) can be simplified by linearization in small ϵ. We call the resulting formula the "linearized analytic formula":

$$D(\omega) = -\frac{\kappa}{2}\frac{e^{i\omega t_r}T_{12}}{(\omega - \omega_\lambda)t_b + i\epsilon}. \tag{3.8}$$

Similar to the general formula, the linearized formula does not provide a closed form for I_{th}, so we still need to apply Eq. (3.7) to find the I_{th} as the smallest real I_0 over $\omega \in [0, \pi/t_b)$.

The usefulness of the linearized formula will be shown when $N_p > 2$. On the other hand, if the HOM decay is insignificant also on the recirculation time scale ($n_r\epsilon \ll 1$), then the formula can be further simplified into the "approximate analytic formula":

$$I_{\text{th}} = \begin{cases} -\frac{\epsilon}{\kappa}\frac{2}{T_{12}\sin(\omega_\lambda t_r)} & \text{if } T_{12}\sin(\omega_\lambda t_r) < 0 \\ \frac{2}{\kappa|T_{12}|}\sqrt{\epsilon^2 + (\frac{t_b}{t_r})^2 \times \text{minmod}(\omega_\lambda t_r, \pi)} & \text{otherwise,} \end{cases} \tag{3.9}$$

in which

$$\text{minmod}(x, y) = \min[\text{mod}(x, y), y - \text{mod}(x, y)]. \tag{3.10}$$

It is worth checking the applicability of the linearized and the approximate formula. This has been done in [7] for a case with $\epsilon = 0.00048$ and $n_r = 6$ to 7. Their result shows great agreement with the two non-general formulas in the trough region, but not in the crest region. Here we test a new case with $\epsilon = 0.024$ and $n_r = 2$ to 3, and the results are plotted together on Fig. 3.1.

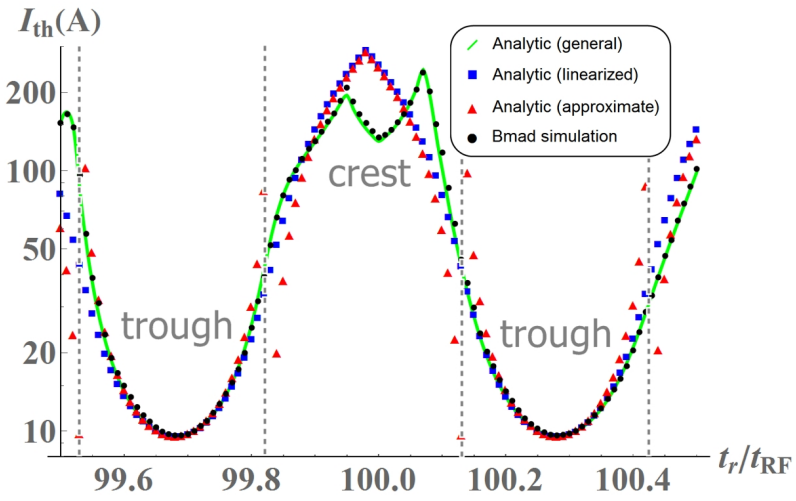

Figure 3.1: (Color) Comparison of the I_{th} obtained from different analytic formulas and BMAD simulation for $N_p = 2$. Parameters used: $ct_{\text{RF}} = 0.5\text{m}$, $t_b = 50t_{\text{RF}}$, $\omega_\lambda/2\pi = 1$ GHz, $Q_\lambda = 100$, $(R/Q)_\lambda = 10^4\Omega$, $T_{12} = -10\text{m}/(1\text{GeV}/c)$.

We again observe that the linearized formula agrees well with the general formula in the trough region, but the approximate formula agrees well only in a smaller region around the minimum of the trough. The inaccuracy of the approximate formula in the trough region comes from the increased value of

$n_r\epsilon$. With HOM dampers, Q_λ is typically on the order of 10^4, so for an ERL with continuous wave operation ($t_b = 2t_{\text{RF}}/N_p$, filling all the RF buckets), $\epsilon \ll 1$ is usually guaranteed. However, n_r (the harmonic number of an ERL, 343 for CBETA) can be a large number depending on the recirculation lattice, so $n_r\epsilon \ll 1$ is not guaranteed. This means the approximate formula needs to be applied with caution. Note that the top case in Eq. (3.9) corresponds to the I_{th} in the trough region, and can be rewritten as:

$$I_{\text{th}} = \frac{-2c^2}{e(R/Q)_\lambda Q_\lambda \omega_\lambda} \frac{1}{T_{12}\sin(\omega_\lambda t_r)}. \tag{3.11}$$

This formula has been derived in several works regarding BBU [18][19][20]. Despite its limited applicability, the formula gives us insight on how to avoid a low I_{th}. Besides suppressing the HOM quality factor Q_λ, one can also adjust the recirculation time to avoid $\sin(\omega_\lambda t_r) \approx +1$ (or -1) when T_{12} is negative (or positive). Theoretically I_{th} can be infinite by making $T_{12} = 0$. Unfortunately this can not be achieved in general with multiple cavities and $N_p > 2$, since the T_{12} between each pair of multipass cavities all needs to be zero. In reality the T_{12} also depends on the length of the cavity, which will be discussed in section III-E. The strategies to improve the I_{th} in general will be covered in section V.

3.1.2 One dipole-HOM with $N_p = 4$

In case A ($N_p = 2$) we see that three analytic formulas exist: the general, linearized, and approximate formula. For a more general case with one dipole-HOM yet $N_p > 2$, the general formula involves finding the maximum eigenvalue of a complex matrix [7]. For accurate calculation this requires a scan over ω at very small steps, and is often numerically difficult. Therefore we will apply

the linearized formula instead of the general formula. Similar to Eq. (3.8), the linearized formula is [7]:

$$D(\omega) = -\frac{\kappa}{2}\frac{1}{(\omega-\omega_\lambda)t_b + i\epsilon}\sum_{J=1}^{N_p}\sum_{I=J+1}^{N_p} e^{i\omega(t_I - t_J)}T^{IJ}, \tag{3.12}$$

in which I and J are the cavity pass index, $(t_I - t_J)$ is the recirculation time from pass J to I, and T^{IJ} is the corresponding T_{12} matrix element. To find the I_{th} we again apply Eq. (3.7), and no complex matrix is involved. The approximate formula also exists, but works only for the "trough regions" in which $\sum_{J=1}^{N_p}\sum_{I=J+1}^{N_p}\sin(\omega(t_I - t_J))T^{IJ} \le 0$:

$$I_{\text{th}} = \frac{-2c^2}{e(R/Q)_\lambda Q_\lambda \omega_\lambda}\frac{1}{\sum_{J=1}^{N_p}\sum_{I=J+1}^{N_p}\sin(\omega_\lambda(t_I - t_J))T^{IJ}}. \tag{3.13}$$

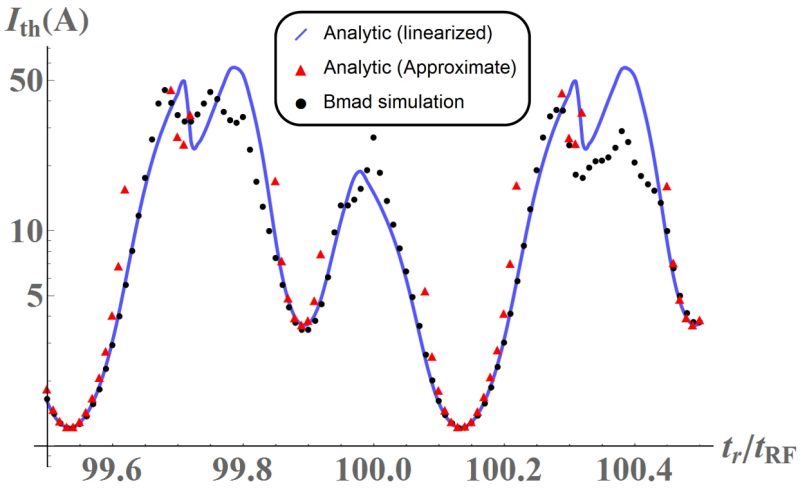

Figure 3.2: (Color) Comparison of the I_{th} obtained from the linearized formula and BMAD simulation for $N_p = 4$. Parameters used are the same as in Fig. 3.1, with $T_{12} = T^{IJ}$ and $t_r = t_I - t_J$ for any $I = J + 1$. The trough regions are where the approximate formula (red triangles) is evaluated.

Fig. 3.2 shows the comparison between BMAD simulation and the two analytic formulas. In contrast to the case with $N_p = 2$ (Fig. 3.1), we now have three instead of one trough regions in one period. The number, depth, and location of the troughs depend on the signs and magnitudes of T^{IJ}, or the optics of multiple recirculation passes. We again observe great agreement between simulation

and the linearized formula at the trough regions, and the approximate formula agrees well only around the the minimums.

3.1.3 One dipole-HOM in two different cavities with $N_p = 2$

The complexity of this case comes from the interaction between the two HOMs via different recirculation passes. Fig. 3.3 shows all the possible ways the HOMs excite themselves and each other. For example, the HOM of cavity 1 (V_1) can excite itself via recirculation (via the green arrow labeled T_{11}^{21}). It can also excite the HOM of cavity 2 (V_2) in the same pass (via the blue arrows labeled T_{21}^{11} for pass 1 and T_{21}^{22} for pass 2).

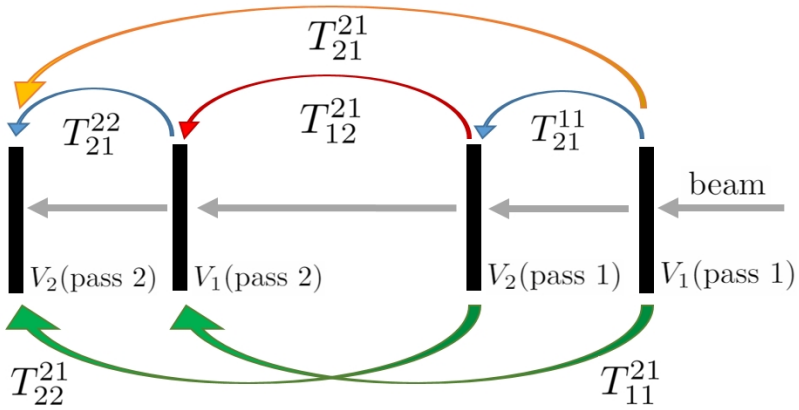

Figure 3.3: (Color) Illustration of the case C configuration. V_j denotes the HOM of cavity j, and T_{ij}^{IJ} is the T_{12} from HOM j of pass J to HOM i of pass I. Arrows with the same color indicate that the corresponding T_{ij}^{IJ} are assumed the same in order to derive Eq. (3.14).

Similar to Case B, the general formula involves calculating the eigenvalues of a complex matrix. However, the formula greatly simplifies if the two HOMs have identical characteristics, and the lattice has symmetric optics ($T_{21}^{22} = T_{21}^{11}$ and $T_{22}^{21} = T_{11}^{21}$) [7]:

$$D(\omega) = -\frac{\kappa}{2}\frac{e^{i\omega t_r}[T_{11}^{21} \pm \sqrt{T_{12}^{21}(T_{21}^{21} + 2e^{-i\omega t_r}T_{21}^{11})}]}{(\omega - \omega_\lambda)t_b + i\epsilon}. \tag{3.14}$$

Comparing to Eq. (3.8) we see the equivalent T_{12} becomes $(T_{11}^{21} \pm \sqrt{T_{12}^{21}(T_{21}^{21} + 2e^{-i\omega t_r}T_{21}^{11})})$, which has two possible values for a fixed ω. Since Eq. (3.14) is a linearized formula, to find the I_{th} we need to apply Eq. (3.7) while considering both values. In general one value gives a greater $|I_0^{-1}|$, which leads to the I_{th}. Eq. (3.14) has several peculiarities which will be explained by the following three cases with special optics, and Fig. 3.4 shows the theory and simulation results for these cases.

Case	Optics
C1	$T_{12}^{21} = 0$
C2	$T_{21}^{22} = T_{21}^{11} = 0$
C3	$T_{21}^{21} = 0$

Table 3.2: The three subcases for case C with special optics.

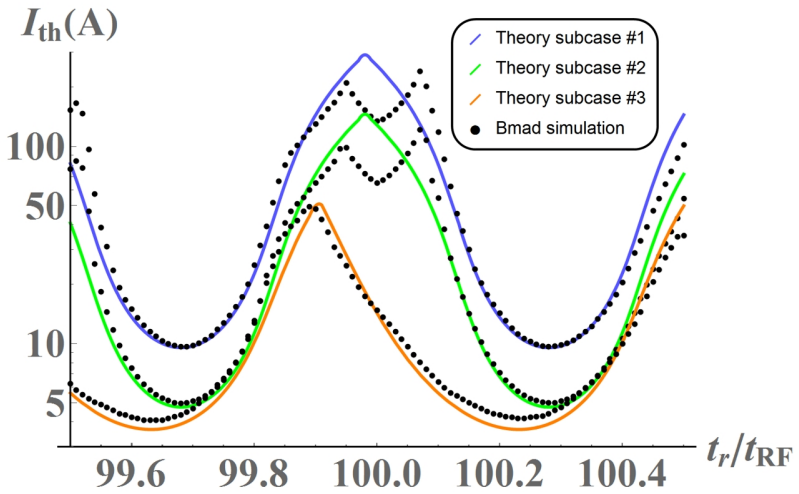

Figure 3.4: (Color) Comparison of the I_{th} obtained from the linearized formula and BMAD simulation for the case C1 (top curve), C2 (middle), and C3 (bottom). The HOM properties are the same as in case A, and the optics are chosen carefully so $T_{11}^{21} = -10\text{m}/(1\text{GeV}/c)$ for all the three subcases.

In the case C1, $T_{12}^{21} = 0$, which means that the second HOM ($j = 2$) can not excite the first HOM ($j = 1$). This is shown clearly by the red arrow in Fig. 3.3. Even though the first HOM can excite the second HOM in this case, there is no feedback from the second HOM. The two HOMs only feedback to themselves. The I_{th} is therefore as large as that of with one single cavity only. Eq. (3.14) supports this argument since the equivalent T_{12} is now simply T_{11}^{21}, which agrees with Eq. (3.8) in the case A. The simulation results again agree well at the trough regions, as observed for all the linearized formulas before.

For the case C2, each HOM can still excite itself directly through T_{ii}^{21} (the green arrows in Fig. 3.3). However, the two HOMs can now excite each other via recirculation through T_{12}^{21} (the red arrow) and T_{21}^{21} (the orange arrow). This mutual excitation results in extra feedback, and changes the equivalent T_{12} to be $(T_{11}^{21} \pm \sqrt{T_{12}^{21} T_{21}^{21}})$, which is independent of ω. This means the I_{th} occurs at the same ω as in the case C1, but the value is scaled down by a constant factor depending on $\sqrt{T_{12}^{21} T_{21}^{21}}$. The scaling effect is shown by the top two curves in Fig. 3.4. Note that if we swap the HOM index i and j, the equivalent T_{12} stays the same.

For the case C3 we have $T_{21}^{21} = 0$. The two HOMs still excite other (via orange and blue arrows in Fig. 3.3), but not symmetrically as in the case C2. The bottom curve of Fig. 3.4 shows the corresponding I_{th} profile, and the location of the trough regions clearly shifts from the two previous cases. This shift is expected due to the extra $e^{-i\omega t_r}$ term in Eq. (3.14). The crest regions might have vanished as we choose between the two quadratic values for greater $|I_0^{-1}|$. The choice at different t_r varies with on the $e^{-i\omega t_r}$ term, which allows us to stay at the trough region given by one of the two values. The overall agreement with

the simulation results also supports that the crest regions, at which linearized formula typically disagrees, have vanished.

3.1.4 Two polarized dipole-HOMs in one cavity with $N_p = 2$

All the cases discussed so far assume that the HOMs are polarized in the horizontal direction only. With cylindrical symmetry there exists a vertical HOM for each horizontal HOM, and the HOM pair has identical HOM characteristics except for the polarization angle. If the recirculation lattice has coupled beam optics between the two transverse phase spaces (i.e. nonzero T_{14} and T_{32}), then the two HOMs could excite each other via recirculation. Similar to case A, we consider the simplest configuration with one cavity and $N_p = 2$. For the case with $\epsilon \ll 1$ and $n_r\epsilon \ll 1$, the approximate formulas for the I_{th} are [17]:

$$I_{\text{th}} = \min(I_{\pm}), \tag{3.15}$$

$$I_{\pm} = \begin{cases} -\frac{\epsilon}{\kappa}\frac{2}{T_{\pm}\sin(\omega_\lambda t_r + \nu_{\pm})} & \text{if it is} < 0 \\ \frac{2}{\kappa T_{\pm}}\sqrt{\epsilon^2 + (\frac{t_b}{t_r})^2 \times \text{minmod}(\omega_\lambda t_r + \nu_{\pm}, \pi)} & \text{o/w}, \end{cases} \tag{3.16}$$

$$T_{\pm}e^{i\nu_{\pm}} = \frac{T_{12}+T_{34}}{2} \pm \sqrt{\left(\frac{T_{12}-T_{34}}{2}\right)^2 + T_{14}T_{32}}, \tag{3.17}$$

$$\text{in which } T_{\pm}, \nu_{\pm} \in \Re \text{ and } T_{\pm} > 0.$$

Note that Eq. (3.15) is essentially Eq. (3.9) with T_{12} replaced by $T_{\pm}$, and $\nu_{\pm}$ added to $\omega_\lambda t_r$. From Eq. (3.15) we see there are two candidates (I_+ and I_-) for the I_{th}, and the nature of coupling (i.e. the matrix elements in Eq. (3.17) determines which one is the I_{th} at different t_r. We define $\Delta\nu = |\nu_+ - \nu_-|$, which measures the phase shift between $I_+(t_r)$ and $I_-(t_r)$. To compare the formula with simulation

results, we again focus on three cases with specified optics, listed in table 3.3 below.

Case	T_{12}	T_{14}	T_{32}	T_{34}		T_-/T_+	$\Delta\nu$
D1	x	0	0	$-x$		1	π
D2	x	$3x$	$-2x$	$4x$		1	4.97
D3	x	$(2+\sqrt{6})x$	$(-2+\sqrt{6})x$	$3x$		13.9	2π

Table 3.3: The three subcases for case D with specified optics. We set $x = -10\text{m}/(\sqrt{2}\text{GeV}/c)$, and the rest of the matrix elements are set to meet symplecticity, consistent with [17]. The optics for case D3 was specifically chosen to obtain $\Delta\nu = 2\pi$.

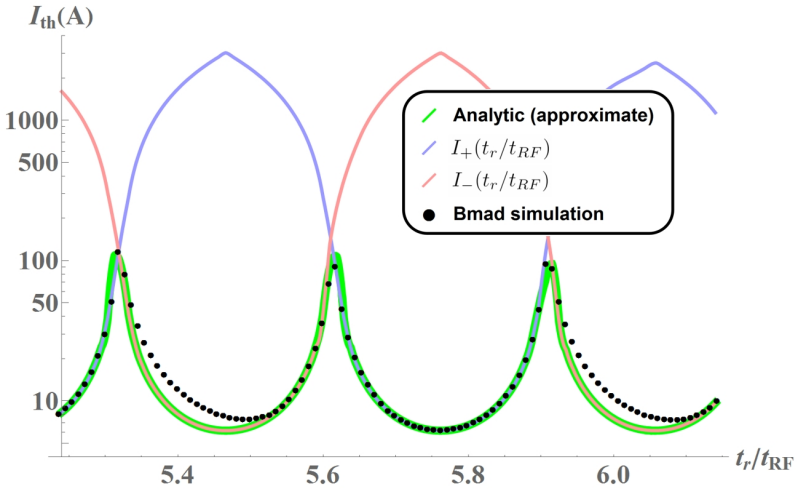

Figure 3.5: (Color) Comparison of the I_{th} obtained from the approximate analytic formula (Eq. (3.15)) and BMAD simulation for case D1. The two candidates for I_{th} ($I_\pm$ from Eq. (3.16)) are also plotted. Parameters used: $t_b = t_{\text{RF}} = 1/1.3$ GHz, $\omega_1 = \omega_2 = 2\pi \times 2.2$ GHz, $Q_1 = Q_2 = 100$, $(R/Q)_1 = (R/Q)_2 = 10^4\ \Omega$.

Fig. 3.5 compares the I_{th} obtained from Eq. (3.15) and BMAD simulation for the case D1. To study the behavior of coupling, the two candidates $I_\pm(t_r)$ are also plotted. Note that both $I_\pm(t_r)$ curves have distinct crest and trough regions as in case A. The two curves are $\Delta\nu = \pi$ out of phase, causing the I_{th} to always stay at the trough regions. This is expected for two reasons. First, the lattice has no coupling ($T_{14} = T_{32} = 0$), so the two HOMs do not excite each other. Mathematically we see $T_+ = |T_{12}|$ and $T_- = |T_{34}|$. The second reason is about

the physical difference between the trough and crest region. The trough region has lower I_{th} because a particle with positive x offset receives positive kick in x after recirculation. In the crest region the particle instead receives a negative kick in x, resulting in a more tolerable I_{th}. Since we have $T_{12} = -T_{34}$ for subcase 1, when x motion benefits from the crest region, y motion suffers from the positive feedback at the trough region, and vice versa. The I_{th} occurs when either x or y motion becomes unstable, not both. If we instead had $T_{12} = T_{34}$, the two candidate curves will overlap each other (in phase with equal magnitude), indicating that x and y motion are identical. In other words, without optical coupling the I_{th} either follows Fig. 3.1 (with distinct crest and trough regions) or Fig. 3.5 (with trough regions only). The BMAD simulation agrees with the approximate formula well, especially in the trough regions of $I_+(t_r)$. Reasons for the slight overestimate of $I_-(t_r)$ at the crest region are to be investigated.

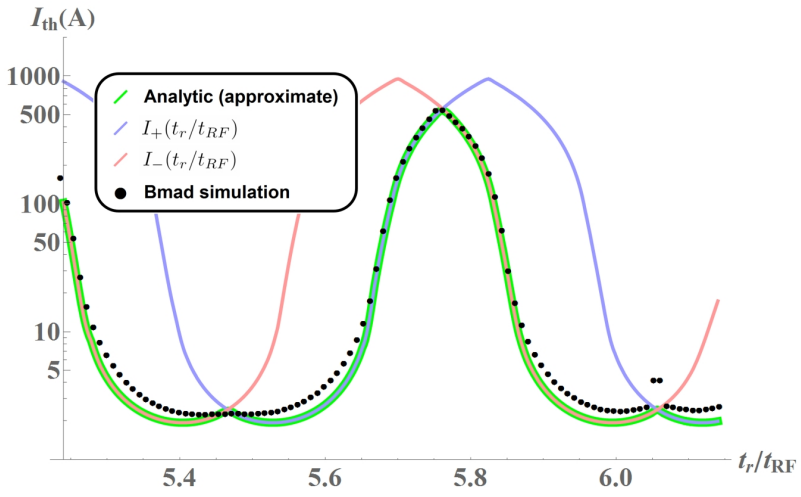

Figure 3.6: (Color) Comparison of the I_{th} obtained from the approximate analytic formula (Eq. (3.15)), the two candidates (Eq. (3.16)), and the BMAD simulation for the case D2. The parameters used are identical as in the case D1, except for the optics.

Fig. 3.6 shows the comparison for the second subcase. The I_{th} for this particular set of optics has been checked in [17] for a specific t_r value, and here we

check against various t_r values with BMAD simulation. Similar to the case D1, case D2 has $T_+ = T_-$, but the different value of $\Delta\nu$ drastically changes the I_{th} behavior at different t_r. Since $\Delta\nu \neq \pi$, the crest regions of the two candidates partially overlap, giving a peak region to the I_{th} curve. Since coupling exists now, the two transverse motions affect each other, and should not be treated independently. Around the peak, the motions together benefit from the crest regions, resulting in a greater I_{th}. Again, BMAD simulation agrees well with the approximate formula.

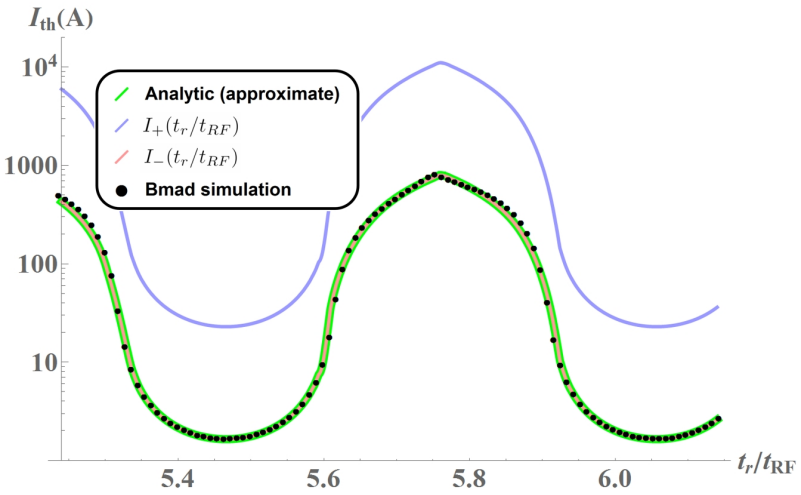

Figure 3.7: (Color) Comparison of the I_{th} obtained from the approximate analytic formula (Eq. (3.15)), the two candidates (Eq. (3.16)), and the BMAD simulation for the case D3. The parameters used are identical as in the case D1, except for the optics.

Lastly, Fig. 3.7 shows the comparison for the case D3. The optics are carefully chosen such that $\Delta\nu$ is 2π, or equivalently zero. This causes the two candidate curves to be in phase, and the ratio $I_+(t_r)/I_-(t_r) = T_-/T_+$ remains constant. The I_{th} curve will always follow the "smaller" candidate curve ($I_-(t_r)$ with our choice of optics). Recall that in the case D1 the two candidate curves would overlap (and be in phase) if T_{12} and T_{34} have the same sign. One might thus wonder what is the effect of coupling in the case D3. In contrast to the case D2

in which coupling changes both the magnitude and phase of the two curves, coupling here only changes their magnitude. The I_{th} magnitude therefore entirely increases or decreases at all t_r depending on the beam optics.

The three cases above have shown that optical coupling can strongly affect the I_{th}. However, in reality it can be difficult to achieve specific optics in order to reach a high I_{th}. For a more general case in BBU with more HOMs and $N_p > 2$, neither the linearized formula nor the approximate formula exists. The general formula becomes more difficult to apply numerically, so we rely on simulation to find the I_{th}. The agreement with the analytic formulas in all the example cases makes us confident to use BMAD to calculate the I_{th} of CBETA.

3.1.5 Comment on recirculation T_{12}

Let us refocus on the most elementary BBU case with one HOM and $N_p = 2$ (Case A). Since the BBU theory derived in [7] assumes a thin-lens cavity, the T_{12} in the formulas corresponds to the T_{12} of the recirculation beamline. This is however an approximation since particles undergo transverse motion through a cavity with nonzero length. Consequently the equivalent T_{12} would depend on other matrix elements (T_{11}, T_{21}, T_{22}, etc.) of the recirculation beamline, as well as the transfer matrix of the cavity itself. This effect is included in BMAD simulation, with the cavity transfer matrix derived in [21], and the transverse HOM kick given instantly at the center of the cavity. Fig. 3.8 shows the I_{th} for case A with varying cavity length. The optics of the recirculation beam line is held constant. In our case, increasing cavity length lowers the equivalent $|T_{12}|$, resulting in a greater I_{th} for all t_r. Physically this reflects the transverse focusing

effect of the cavity.

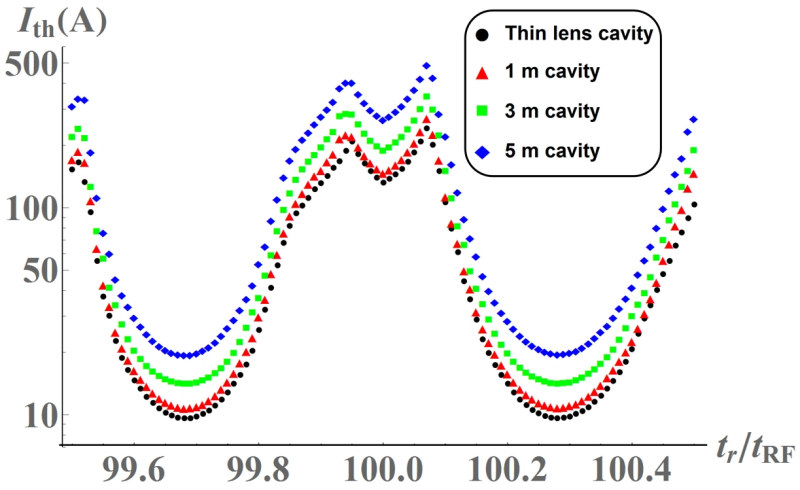

Figure 3.8: (Color) Comparison of the I_{th} obtained from the BMAD simulation for case A with different cavity length. Parameters used are identical as in Fig. 3.1.

In reality the HOM kick is not instant at a specific point of the cavity, but gradual depending the time varying HOM field. A more realistic simulation would therefore integrate the field contribution from both the fundamental mode and the HOM to calculate the exact particle trajectory through the cavity. Since the HOM field depends on the interaction history of the traversed beam, the simulation can be computationally intensive.

3.2 Scaling of multi-pass I_{th} with N_r

The scaling of I_{th} over the number of linac pass N_p was estimated to be

$$I_{\text{th}}(N_r) \approx \frac{1}{N_r(2N_r-1)} I_{\text{th}}(1) \tag{3.18}$$

in [7] for multi-turn accelerators with $N_p = 2N_r$. Here we revisit the scaling law and focus on the case with symmetric ERLs. Symmetry means that the optics

and time of flights of the accelerating passes are mirror symmetric to those of the decelerating passes. Assuming there is only one dipole HOM, the formula for the multi-pass I_{th} can be written as, from the BBU theory:

$$I_{\text{th}} = \frac{2\epsilon}{\kappa}\frac{1}{\max_\omega \Sigma S},\ \Sigma S > 0. \tag{3.19}$$

$$\Sigma S = -\sum_{J=1}^{N_p}\sum_{I=J+1}^{N_p} \sin(\omega(t_I - t_J))\sqrt{\frac{\beta_I\beta_J}{p_I p_J}}\sin(\phi_{IJ}), \tag{3.20}$$

in which β_I and p_I are the beta function and momentum at pass I, and ϕ_{IJ} is the phase advance from pass J to pass I. For an ERL we have the following constraints:

$$N_p \text{ is even.} \tag{3.21}$$

$$N_p \text{ is even.} (t_{I+1} - t_I) = \begin{cases} (m_I + \frac{1}{2}) \times t_{\text{RF}} \text{ if } I = N_p/2 \\ m_I t_{\text{RF}} \quad \text{otherwise } (m_I \in \mathbb{N}). \end{cases} \tag{3.22}$$

For a symmetric ERL we have additional constraints:

$$t_I + t_{N_p - I + 1} = \text{const}\ \forall I. \tag{3.23}$$

$$\beta_I = \beta_{Np-I+1}\ \forall I. \tag{3.24}$$

$$p_I = p_{Np-I+1}\ \forall I. \tag{3.25}$$

$$\phi_{IJ} = \phi_{(N_p-J+1)(N_p-I+1)}\ \forall I > J. \tag{3.26}$$

The goal here is to obtain the scaling law of the $minimum$ I_{th} for a symmetric ERL with adjustable phase advances ϕ_{IJ} and fixed t_I, β_I, and p_I. We define:

$$\min[I_{\text{th}}] = \frac{2\epsilon}{\kappa}(\max_{\omega,\phi_{IJ}} \Sigma S)^{-1},\ \Sigma S > 0. \tag{3.27}$$

For simplicity we choose $\sqrt{\beta_I/p_I} = \text{constant}$. With $\sigma_x \approx \sqrt{\beta_x \epsilon_n/(\beta\gamma)}$, this means the beams size is the same for all I. The symmetry constraint on ϕ_{IJ} reduces the number of free phases from $N_p(N_p-1)/2$ to $N_p/2$. In general, each term

in Eq. (3.27) can be positive or negative depending on the values of (ω, ϕ_{IJ}), and the minimum I_{th} occurs when the sum of these terms, neglecting the minus sign at the front, is the most negative. Fig. (3.9) below shows the resultant $\min[I_{\text{th}}]$ with different N_p and ω_λ after optimization using Mathematica.

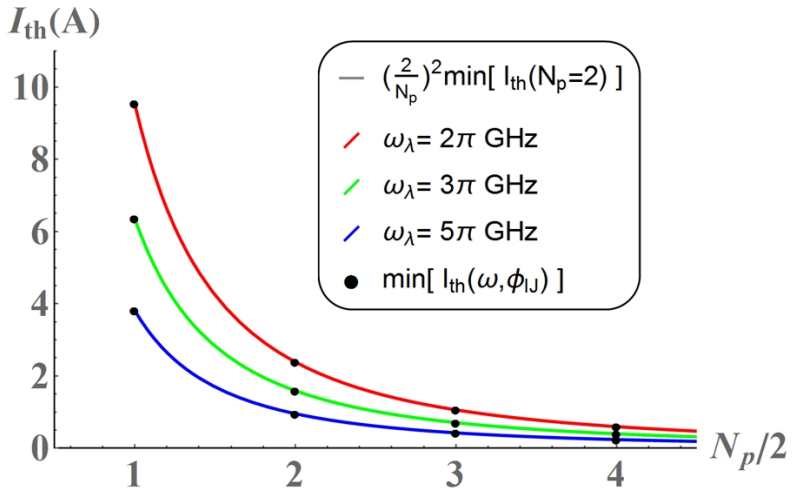

Figure 3.9: (color) Scaling of the $\min[I_{\text{th}}]$ over N_p for symmetric ERLs with different ω_λ. Parameters: $ct_{\text{RF}} = 0.5$m, $t_b = t_{\text{RF}}$, $Q_\lambda = 100$, $(R/Q)_\lambda = 10^4\ \Omega$, $t_{I+1} - t_I = 100t_{\text{RF}}$ (with an additional $\frac{1}{2}t_{\text{RF}}$ for $I = N_p/2$), $\beta_I = 10$m, and $p_I \approx 1\text{GeV}/c$ for all I.

With no prediction it turns out that the minimum I_{th} closely follow a new scaling law:

$$\min[I_{\text{th}}(N_r)] \approx \left(\frac{1}{N_r}\right)^2 \min[I_{\text{th}}(1)]. \tag{3.28}$$

Instead of the estimated value of $1/N_r(2N_r-1)$ in [7], the scaling factor for the $\min[I_{\text{th}}]$ for a symmetric ERL is found to be just $(1/N_r)^2$. While the exact scaling factor requires rigorous mathematical proof, the new scaling factor provides more insight into the I_{th} scaling for symmetric ERLs.

Note that the previous factor in [7] was estimated to be $1/N_r(2N_r - 1)$ because there are $N_r(2N_r - 1)$ terms in Eq. (3.20). However, due to the symmetry constraints, the number of $distinct$ terms is reduced to N_r^2, which happens to

correspond to the new scaling factor of $(1/N_r)^2$. While the previous factor was obtained assuming that the multipass T_{IJ}s have very similar values for $all\ I > J$, the new scaling factor assumes mirror symmetrical optics. In a realistic ERL like CBETA, the former assumption is more difficult to achieve than the latter one, making the new scaling law more relevant. Since ERLs are usually designed to achieve a high I_{th} instead of the $minimum\ I_{\text{th}}$, the applicability of the new scaling law might first seem limited. However, with many cavities and HOMs, the I_{th} tends to locate at the trough region, with a value close to the minimum I_{th}. The new scaling law for the minimum I_{th} can therefore serve as a decent approximation for the scaling of the actual I_{th}.

3.3 Effect of chromaticity on BBU I_{th}

When phase space filamentation is relevant, e.g. when the chromaticity ($\xi = d\nu/d\delta$) times the energy spread (σ_δ) is of order 1, the BBU instability can be suppressed [16]. Here we estimate this effect on the effective T_{12} in the BBU theory. The T_{12} seen by the design particle can be written as:

$$T_{12}(\delta = 0) = \sqrt{\frac{\beta_0\beta_1}{p_0 p_1}}\sin(2\pi\nu_0), \tag{3.29}$$

in which β_0 (β_1) and p_0 (p_1) are the beta function and momentum at the beginning (end) of the recirculation arc around the cavity, and $2\pi\nu_0$ is the phase advance of the design particle.

For a particle with relative energy deviation δ, the phase advance is $2\pi(\nu_0 + \xi\delta)$. Let $\rho(\delta)$ denote the δ distribution of the beam, then the effective T_{12} can be written as:

$$\hat{T}_{12} = \sqrt{\frac{\beta_0\beta_1}{p_0 p_1}} \int_{-\infty}^{\infty} \rho(\delta) \sin(2\pi(\nu + \xi\delta)) d\delta \tag{3.30}$$

Assume $\rho(\delta)$ is a Gaussian distribution with (μ, σ) = (0, σ_δ), and apply the identity $\sin(A + B) = \sin(A)\cos(B) + \cos(A)\sin(B)$. The second term in the integral then vanishes (odd in δ), yielding:

$$\hat{T}_{12} = \sqrt{\frac{\beta_0\beta_1}{p_0 p_1}} \frac{\sin(2\pi\nu_0)}{\sqrt{2\pi\sigma_\delta^2}} \int_{-\infty}^{\infty} e^{-\delta^2/2\sigma_\delta^2} \cos(2\pi\xi\delta) d\delta \tag{3.31}$$

$$= T_{12}(\delta = 0) \frac{1}{\sqrt{2\pi\sigma_\delta^2}} (\sqrt{2\pi\sigma_\delta^2} e^{-(2\pi\xi)^2\sigma_\delta^2/2}) \tag{3.32}$$

$$= T_{12}(\delta = 0) e^{-(2\pi\xi\sigma_\delta)^2/2} \tag{3.33}$$

Fig. (3.10) below shows the I_{th} results of tracking a Gaussian beam (with different σ_δ) through a "one-HOM, $N_p = 2$" lattice (with different chromaticity ξ). From the most elementary BBU case, we know $I_{\text{th}} \propto T_{12}^{-1}$, so from the chromaticity analysis above we expect:

$$I_{\text{th}}(\sigma_\delta, \xi)/I_{\text{th}}(0, 0) = e^{-(2\pi\xi\sigma_\delta)^2/2}. \tag{3.34}$$

Bmad simulation results agree with this prediction for various (σ_δ, ξ).

Since the factor $e^{-(2\pi\xi\sigma_\delta)^2/2}$ is smaller than unity, the effective T_{12} becomes $smaller$ in magnitude, resulting in a greater I_{th} all the time. For a multipass lattice with multiple cavities, the effective T_{12} elements scale up differently depending on the chromaticity of the return loops. Assuming that δ distribution remains Gaussian-like, the I_{th} is expected to be greater than that with only the design particle.

CBETA has no sextupoles, and the natural horizontal chromaticity ξ of its four loops is approximately, from the lowest to the highest design energy, -85.6,

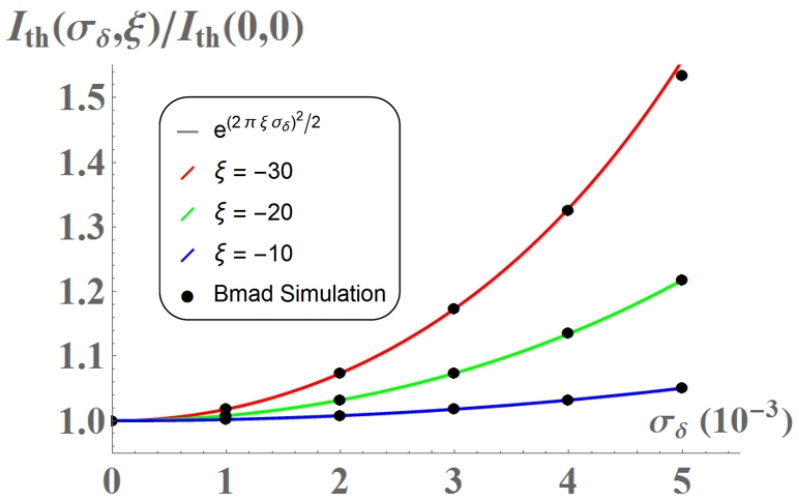

Figure 3.10: (color) The I_{th} results from tracking a Gaussian beam (2000 particles per bunch) through a "one-HOM, $N_p = 2$" lattice with different (σ_δ, ξ). The three curves correspond to the factor $e^{-(2\pi\xi\sigma_\delta)^2/2}$ with different ξ, and the black dots are the simulation results. Parameters: same as in case A (See Fig. 3.1).

-25.3, -16.5, and -14.9. With an energy spread σ_δ of 10^{-3}, the effective T_{12} elements of the lowest energy loop decreases by 13.4%. This means that the I_{th} of CBETA 1-pass mode could increase up to 15.5% assuming only one dipole HOM exists. To check this we tracked a beam with 3000 particles per bunch through the CBETA 1-pass lattice with varying σ_δ and different HOM assignments. Note that these BBU simulations with multiple particles per bunch are computationally intensive comparing to the cases with single particle tracking.

Fig. (3.11) shows that for 50 different HOM assignments, the I_{th} increases as σ_δ increases, and the result curves follow relatively close to the theory prediction. The discrepancy in some of the curves is likely due to the non-Gaussian distribution of the accelerated bunches. Regardless, the results indicate that CBETA 1-pass can reach a higher I_{th} than predicted with single particle tracking. Moreover, the theory can be used to approximate the case of non-Gaussian bunches. Although increasing the energy spread seems to help raising the I_{th},

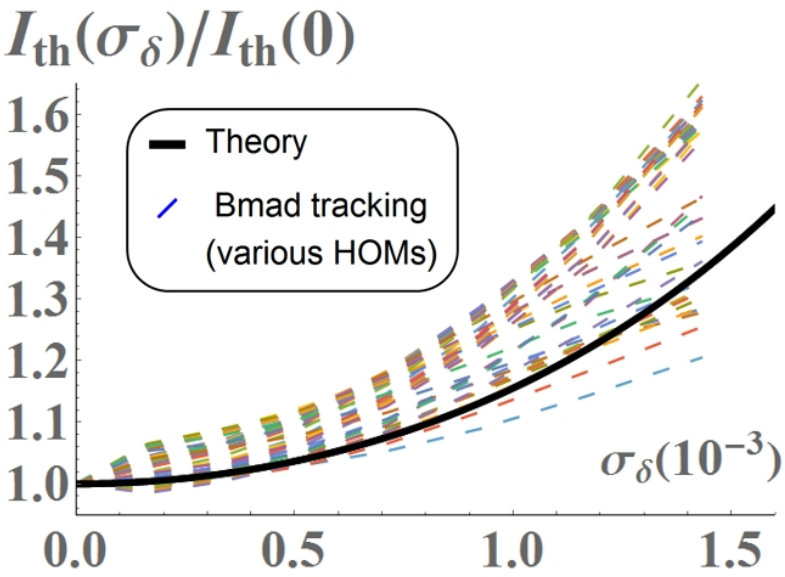

Figure 3.11: (color) Fifty I_{th} results from tracking a beam (3000 particles per bunch) through the CBETA 1-pass lattice with different σ_δ and HOM assignments. Each of the 50 dashed curves corresponds to one specific HOM assignment, and the thick curve is the theory prediction with a Gaussian beam.

it will eventually cause particle loss due to lattice dispersion. A large energy spread can also cause undesired ERL operation at the cavities. The limit and reliability of this method to increase the I_{th} therefore requires experimental testing. For the 4-pass mode, the chromaticity magnitudes of the higher energy loops are much smaller, giving a small chance to increase the I_{th}.

3.4 Bmad BBU Simulation Overview

The BBU program in Bmad requires a lattice with a recirculated cavity(s) with at least one HOM assigned to it. There are six MLC cavities in the CBETA lattice, and multiple HOMs can be assigned to each cavity. The following two subsections describe how the HOM data are generated, and how BMAD numerically finds the I_{th}.

3.4.1 HOM simulation and assignment

Each HOM is characterized by its frequency f, shunt impedance (R/Q), quality factor Q, order m, and polarization angle θ. Since the MLC cavities have been built and commissioned, one would expect direct measurement of HOM spectra from the cavities. Unfortunately, the measured spectra contain hundreds of HOMs, and it is difficult to isolate each individual HOM and compute their characteristics, especially the R/Q value. Therefore, instead of direct measurement, simulated HOM profiles using the known cavity structures are used. The simulations were done by Nick Valles using the CLANS2 program, which can model the fields and HOM spectrum within a cavity [9][10].

The CBETA MLC cavity shapes are characterized by a few ellipse parameters, and in reality each cavity is manufactured with small unknown errors [9]. The fabrication tolerance requires the errors in these parameters to be within $\pm 125\,\mu\mathrm{m}$. For simplicity we use ϵ to denote the maximum deviation, i.e. ϵ = $125\,\mu\mathrm{m}$ for realistic CBETA cavities. In the CLANS2 program, random errors are introduced to the modelled cavity shape within a specified ϵ. The cavity is then compressed to obtain the desired fundamental accelerating frequency of 1.3 GHz. This procedure results in different HOM spectra for each cavity. Hundreds of spectra were generated, each representing a possible cavity in reality. The six MLC cavities have different manufacturing errors, therefore each BBU simulation in Bmad assigns each cavity one of these simulated HOM spectra. With multiple BBU simulations we can obtain a statistical distribution of I_{th} of CBETA because the assigned HOM spectra will be different for each BBU simulation.

To save simulation time we include only the 10 most dominant transverse

dipole-HOMs ($m = 1$) from a pre-calculated spectrum. A dipole-HOM is considered more dominant if it has a greater figure-of-merit $\xi = (R/Q)\sqrt{Q}/f$ [9]. Fig. 3.12 shows an example HOM assignment file with 10 dipole-HOMs for ϵ = $125\,\mu\mathrm{m}$. The zero polarization angles indicate that all these HOMs are horizontally polarized which give no vertical kick to the beam bunches. We include only horizontal HOMs and exclude any vertical HOMs. This is a reasonable model since the cavities have cylindrical symmetry. For the rest of this paper, HOM refers to dipole-HOM unless further specified.

```
                  Frequency R/Q         Q       mode  Polarization_Angle
                  (Hz)      Ohm/m^(2n)                (Radians/2pi)
&long_range_modes
   lr(1) =        8.8302e9  7765.5      606830. 1     0.
   lr(2) =        3.0751e9  3901.5      310240. 1     0.
   lr(3) =        2.549e9   81610.      6229.9  1     0.
   lr(4) =        1.7041e9  51754.      1654.5  1     0.
   lr(5) =        1.7381e9  42511.      1755.8  1     0.
   lr(6) =        1.8702e9  39137.      1610.   1     0.
   lr(7) =        1.8558e9  25852.      1598.9  1     0.
   lr(8) =        1.8711e9  42890.      789.99  1     0.
   lr(9) =        1.872e9   40762.      653.48  1     0.
   lr(10) =       1.6766e9  11687.      707.34  1     0.
/
```

Figure 3.12: An example file of 10 dominant horizontal dipole-HOMs assigned to a single CBETA MLC cavity. The HOMs are simulated using CLANS2 program with ϵ = $125\,\mu\mathrm{m}$. Note that all the HOM frequencies are above the fundamental frequency 1.3 GHz.

3.4.2 Bmad simulation detail

The goal of BBU simulations is to find the I_{th} for a given multipass lattice with HOMs assigned to the cavities. The BMAD program starts with a test current by injecting beam bunches into the lattice at a constant repetition rate. The initial bunches populating the lattice are given small transverse orbit offsets to allow initial excitation of the HOMs. As the bunches pass through the cavities, the momentum exchange between the bunches and the wake fields are calculated,

and the HOM voltages are updated. The program records all the HOM voltages over time and periodically examine their stability. If all HOM voltages are stable over time, the test current is considered stable, and a greater current will be tested. Since the repetition rate is held constant, this is equivalent to raising the charge per bunch. In contrast, if at least one HOM voltage is unstable, the test current is regarded unstable, and a smaller current will be tested. The program typically converges to a I_{th} within 0.1% accuracy in under 30 iterations.

Since the BBU instability occurs because bunches interact with HOMs in the cavities, detailed tracking in the recirculation arc is not required. To save simulation time we usually hybridize the arc elements into an equivalent transfer matrix. The time advantage of hybridization is one to two orders of magnitude.

3.5 Bmad Simulation Result

As discussed, CBETA can operate in either the 1-turn or 4-turn mode, and each of the 6 MLC cavities can be assigned with a set of HOM spectrum. Hundreds of simulations with different HOM assignments were run to obtain a statistical distribution of I_{th} for each specific CBETA design. We will investigate the following five design cases:

Case (1): CBETA 1-turn with $\epsilon = 125\,\mu\text{m}$

Case (2): CBETA 4-turn with $\epsilon = 125\,\mu\text{m}$

Case (3): CBETA 4-turn with $\epsilon = 250\,\mu\text{m}$

Case (4): CBETA 4-turn with $\epsilon = 500\,\mu\text{m}$

Case (5): CBETA 4-turn with $\epsilon = 1000\,\mu\text{m}$

The first two cases aim to model the reality since CBETA cavities have the

fabrication tolerance of $\pm$ 125 µm. The latter three cases with greater fabrication errors are simulated for academic interest. Results of all the cases are presented as histograms in the following subsections. Note that some of the results have been presented in [11].

3.5.1 CBETA 1-turn with ϵ = 125 µm

The design current of CBETA 1-turn mode is 1 mA (the low goal) and 40 mA (the high goal). It's important to note that these goals refer to the injected current, so a 40 mA injected current corresponds to 80 mA for the 1-turn mode ($N_p = 2$) and 320 mA for the 4-turn mode ($N_p = 8$) at the MLC cavities. Fig. 3.13 shows that all 500 simulations results exceed the lower goal of 1 mA, and only one of them is below 40 mA. This is a promising result for the CBETA 1-turn operation. We have to be unfortunate for the cavities to assume certain undesirable combinations of HOMs for the current to not reach the high goal.

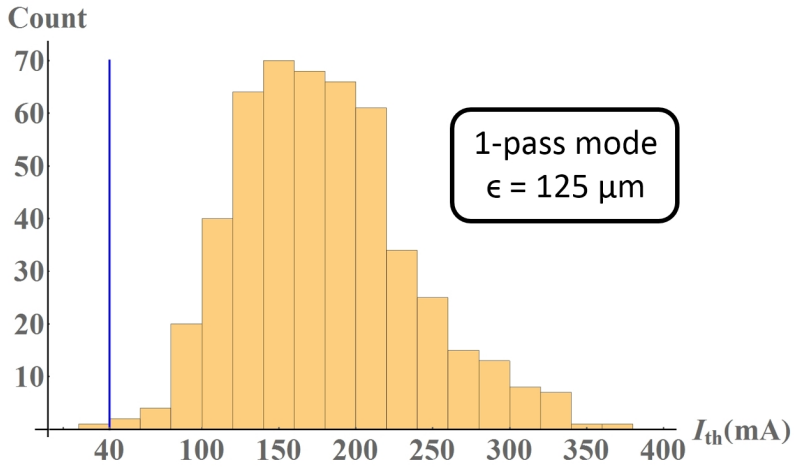

Figure 3.13: 500 BBU simulation results of I_{th} for the CBETA 1-turn lattice. Each cavity is assigned with a random set of 10 dipole HOMs (ϵ = 125 µm). The blue line indicates the higher design goal of 40 mA.

3.5.2 CBETA 4-turn with ϵ = 125 µm

The design current of CBETA 4-turn mode is also 1 mA and 40 mA. Fig. 3.14 shows that for the 4-turn mode, 494 out of 500 simulations exceed the 40 mA goal. This is again quite promising for the 4-turn operation, and for the few cases with undesirably low I_{th}, we will discuss the potential ways to improve them in the following section. Comparing to Fig. 3.13, the average I_{th} for the 4-turn mode is 80.8 mA, much lower than the 179.4 mA of the 1-turn mode. This is expected from the BBU theory, since more recirculation passes allow more interaction between the HOMs and beam bunches, thus resulting in a smaller I_{th}.

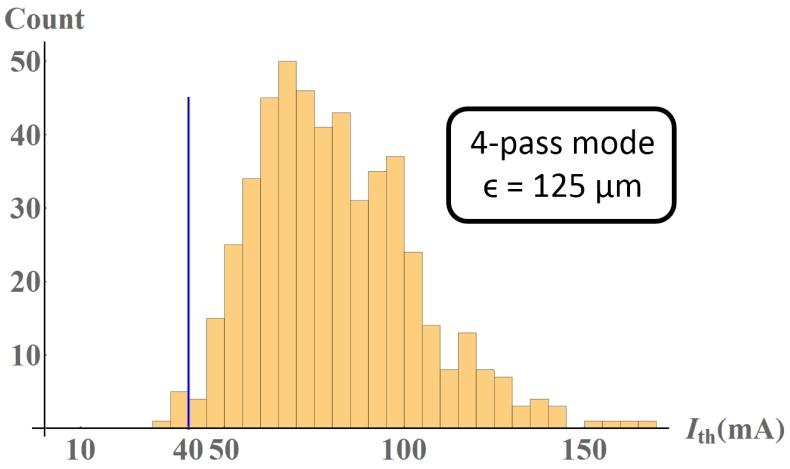

Figure 3.14: 500 BBU simulation results of I_{th} for the CBETA 4-turn lattice. Each cavity is assigned with a random set of 10 dipole HOMs (ϵ = 125 µm).

3.5.3 CBETA 4-turn with $\epsilon \geq 250$ µm

It is interesting to see how I_{th} distribution changes with greater manufacture errors for the 4-turn lattice. Fig. 3.15, Fig. 3.16, and Fig. 3.17 show the results of 500 simulations for ϵ = 250 µm, ϵ = 500 µm, and ϵ = 1000 µm respectively. For

simple comparison, table 3.4 summarizes the statistics of all the results. For ϵ = $250\,\mu\mathrm{m}$, the minimum and average I_{th} are both higher than the $\epsilon = 125\,\mu\mathrm{m}$ case. However, the low average I_{th} for $\epsilon = 1000\,\mu\mathrm{m}$ implies that a greater ϵ does not always improve the I_{th}.

Fundamentally greater deviation in the cavity shape results in greater spread in the HOM frequencies. This causes the HOMs across the cavities to act less coherently when kicking the beam, thus potentially increases the I_{th}. However, a greater deviation also tends to undesirably increase the Q and R/Q of the HOMs, which usually lowers the I_{th}. This could explain why I_{th} statistics improves as ϵ increases from $125\,\mu\mathrm{m}$ to $250\,\mu\mathrm{m}$, but deteriorates at $1000\,\mu\mathrm{m}$. Compensation between the frequency spread and HOM damping also implies that an optimal manufacture tolerance could exist to raise the overall I_{th}.

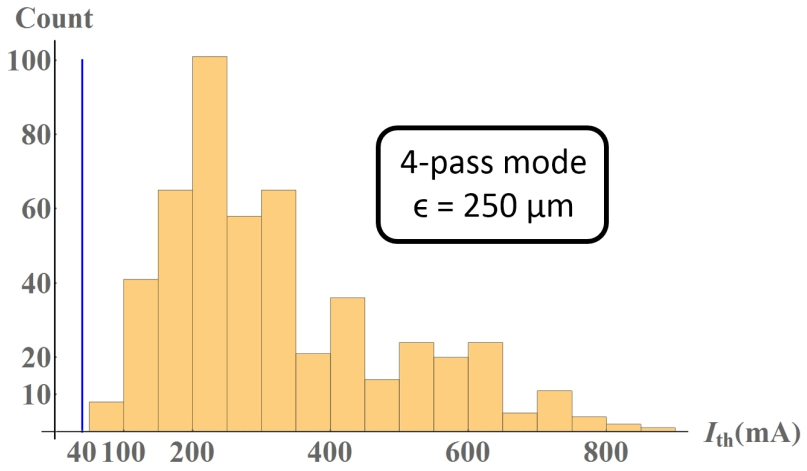

Figure 3.15: 500 BBU simulation results of I_{th} for the 4-turn lattice with cavity shape errors within $\epsilon = 250\,\mu\mathrm{m}$.

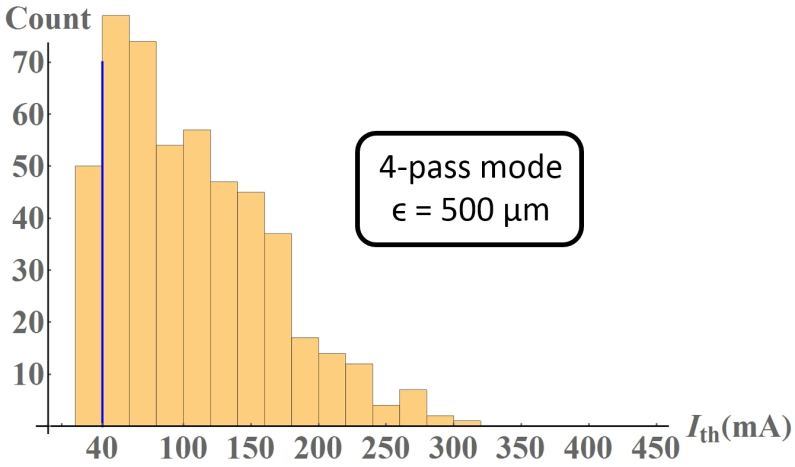

Figure 3.16: 500 BBU simulation results of I_{th} for the 4-turn lattice with cavity shape errors within $\epsilon = 500\,\mu\text{m}$.

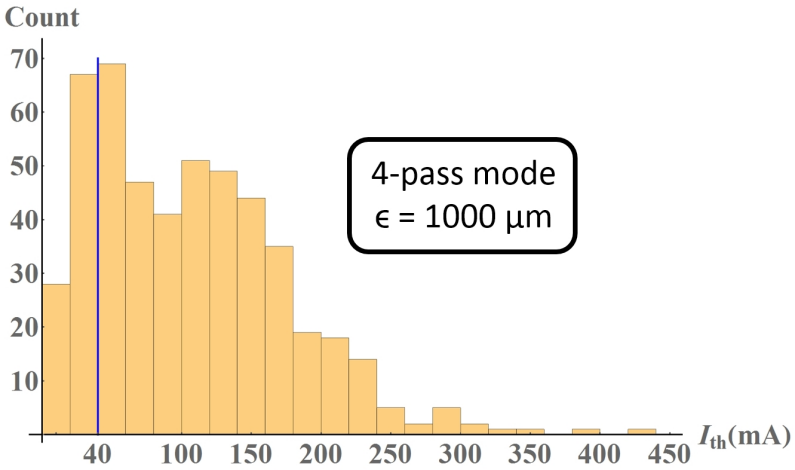

Figure 3.17: 500 BBU simulation results of I_{th} for the 4-turn lattice with cavity shape errors within $\epsilon = 1000\,\mu\text{m}$.

3.6 Aim for higher I_{th}

From BBU theory we know that I_{th} depends generally on the HOM properties $(\omega_\lambda, Q_\lambda, (R/Q)_\lambda)$, the lattice properties (t_r and T_{12}), and the injected bunch time spacing t_b. The previous section shows how I_{th} can vary with different HOM spectra in the cavities. Our goal now is to study how much the I_{th} of CBETA can be improved. Based on the knowledge from BBU theory, three methods

CBETA mode ($N_p/2$)	ϵ (μm)	$\mu(I_{\text{th}})$ (mA)	$\sigma(I_{\text{th}})$ (mA)	$\min(I_{\text{th}})$ (mA)	N in 500 cases with $I_{\text{th}} < 40$ mA
1-turn	125	179.4	56.1	21.9	1
4-turn	125	80.8	22.4	34.4	6
4-turn	250	325.3	164.4	82.4	0
4-turn	500	107.1	59.1	20.4	50
4-turn	1000	106.6	69.3	8.8	95

Table 3.4: Summary of the BBU I_{th} statistics of different CBETA design cases. For the 4-turn mode, ϵ = 250 μm generates the most satisfying I_{th} statistics.

have been proposed and tested for existing 1-turn ERLs:

Method (1) Vary t_b,

Method (2) Vary phase advance, and

Method (3) Introduce x-y coupling.

Both the second and third method involve modifying the optics of the recirculation beamline between the pairs of multipass cavities. The idea of modifying beam optics to improve the I_{th} was first suggested in 1980[12], and has been tested out at the Jefferson Lab's free electron laser [13][14][15]. The effect of all three methods are simulated using BMAD following only the design particle, with results presented in the three following subsections.

When phase space filamentation is relevant, the BBU instability can be suppressed, e.g. when the chromaticity times the energy spread is of order 1 [16]. Since the 42 MeV orbit in the FFA lattice has a great natural chromaticity, additional simulations are performed for the CBETA 1-turn lattice. Note that in order to demonstrate the chromaticity effect, it requires tracking of $multiple$ particles per bunch with an energy spread. This new feature has been implemented in BBU simulation of BMAD. The results and related theoretical analysis are pre-

sented in section VII.

3.6.1 Effect on I_{th} by varying t_b

Eq. (3.5) and Eq. (3.6) show that the I_{th} depends on t_b in a complicated way even for the most elementary BBU case. The dependence however vanishes in the approximate formula for the trough region (Eq. (3.9)). It is interesting to investigate how I_{th} of CBETA varies with t_b using simulation. For all the bunches to see desired longitudinal acceleration, $t_b = nt_{\text{RF}}$ is required with a positive integer n.

For the rest of the paper, let N_p denote the number of times a bunch traverses the multipass cavity(s), which is always equal to the number of recirculations plus one. For an ERL, N_p must be an even number, since each pass through a cavity for acceleration is accompanied by one for deceleration. For instance, the CBETA 1-turn lattice has $N_p = 2$ and one recirculation, while the 4-turn lattice has $N_p = 8$ and seven recirculations. Traditionally such an accelerator is referred to as an $N_p/2$ turn ERL.

For all the CBETA results presented in the previous section, we have set $n = N_p/2$. This corresponds to filling all the RF buckets (i.e. CW operation), and practically we would not use a smaller n to avoid overlapping bunches. Fig. 3.18 shows the simulated I_{th} statistics with increasing n at integer steps for the 4-turn lattice ($N_p = 8, \min[n] = 4$). To focus on the effect of varying t_b only, the 500 sets of HOM assignments are fixed. The result shows that the I_{th} depends weakly on t_b, and potential improvement on I_{th} is limited. Specifically the average I_{th} does not change by 5%. It will still be interesting to test the effect of varying t_b

when CBETA begins operation.

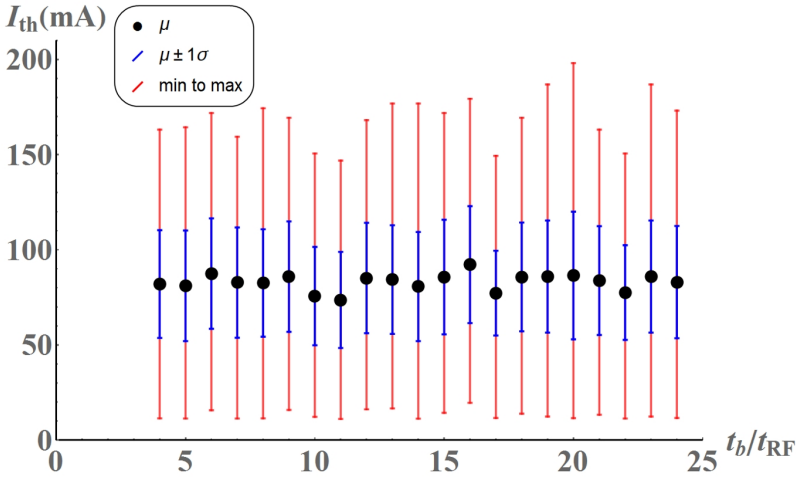

Figure 3.18: (Color) I_{th} v.s t_b/t_{RF} for the CBETA 4-turn lattice. For each t_b/t_{RF}, 500 simulations are run with different HOM assignments (ϵ = 125 µm). The black dot marks the average I_{th}, and the blue inner line marks the $\pm 1\sigma$ range. The red outer line marks the range of the entire distribution.

3.6.2 Effect on I_{th} by varying phase advance

I_{th} can potentially be improved by changing the phase advances (in both x and y) between the multi-pass cavities. This method equivalently changes the T_{12} (and T_{34}) element of the transfer matrices. In the elementary case of BBU theory, smaller T_{12} directly results in greater I_{th} (Eq. (3.5)). However, with multiple cavities and HOMs, it's generally difficult to lower all the T_{12} elements between different HOM pairs. To freely vary the phase advances in BMAD simulations, a zero-length lattice element is introduced right after the first pass of the MLC cavities. The element has the following 4x4 transfer matrix in the transverse phase space:

$$T_{\text{decoupled}}(\phi_x, \phi_y) = \begin{pmatrix} M_{x \leftarrow x}(\phi_x) & \mathbf{0} \\ \mathbf{0} & M_{y \leftarrow y}(\phi_y) \end{pmatrix}. \tag{3.35}$$

Each of the 2x2 submatrix depends on the Twiss parameters (β_i, α_i, and γ_i) in one transverse direction ($i = x$ or y) at the location of introduction:

$$M_{i \leftarrow i}(\phi) = \begin{pmatrix} \cos\phi + \alpha_i \sin\phi & \beta_i \sin\phi \\ -\gamma_i \sin\phi & \cos\phi - \alpha_i \sin\phi \end{pmatrix}. \tag{3.36}$$

Note that ϕ_x and ϕ_y are the additional transverse phase advances introduced by the element, and both can be chosen freely between $[0, 2\pi)$. The 4x4 matrix does not introduce optical coupling between the two transverse phase spaces, and is thus named $T_{\text{decoupled}}$. In reality there is no physical element providing such a flexible transfer matrix, and the phase advances are changed by adjusting the quad strengths around the accelerator structure. In simulation the introduction of this matrix allows us to arbitrarily yet effectively vary the two phase advances.

To investigate how I_{th} varies with both transverse lattice optics, we need to include vertical HOMs which give vertical kicks to the bunches. Therefore for each simulation, each cavity is assigned with three dominant "ϵ = 125 µm" horizontal HOMs and three identical vertical HOMs (polarization angle = $\pi/2$). Fig. 3.19 shows an example assignment to one cavity. With a fixed set of HOM assignments, the I_{th} statistics is obtained for different choices of (ϕ_x, ϕ_y).

```
                  Frequency R/Q         Q         mode  Polarization_Angle
                  (Hz)      Ohm/m^(2n)                    (Radians/2pi)
&long_range_modes
  lr(1) =         2.5512e9  79593.0     6100.8    1     0.0
  lr(2) =         8.8345e9  8005.2      439340.0  1     0.0
  lr(3) =         8.8345e9  7907.8      350650.0  1     0.0
  lr(4) =         2.5512e9  79593.0     6100.8    1     0.25
  lr(5) =         8.8345e9  8005.2      439340.0  1     0.25
  lr(6) =         8.8345e9  7907.8      350650.0  1     0.25
/
```

Figure 3.19: An example file of three dominant horizontal HOMs (the top 3) and three identical vertical HOMs (the bottom 3) assigned to a single CBETA MLC cavity. The HOMs are simulated using HTC program with ϵ = 125 µm.

One hundred statistics were obtained for both the 1-turn and 4-turn CBETA lattice, and typical statistics are shown by Fig. 3.20 and Fig. 3.21 respectively. Depending on the HOM assignment, the peak I_{th} can reach at least 461 mA for the 1-turn mode (and 171 mA for the 4-turn mode) with an optimal choice of (ϕ_x, ϕ_y). Table 3.5 summarizes the statistics of the peak I_{th} with the 100 different HOM assignments. Clearly varying phase advances can be used to (significantly) improve the I_{th}.

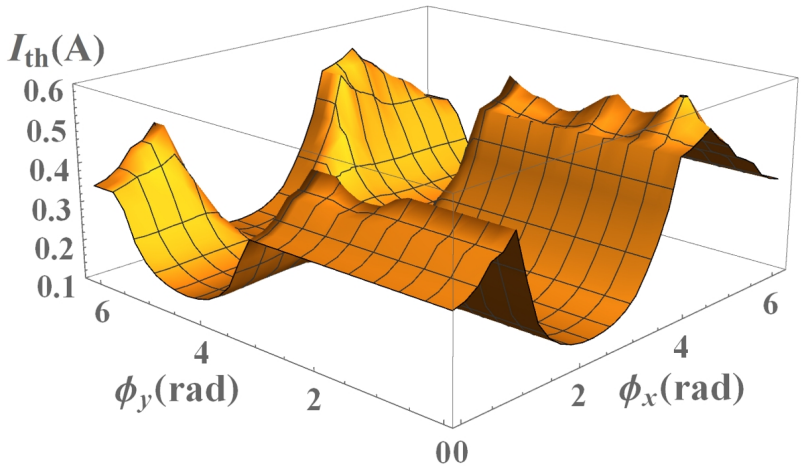

Figure 3.20: A scan of BBU I_{th} over the two phase advances for the CBETA 1-turn lattice. Each cavity is assigned with a random set of 3 dipole HOMs in both x and y polarization. (ϵ = 125 µm). For this particular HOM assignment, I_{th} ranges from 140 mA to 610 mA.

It is also observed that ϕ_x and ϕ_y affect I_{th} rather independently. That is, at certain ϕ_x which results in a low I_{th} (the "valley"), different choice of ϕ_y does not help increase I_{th}, and vise versa. It is also observed that I_{th} is more sensitive to ϕ_x, and the effect of ϕ_y becomes obvious mostly at the "peak" in ϕ_x. Physically this is expected since many lattice elements have a unit transfer matrix in the vertical phase space, and the effect of varying T_{12} is more significant than T_{34}. In other words, HOMs with horizontal polarization are more often excited. As we will see this is no longer true when x-y coupling is introduced.

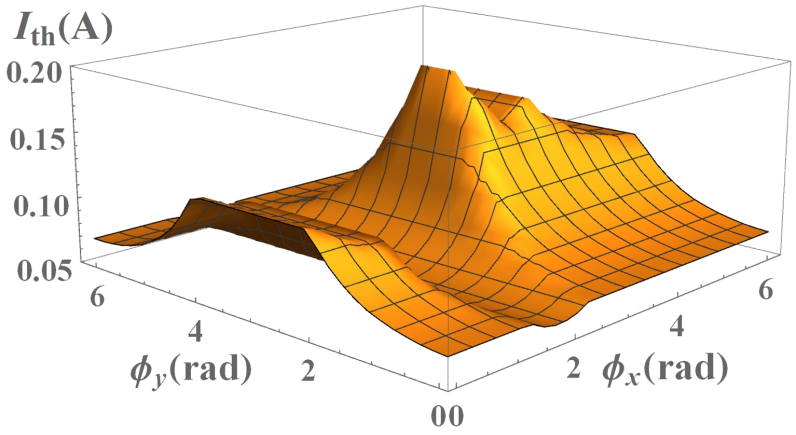

Figure 3.21: A scan of BBU I_{th} over the two phase advances for the CBETA 4-turn lattice. Each cavity is assigned with a random set of 3 dipole HOMs in both x and y polarization. (ϵ = 125 µm). For this particular HOM assignment, I_{th} ranges from 61 mA to 193 mA.

It is also observed that the location of the valley remains almost fixed when HOM assignments are similar. Physically the valley occurs when the combination of phase-advances results in a great equivalent T_{12} (or T_{34}) which excites the most dominant HOM. Therefore, the valley location depends heavily on which cavity has the most dominant HOM, and the simulation results agree with this observation.

In reality the optimal set of (ϕ_x, ϕ_y) to achieve the peak I_{th} may not be achievable for CBETA due to its limited number of free quadrupole magnets and strict constraints on beam optics. However it suffices to have enough freedom to increase the I_{th} over the design goal of 40 mA for the 4-turn mode. It will be interesting to investigate this experimentally at CBETA.

3.6.3 Effect on I_{th} with x-y coupling

Another method potentially improves I_{th} by introducing x-y coupling in the transverse optics, so that horizontal HOMs excite vertical motions and vise versa. This method has been shown very effective for 1-turn ERLs [17]. To simulate the coupling effect in BMAD simulation, a different 4x4 matrix of zero-length is again introduced right after the first pass of the LINAC:

$$T_{\text{coupled}}(\phi_1, \phi_2) = \begin{pmatrix} \mathbf{0} & M_{x\leftarrow y}(\phi_1) \\ M_{y\leftarrow x}(\phi_2) & \mathbf{0} \end{pmatrix}. \tag{3.37}$$

The elements of the two 2x2 submatrices $M_{j\leftarrow i}(\phi)$ are specified using on the transverse Twiss parameters at the location of introduction:

$$\begin{aligned} M_{11} &= \sqrt{\tfrac{\beta_j}{\beta_i}}(\cos\phi + \alpha_i \sin\phi) \\ M_{12} &= \sqrt{\beta_j\beta_i}\sin\phi \\ M_{21} &= \tfrac{1}{\sqrt{\beta_j\beta_i}}[(\alpha_i - \alpha_j)\cos\phi - (1 + \alpha_i\alpha_j)\sin\phi] \\ M_{22} &= \sqrt{\tfrac{\beta_j}{\beta_i}}(\cos\phi - \alpha_j \sin\phi). \end{aligned} \tag{3.38}$$

The 4x4 symplectic matrix T_{coupled} couples the lattice optics in the two transverse directions with two phases of free choice (ϕ_1, ϕ_2). Note the two phases are not the conventional phase advances, and can both range from 0 to 2π.

Fig. 3.22 and Fig. 3.23 show a typical way I_{th} varies with the two free phases for the 1-turn and 4-turn lattice respectively. Depending on the HOM assignment, the I_{th} can reach at least 299 mA for the 1-turn mode (and 127 mA for the 4-turn mode) with an optimal choice of (ϕ_1, ϕ_2). Because the transverse optics are coupled, the two phases no longer affect I_{th} in an independent manner. That is, there is no specific ϕ_1 which would always result in a relatively high or low I_{th}. The two phases need to be varied together to reach the peak I_{th}.

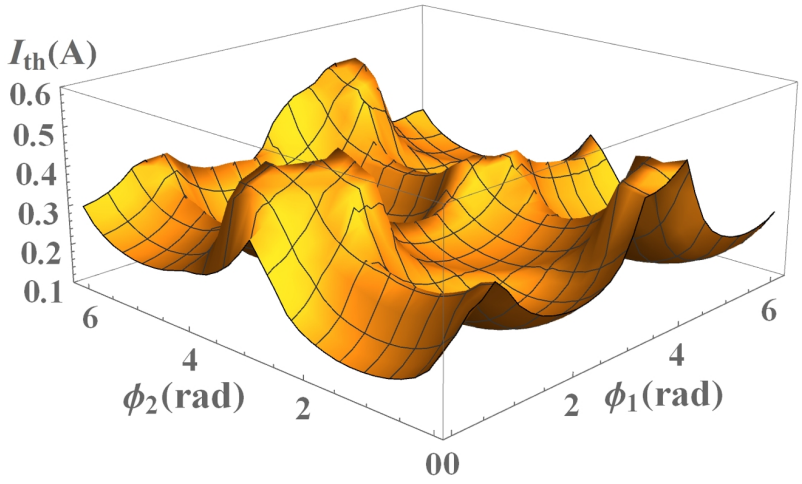

Figure 3.22: A scan of BBU I_{th} over the two free phases for the CBETA 1-turn lattice with x-y coupling. Each cavity is assigned with a random set of 3 dipole HOMs in both x and y polarization. (ϵ = 125 µm). For this particular HOM assignment, I_{th} ranges from 140 mA to 520 mA.

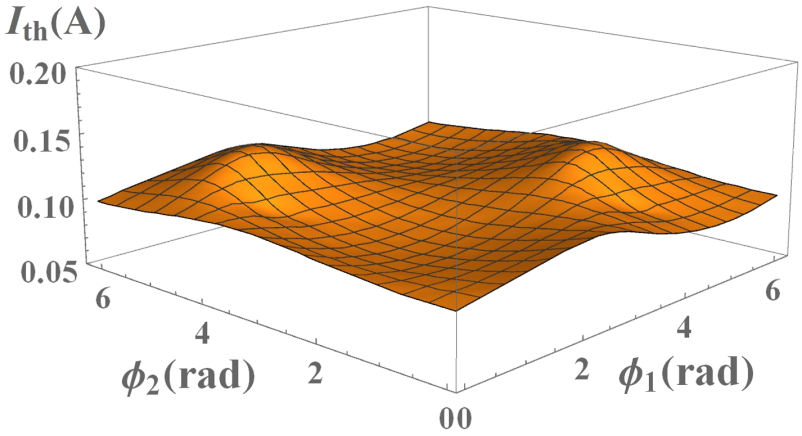

Figure 3.23: A scan of BBU I_{th} over the two free phases for the CBETA 4-turn lattice with x-y coupling. Each cavity is assigned with a random set of 3 dipole HOMs in both x and y polarization. (ϵ = 125 µm). For this particular HOM assignment, I_{th} ranges from 89 mA to 131 mA.

Similar to the case with decoupled optics, 100 statistics are run for both the 1-turn and 4-turn mode with different HOM assignments, and the statistics of the peak I_{th} are summarized in Table 3.5. As expected from theory, the I_{th} can statistically reach a higher value for the 1-turn mode than the 4-turn mode. While introducing additional phase advances and x-y coupling both give great poten-

tial to raise the peak I_{th} (way above the high design goal of 40 mA), the former gives more. In realty, introducing x-y coupling also requires installation of skew quadrupole magnets, and CBETA might not achieve this due to limited space. In short, varying phase advances is the most promising method to improve the I_{th} of CBETA.

Case (optics)	$\min$(peak I_{th}) (mA)	μ(peak I_{th}) (mA)	$\max$(peak I_{th}) (mA)
1-turn (decoupled)	461	733	1275
1-turn (coupled)	299	557	928
4-turn (decoupled)	171	440	758
4-turn (coupled)	127	434	548

Table 3.5: Summary of the I_{th} statistics with varying transverse optics over 100 different HOM-assignments for the CBETA 1-turn and 4-turn mode. For both modes, introducing additional phase advances (decoupled optics) gives greater potential to increase I_{th} than x-y coupling.

3.6.4 Conclusion

To establish the trustworthiness of BBU simulations for CBETA, agreement has been found between the BBU theory and BMAD simulations for multi-turn ERL setups. This gives us confidence in BMAD simulation for determining the I_{th} for ERL lattices with multipass cavities and multiple HOMs, like CBETA. Simulation results show that for CBETA (both the 1-pass and 4-pass mode), the I_{th} can always surpass the low design current of 1 mA, and can reach the high goal of 40 mA in over 98% of the cases with realistic cavity construction errors.

In the remaining 2% of the cases, the I_{th} can be improved by adjusting the lattice optics, which has been an effective method for 1-turn ERLs like the Jefferson FEL-ERL. Varying phase advances is shown to be more effective than introducing x-y coupling. Also, both methods are shown less effective in multi-turn

ERLs than in the 1-turn arrangement. It is intended to verify these observations experimentally, and it will be interesting to test the applicability and effectiveness of all these methods in CBETA.

The scaling law of the I_{th} with N_r is revisited for the case with symmetric ERLs, and the scaling factor is found to be approximately $1/N_r^2$. This new scaling law has better applicability for ERLs than the previously approximated factor of $1/N_r(2N_r - 1)$ in [7]. Also, the effect of lattice chromaticity on the I_{th} is studied assuming bunches with an Gaussian energy spread, and a relationship between the I_{th}, chromaticity, and energy spread was found. Results with the CBETA 1-pass lattice show that the I_{th} in reality can be higher than predicted using single particle tracking.

CHAPTER 4

COHERENT SYNCHROTRON RADIATION

4.1 Two particle interaction

The most elementary CSR theory studies the interaction of two electrons passing through one bending magnet, and the CSR wake $w = d\mathcal{E}_{\text{CSR}}/cdt$ has been derived for four different cases (A,B,C, and D) in [22], depending on the location of the source and the observation points within or outside the magnet. The approximated wake expressions $W(s) = \int w(s-s')\lambda(s')ds'$ for an arbitrary longitudinal bunch distribution $\lambda(s)$ have been calculated for the four cases in [23]. However, if a second magnet is located downstream not sufficiently far away for the exit wake from the first magnet to attenuate, the wake leaks into the second magnet, and the existing formulas cannot be applied. Therefore, our goal is to derive the wake expressions for a system with two magnets.

The Lienard-Wiechert formula describes the electric field seen by the front electron at point P (as in Fig. 4.1 for example) at time t. This field is produced by the tail electron at point P' at retarded time t' [25]:

$$\mathbf{E}(P) = \frac{ke}{\gamma^2}\frac{(\mathbf{L} - L\beta\mathbf{n}')}{(L - \mathbf{L}\cdot\beta\mathbf{n}')^3} + \frac{ke}{c^2}\frac{(\mathbf{L}\times[(\mathbf{L} - L\beta\mathbf{n}')\times\mathbf{a}'])}{(L - \mathbf{L}\cdot\beta\mathbf{n}')^3}, \tag{4.1}$$

in which $k = 1/(4\pi\epsilon_0)$, e is the electron charge, and c is the speed of light. $\mathbf{L}$ is the vector pointing from P' to P, and L is its magnitude. The two electrons are assumed to have the same speed $v = \beta c$. $\mathbf{n}'$ and $\mathbf{a}'$ are respectively the unit velocity vector and the acceleration at point P'. By convention we refer to the term in Eq.(4.1) that is proportional to $1/\gamma^2$ as the velocity field, and the term with $\mathbf{a}'$ as the acceleration field [22].

Let L_s denote the path length from P' and P travelled by the electron. Also, let s and s' denote the longitudinal position of the front and tail electron at time t with respect to the bunch center (Note: s' is evaluated at the observation time t, *not* the retarded time t'). Then the distance between the two particles at time t can be expressed as [26]:

$$\Delta \equiv s - s' = L_s - \beta L. \tag{4.2}$$

As we will see, Δ is an important quantity in deriving the wake expressions. As $\Delta \to 0$, the velocity field has a singularity of order $1/\Delta^2$, which is dealt with by splitting $\mathbf{E}(P)$ into two terms:

$$\mathbf{E}(P) = \mathbf{E}_{\text{SC}} + \mathbf{E}_{\text{CSR}}. \tag{4.3}$$

The singularity is contained in the space charge term:

$$\mathbf{E}_{\text{SC}} = \frac{ke\mathbf{n}}{\gamma^2\Delta^2}, \tag{4.4}$$

in which $\mathbf{n}$ is the unit velocity vector at point P. $\mathbf{E}_{\text{SC}}$ is the field resulting from two particles moving on a straight line without acceleration. The rate of change in energy of the front electron at point P is:

$$\frac{d\mathcal{E}}{dt} = \mathbf{v} \cdot \mathbf{F} = ec\beta\mathbf{n} \cdot \mathbf{E}(P). \tag{4.5}$$

The CSR wake seen by the front electron is defined to be:

$$w \equiv \frac{d\mathcal{E}_{\text{CSR}}}{cdt} = e\beta\mathbf{n} \cdot (\mathbf{E}(P) - \mathbf{E}_{\text{SC}}). \tag{4.6}$$

Our goal is to find w for the cases with two bending magnets, and apply similar approximations in [23] to solve for the wake expression $W(s)$ seen by the full bunch. Note that this is a one dimensional theory which assumes that all electrons move along the same path. Following the nomenclature in [22], this will

introduce four additional cases: E, F, G, and H. Case E and G are extension of case A and C in which P' is located on the drift before the first magnet. We call these cases the "odd cases". Similarly, case F and case H are extension of case B and D in which P' is located within the first magnet, and we call them the "even cases". In the two subsections below we will derive the wake expressions respectively for the four odd cases and four even cases. The main results for all eight cases are summarized in Appendix A.

4.1.1 Odd cases

We will first re-derive the wake expression for case A and C, then apply similar formulation to obtain the expressions for case E and G.

Case A

The geometry for case A is shown in Fig. 4.1. The observation point P is located at an angle θ into the magnet. Since P' is located on a drift, i.e. $\mathbf{a}' = 0$, as the acceleration field vanishes. Let us define

$$\mathcal{N}_v \equiv \beta\mathbf{n} \cdot (\mathbf{L} - L\beta\mathbf{n}'), \tag{4.7}$$

$$\mathcal{D} \equiv (L - \mathbf{L} \cdot \beta\mathbf{n}'). \tag{4.8}$$

The subscript v indicates that the numerator belongs to the velocity field. Then we can write w as:

$$w = \frac{ke^2}{\gamma^2}\left(\frac{\mathcal{N}_v}{\mathcal{D}^3} - \frac{1}{\Delta^2}\right). \tag{4.9}$$

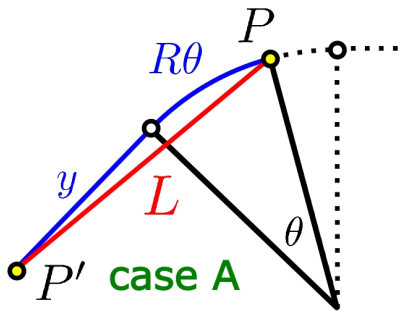

Figure 4.1: (Color) Geometry for case A. Point P and P' are labeled by yellow dots. The blue curve is the path traversed by electrons. These conventions apply to all other geometry figures in Section I.

To find $\mathcal{N}_v$ and $\mathcal{D}$ we have to first fix our coordinate system. Let us pick the unit velocity vector at P to be $\mathbf{n} = \langle 1, 0, 0\rangle$. Vector analysis shows that:

$$\mathbf{n}' = \langle \cos\theta, \sin\theta, 0\rangle, \tag{4.10}$$

$$L_x = y\cos\theta + L_c\cos(\theta/2), \tag{4.11}$$

$$L_y = y\sin\theta + L_c\sin(\theta/2), \tag{4.12}$$

in which L_c is the chord length (See Fig.(1)), and $\mathbf{L} = \langle L_x, L_y, 0\rangle$. As in [22], we assume a small bending angle ($\theta \ll 1$), and expand all quantities, holding $R\theta$ constant, up to order of θ^2. This yields:

$$L_c = R\theta - R\theta^3/24, \tag{4.13}$$

$$L = L_s - \frac{R\theta^3}{24}\frac{(R\theta + 4y)}{L_s}, \tag{4.14}$$

in which $L_s = (R\theta + y)$ for case A. Since $R\theta$ is held constant, terms like $R^n\theta^{(n+2)}$ do *not* vanish ($n \in \mathbb{N}$). It follows that:

$$\Delta = L_s - \beta L = \frac{L_s}{2\gamma^2} + \frac{R\theta^3}{24}\frac{(R\theta + 4y)}{L_s}. \tag{4.15}$$

Since we are interested in cases with large γ, β is taken to be unity except for $(1-\beta) \approx 1/2\gamma^2$ in the leading term.

Applying Eq. (4.7),(4.8), and (4.9) gives:

$$\mathcal{N}_v = \frac{L_s}{2\gamma^2} + \frac{R\theta^3(3R\theta + 4y)}{8L_s}, \tag{4.16}$$

$$\mathcal{D} = \frac{L_s}{2\gamma^2} + \frac{R^2\theta^4}{8L_s}, \tag{4.17}$$

$$w = ke^2\gamma^2 L_s^2 \left(\frac{64[4L_s^2 + \gamma^2 R\theta^3(3R\theta + 4y)]}{(4L_s^2 + \gamma^2 R^2\theta^4)^3} - \frac{576}{(12L_s^2 + \gamma^2 R\theta^3(R\theta + 4y))^2} \right). \tag{4.18}$$

Eq. (4.18) agrees with Eq. (30) from [22]. The first term, with the cubic in the denominator, comes from the velocity field. The second term comes from the space charge field, and it monotonically decreases with y. Note that if $\theta = 0$, the two terms cancel each other, and w vanishes regardless of γ. There is thus no CSR field for particles on a straight line because the space charge term has been subtracted in Eq. (6).

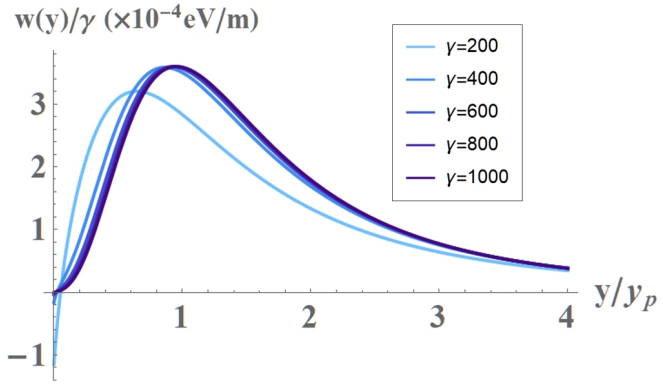

Figure 4.2: (Color) $w(y)$ for various γ values with $R = 1.0$ m and $\theta = 0.04$ rad. For large γ, $w(y)$ is maximized at $y \approx y_p = \frac{1}{2}\gamma R\theta^2$. Note that w is negative at small y due to the space charge field term.

Fig. 4.2 shows the wake as a function of y for different γ. At large γ the wake is localized in the vicinity $y \sim y_p = \frac{1}{2}\gamma R\theta^2$. This means for large γ, the main contribution to $W(s)$ comes from electrons with a retarded position $y \gg R\theta$.

With this the wake reduces to:

$$w(y) = 4ke^2\gamma^2 \left[\frac{64y^3(y+\gamma^2 R\theta^3)}{(4y^2+\gamma^2 R^2\theta^4)^3} - \frac{9}{(3y+\gamma^2 R\theta^3)^2} \right]. \tag{4.19}$$

In the limit of $\gamma^2 \gg L_s/R\theta^3$, the second term in the velocity field term dominates, giving:

$$w(y) = 256ke^2\gamma^4 \frac{y^3 R\theta^3}{(4y^2+\gamma^2 R^2\theta^4)^3}. \tag{4.20}$$

One can check that y_p maximizes this term. For large γ the wake can be approximated as a dirac delta function: $w(y) \sim \delta(y - y_p)$. This is a good approximation because the beam distribution over the retarded positions of P' are stretched over a much longer distance than the width of the peak in Fig. 2. To find the corresponding dirac delta function in the Δ space, we need to calculate $\Delta(y = y_p)$. In the limit $y \gg R\theta$, we have:

$$\Delta(y) = \frac{y}{2\gamma^2} + \frac{1}{6}R\theta^3 - \frac{1}{8y}R^2\theta^4 + O(1/y^2). \tag{4.21}$$

Neglecting higher order terms, we have $\Delta(y_p) = \frac{1}{6}R\theta^3$. Therefore the wake in the Δ space can be written as:

$$w(\Delta) = A\delta\left(\Delta - \frac{1}{6}R\theta^3\right). \tag{4.22}$$

This makes sense since for large γ, the dominant term in $\Delta(y)$ is the constant term $R\theta^3/6$. Assuming that the drift in front of the magnet is infinitely long, the normalization factor A can be found by:

$$A = \int w d\Delta = \int_0^\infty w(y)\frac{\partial\Delta}{\partial y}dy, \tag{4.23}$$

in which $w(y)$ is given by Eq.(20) and the derivative $\frac{\partial\Delta}{\partial y}$ can be computed from Eq.(21):

$$\frac{\partial\Delta}{\partial y} = \frac{1}{2\gamma^2} + \frac{1}{8y^2}R^2\theta^4. \tag{4.24}$$

`Mathematica` gives $A = 4ke^2/R\theta$. For a bunch with a longitudinal distribution $\lambda(s)$, the wake expression $W(s)$ is:

$$W(s) = \int w(s-s')\lambda(s')ds' \tag{4.25}$$

$$= \frac{4ke^2}{R\theta}\lambda\left(s - \frac{1}{6}R\theta^3\right). \tag{4.26}$$

Eq. (4.26) agrees with Eq. (10) in [23]. Assuming the bunch has a bunch length of l_b, then for a large entrance angle θ such that $R\theta^3/6 \gg l_b$, the wake attenuates. In the case where the bunch has not entirely entered the magnet (i.e. $R\theta < l_b$), then the tail portion of the bunch outside the magnet sees no CSR wake.

There are some limitations in applying the wake expression in Eq. (4.26). First, the derivation assumes that $\gamma^2 \gg L_s/R\theta^3$, which implies that $\theta \gg 1/\gamma$ is required. Therefore depending on the γ value, the observation point cannot be too close to the magnet entrance. For small θ such that $\theta \sim 1/\gamma$, or equivalently $\Delta \sim R/\gamma^3$, the wake needs to be found numerically. However for a very large γ such a small numerical scale can be difficult to resolve in simulation software. A numerical formulation to resolve this has been presented in IPAC 2017 [27].

In addition, the derivation assumes a drift with a length $y_m \gg y_p$, so that most of the peak in Fig. (2) appears within the drift. Note that y_p can be large since it increases with γ. For an insufficiently long drift, one needs to use the more general formula from Eq. (4.25) to calculate $W(s)$:

$$W(s) = \int_{s-\Delta(y=y_m)}^{s-\Delta(y=0)} w(s-s')\lambda(s')ds' \tag{4.27}$$

$$= \int_0^{y_m} w(y)\lambda(s-\Delta(y))\frac{\partial\Delta}{\partial y}dy, \tag{4.28}$$

in which $w(y)$ is given by Eq.(4.18). Note that change of variable from s' to y has been applied so there is no need to find an expression for $w(\Delta)$. In the case with $y_m \ll y_p$, contribution from the drift becomes insignificant for $\gamma\theta \gg 1$.

Case C

The geometry for case C is shown in Fig. 4.3 below. Since case C is an extension of case A, we will apply a similar derivation process. To find $\mathcal{N}_v$ and $\mathcal{D}$ we

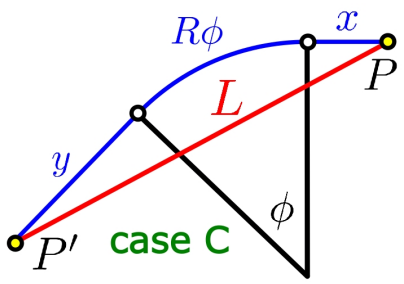

Figure 4.3: (Color) Geometry for case C.

have to first fix our coordinate system. Let us pick the exit point of the bending magnet to be the origin, and the exit drift to lie along the $+x$ axis. This choice will be shown convenient for case E too. Let ϕ denote the *total* bending angle of the magnet. Vector analysis shows that:

$$\mathbf{n} = \langle 1, 0, 0 \rangle, \tag{4.29}$$

$$\mathbf{n}' = \langle \cos\phi, \sin\phi, 0 \rangle, \tag{4.30}$$

$$L_x = y\cos\phi + L_c\cos(\phi/2) + x, \tag{4.31}$$

$$L_y = y\sin\phi + L_c\sin(\phi/2). \tag{4.32}$$

We again expand all quantities in small ϕ, holding $R\phi$ constant, up to order of ϕ^2. This yields:

$$L_c = R\phi - R\phi^3/24, \tag{4.33}$$

$$L = L_s - \frac{\phi^2}{24}\frac{R^2\phi^2 + 4R\phi(x+y) + 12xy}{L_s}, \tag{4.34}$$

$$\Delta = \frac{L_s}{2\gamma^2} + \frac{\phi^2}{24}\frac{R^2\phi^2 + 4R\phi(x+y) + 12xy}{L_s}, \tag{4.35}$$

in which $L_s = R\phi + x + y$ for case C. Applying Eq. (4.7) and Eq. (4.8) gives:

$$\mathcal{N}_v = \frac{L_s}{2\gamma^2} + \frac{(R\phi + 2x)(3R\phi + 2x + 4y)\phi^2}{8L_s}, \tag{4.36}$$

$$\mathcal{D} = \frac{L_s}{2\gamma^2} + \frac{(R\phi + 2x)^2\phi^2}{8L_s}. \tag{4.37}$$

These lead to:

$$w = ke^2\gamma^2 L_s^2 \left(\frac{64[4L_s^2 + \gamma^2\phi^2(R\phi + 2x)(3R\phi + 2x + 4y)]}{(4L_s^2 + \gamma^2\phi^2(R\phi + 2x)^2)^3} - \frac{576}{(12L_s^2 + \gamma^2\phi^2(R^2\phi^2 + 4R\phi(x + y) + 12xy))^2} \right). \tag{4.38}$$

Eq. (4.38) agrees with Eq. (34) from [22]. As expected, the wake vanishes if $\phi \to 0$ or $x \to \infty$. In the limit $\gamma^2 \gg L_s/(R\phi + 2x)\phi^2$, the second term in the velocity field term dominates. With the additional limit of $y \gg R\phi$ and $y \gg x$, the wake reduces to:

$$w = 256ke^2\gamma^4 \frac{y^3(R\phi + 2x)\phi^2}{(4y^2 + \gamma^2(R\phi + 2x)^2\phi^2)^3}. \tag{4.39}$$

This wake is maximized at $y_p = \frac{1}{2}\gamma(R\phi + 2x)\phi$. In the limit of large y we also have:

$$\Delta(y) = \frac{y}{2\gamma^2} + \frac{1}{6}(R\phi + 3x)\phi^2 - \frac{1}{8y}(R\phi + 2x)^2\phi^2 + O(1/y^2). \tag{4.40}$$

Similar to case A, we assume that y_m, the length of the drift in front of the magnet, is much longer than y_p. With $\Delta(y_p) = \frac{1}{6}(R\phi + 3x)\phi^2$, the wake can be approximated as a dirac delta function:

$$w(\Delta) = A\delta\left(\Delta - \frac{1}{6}(R\phi + 3x)\phi^2\right). \tag{4.41}$$

The normalization factor A can be found by:

$$A = \int_0^\infty w(y)\frac{\partial\Delta}{\partial y}dy = \frac{4ke^2}{R\phi + 2x}, \tag{4.42}$$

For a bunch with a longitudinal distribution $\lambda(s)$, the wake expression $W(s)$ is:

$$W(s) = \int w(s-s')\lambda(s')ds' \tag{4.43}$$

$$= \frac{4ke^2}{(R\phi+2x)}\lambda\left(s - \frac{1}{6}(R\phi+3x)\phi^2\right), \tag{4.44}$$

which agrees with Eq. (10) in [23]. For $x \to 0$, we recover the expression for case A. For large x, the wake vanishes as expected. Since the derivation assumes $\gamma^2 \gg L_s/(R\phi+2x)\phi^2$, the bending angle ϕ cannot be too small. Also, the drift in front of the magnet has to be much longer than y_p. Otherwise one needs to use a more general formula as Eq. (4.28).

Case E1

Case E has two subcases depending on the bending direction of the second magnet. For case E1, the two magnets have the same bending direction. For opposite bending directions, see case E2 in the following subsection. The geometry for case E1 is shown in Fig. 4.4. A second magnet with a bending radius R_2 has been introduced at a distance x behind the first magnet. The observation point P is located at an angle θ_2 into the second magnet. Note that θ_2 is *not* the total bending angle of the second magnet.

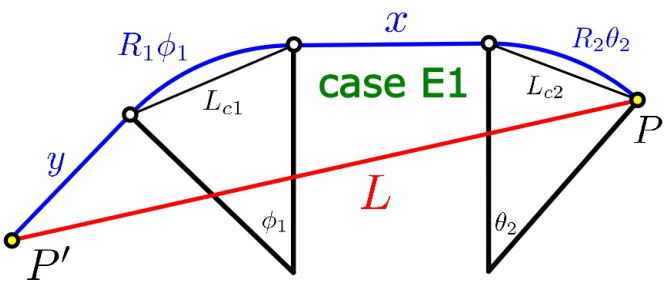

Figure 4.4: (Color) Geometry for case E1.

Since case E is an extension of case C, we will apply a similar derivation

procedure. Using the same coordinate system as in case C, we now have:

$$\mathbf{n} = \langle \cos\theta_2, -\sin\theta_2, 0 \rangle, \tag{4.45}$$

$$\mathbf{n}' = \langle \cos\phi_1, \sin\phi_1, 0 \rangle, \tag{4.46}$$

$$L_x = (y\cos\phi_1 + L_{c1}\cos\frac{\phi_1}{2} + x + L_{c2}\cos\frac{\theta_2}{2}), \tag{4.47}$$

$$L_y = (y\sin\phi_1 + L_{c1}\sin\frac{\phi_1}{2} - L_{c2}\sin\frac{\theta_2}{2}), \tag{4.48}$$

in which L_{c1} and L_{c2} are respectively the chord length associated with $R_1\phi_1$ and $R_2\theta_2$. Expanding in small ϕ_1 and θ_2 gives:

$$L = L_s - \frac{1}{24L_s}\Big\{[R_1^2\phi_1^2 + 12(R_2\theta_2 + x)y + 4R_1\phi_1(R_2\theta_2 + x + y)\phi_1^2] \\ + 6[R_2\theta_2(R_1\phi_1 + 2y)\phi_1\theta_2] + [R_2\theta_2(4R_1\phi_1 + R_2\theta_2 + 4x + 4y)]\theta_2^2\Big\}, \tag{4.49}$$

in which $L_s = (R_1\phi_1 + R_2\theta_2 + x + y)$ for case E1. It follows that:

$$\mathcal{N}_v = \frac{L_s}{2\gamma^2} + \frac{1}{8L_s}[(3R_1\phi_1 + 2x + 4y + 2R_2\theta_2)\phi_1 + (4R_1\phi_1 + 4x + 4y + 3R_2\theta_2)\theta_2] \\ \times (R_1\phi_1^2 + 2x\phi_1 + 2R_2\phi_1\theta_2 + R_2\theta_2^2), \tag{4.50}$$

$$\mathcal{D} = \frac{L_s}{2\gamma^2} + \frac{1}{8L_s}(R_1\phi_1^2 + 2x\phi_1 + 2R_2\phi_1\theta_2 + R_2\theta_2^2)^2. \tag{4.51}$$

In the limit of

$$\gamma^2 \gg L_s/(\phi_1 + \theta_2)(R_1\phi_1^2 + 2x\phi_1 + 2R_2\phi_1\theta_2 + R_2\theta_2^2), \tag{4.52}$$

the dominant term again comes from the velocity field. As in case C, we take the additional limit of large y (i.e. $y \gg R_1\phi_1, x, R_2\theta_2$), and the wake reduces to:

$$w = \frac{256ke^2\gamma^4y^3(\phi_1 + \theta_2)(R_1\phi_1^2 + 2x\phi_1 + 2R_2\phi_1\theta_2 + R_2\theta_2^2)}{[4y^2 + \gamma^2(R_1\phi_1^2 + 2x\phi_1 + 2R_2\phi_1\theta_2 + R_2\theta_2^2)^2]^3}. \tag{4.53}$$

One can verify that $y_p = \frac{1}{2}\gamma(R_1\phi_1^2 + 2x\phi_1 + 2R_2\phi_1\theta_2 + R_2\theta_2^2)$ maximizes $w(y)$ in Eq. (4.53). If the second magnet is removed (i.e. $\theta_2 = 0$), Eq. (4.53) reduces to

Eq. (4.39) in case C. In the limit of large y we also have:

$$\Delta = \frac{y}{2\gamma^2} + \frac{1}{6}\left[(R_1\phi_1 + 3x)\phi_1^2 + R_2\theta_2(3\phi_1^2 + 3\phi_1\theta_2 + \theta_2^2)\right] - \frac{1}{8y}(R_1\phi_1^2 + 2x\phi_1 + 2R_2\phi_1\theta_2 + R_2\theta_2^2)^2 + O(1/y^2). \quad (4.54)$$

As before, the constant term in Δ gives the location of the dirac delta function. The normalization factor A is:

$$A = \int_0^\infty w(y)\frac{\partial\Delta}{\partial y}dy = \frac{4ke^2(\phi_1 + \theta_2)}{R_1\phi_1^2 + 2x\phi_1 + 2R_2\phi_1\theta_2 + R_2\theta_2^2}. \quad (4.55)$$

So the approximated wake expression for case E1 is:

$$W(s) = \frac{4ke^2(\phi_1 + \theta_2)}{R_1\phi_1^2 + 2x\phi_1 + 2R_2\phi_1\theta_2 + R_2\theta_2^2} \times \lambda(s - \frac{1}{6}\left[(R_1\phi_1 + 3x)\phi_1^2 + R_2\theta_2(3\phi_1^2 + 3\phi_1\theta_2 + \theta_2^2)\right]). \quad (4.56)$$

Let us examine some limiting cases. First, if we set $\theta_2 = 0$, we recover the $W(s)$ for case C as expected (See Eq. (4.44)). If we instead remove the first magnet by setting $\phi_1 = 0$, we recover case A with only the second magnet (See Eq. (4.26) with $\theta \to \theta_2$). Another interesting limit is to set $x = 0$ and $R_1 = R_2 = R$. This physically corresponds to removing the drift between the two magnets and merging the two magnets. The result is:

$$W(s) = \frac{4ke^2}{R(\phi_1 + \theta_2)}\lambda\left(s - \frac{1}{6}R(\phi_1 + \theta_2)^3\right). \quad (4.57)$$

As expected, we recover the $W(s)$ for case A with the observation point located at $\theta = (\phi_1 + \theta_2)$ into the merged magnet. Similar to case C and case A, there are limitations in applying Eq. (4.56). The length of the drift in front of the first magnet has to be much greater than y_p. Also, the assumption of large γ in Eq. (4.52) requires $(\phi_1 + \theta_2)$ to be not small.

Case E2

In contrast to case E1, the second magnet has a bending direction *opposite* to the first magnet. With our coordinate system the vector **n** now becomes $\langle \cos\theta_2, \sin\theta_2, 0 \rangle$. Following the same derivation procedure as in case E1, we obtain:

$$W(s) = \frac{4ke^2(\phi_1 - \theta_2)}{R_1\phi_1^2 + 2x\phi_1 + 2R_2\phi_1\theta_2 - R_2\theta_2^2} \times \lambda\left(s - \frac{1}{6}\left[(R_1\phi_1 + 3x)\phi_1^2 + R_2\theta_2(3\phi_1^2 - 3\phi_1\theta_2 + \theta_2^2)\right]\right). \quad (4.58)$$

As expected, the result is very similar to case E1, with $\theta_2 \to -\theta_2$. However, the term $R_2\theta_2$ remains unchanged since it comes from the path length and is always positive.

Case G1 and G2

Similar to case E, there are two subcases in case G depending on the two bending directions. The geometry for case G1 is shown in Fig. 4.5. The observation point P is now located a distance x_2 down the second magnet. Let ϕ_2 denote the total bending angle of the second magnet.

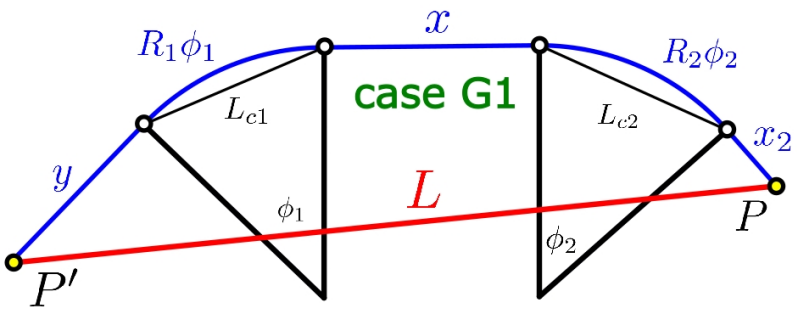

Figure 4.5: (Color) Geometry for case G1.

With the same derivation procedure as in case E1 and E2, we obtain:

$$W(s) = \frac{4ke^2(\phi_1 \pm \phi_2)}{R_1\phi_1^2 + 2x\phi_1 + 2R_2\phi_1\phi_2 \pm R_2\phi_2^2 + 2x_2(\phi_1 \pm \phi_2)} \times \lambda(s - \frac{1}{6}[(R_1\phi_1 + 3x)\phi_1^2 + R_2\phi_2(3\phi_1^2 \pm 3\phi_1\phi_2 + \phi_2^2) + 3x_2(\phi_1 \pm \phi_2)^2]). \quad (4.59)$$

Note that the $\pm$ sign denotes " $+$ " for case G1 (when the two magnets bend in the same direction) and " $-$ " for case G2 (with opposite bending directions). One can verify that for $x_2 = 0$, we recover the expressions for case E1 and E2. If we merge the two magnets by taking $x = 0$ and $R_1 = R_2 = R$, then case G1 reduces to case C with $\phi = \phi_1 + \phi_2$, as expected.

4.1.2 Even cases

We will first re-derive the wake expression for case B and D, then apply a similar formulation to obtain the expressions for case F and H.

Case B

The geometry for case B is shown in Fig. 4.6. The point P' and P are inside the same magnet separated by an angle θ.

Since P' is inside a bend, the tail electron at the retarded time has an centripetal acceleration with magnitude $|\mathbf{a}'| = \beta^2c^2/R$. This adds the first extra term to the wake:

$$w = ke^2\left(\frac{\mathcal{N}_a}{\mathcal{D}^3} + \frac{1}{\gamma^2}\left(\frac{\mathcal{N}_v}{\mathcal{D}^3} - \frac{1}{\Delta^2}\right)\right), \quad (4.60)$$

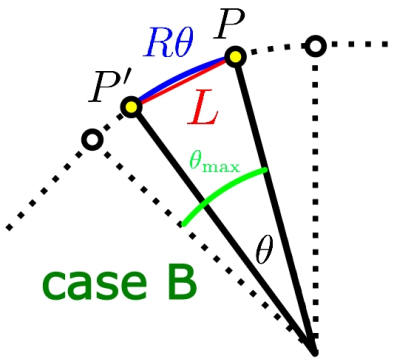

Figure 4.6: (Color) Geometry for case B. Note that the θ here is *not* the same as the θ defined in case A. The $\theta_{\max}$ here corresponds to the θ in case A.

in which $\mathcal{N}_a \equiv \beta \mathbf{n} \cdot (\mathbf{L} \times [(\mathbf{L} - L\beta \mathbf{n}') \times \mathbf{a}'])/c^2$. We first fix our coordinate system by choosing $\mathbf{n} = \langle 1, 0, 0 \rangle$, then we have:

$$\mathbf{n}' = \langle \cos\theta, \sin\theta, 0 \rangle, \tag{4.61}$$

$$\mathbf{a}' = \frac{\beta^2 c^2}{R} \langle -\sin\theta, \cos\theta, 0 \rangle, \tag{4.62}$$

$$\mathbf{L} = \langle (L_c \cos(\theta/2)), (L_c \sin(\theta/2)), 0 \rangle. \tag{4.63}$$

Expanding in small θ, keeping $R\theta$ constant, gives:

$$L = L_s - \frac{R\theta^3}{24}, \tag{4.64}$$

$$\mathcal{N}_a = \frac{-L_s}{2\gamma^2} \frac{(R\theta)}{2R} \theta + \frac{(R\theta)^2}{16R} \theta^3, \tag{4.65}$$

$$\mathcal{N}_v = \frac{L_s}{2\gamma^2} + \frac{3R\theta^3}{8}, \tag{4.66}$$

$$\mathcal{D} = \frac{L_s}{2\gamma^2} + \frac{R\theta^3}{8}, \tag{4.67}$$

in which $L_s = R\theta$ for case B. Note that while *even* terms in θ survive in L, $\mathcal{N}_v$, and $\mathcal{D}$, *odd* terms survive in $\mathcal{N}_a$, and it is required to keep the expansion up to order θ^3 in $\mathcal{N}_a$. The expression for $\mathcal{N}_a$ is *not* simplified to explicitly show this observation, and the R in the denominator comes directly from $\mathbf{a}'$ and therefore does not have a θ associated with it. It follows that:

$$w = \frac{32ke^2\gamma^4}{R^2} \left[\frac{\gamma^2\theta^2 - 4}{(\gamma^2\theta^2 + 4)^3} + \frac{2}{\gamma^2\theta^2} \left(\frac{3\gamma^2\theta^2 + 4}{(\gamma^2\theta^2 + 4)^3} - \frac{9}{(\gamma^2\theta^2 + 12)^2} \right) \right], \tag{4.68}$$

which agrees with Eq.(36) in [22]. For $\gamma\theta \ll 1$, the wake reduces to:

$$w(\gamma\theta \ll 1) = \frac{-4ke^2\gamma^4}{3R^2}. \tag{4.69}$$

The physical significance of this result has been discussed in [22]. Here we are interested in the case with $\gamma\theta \gg 1$, for which the acceleration field term dominates:

$$w(\gamma\theta \gg 1) = \frac{32ke^2}{R^2\theta^4}. \tag{4.70}$$

In the limit of large γ we also have:

$$\Delta = L_s - \beta L = \frac{L_s}{2\gamma^2} + \frac{R\theta^3}{24} \to \frac{R\theta^3}{24} \tag{4.71}$$

To solve for $W(s) = \int w(s-s')\lambda(s')ds'$ one can simply write down $w(\Delta)$ by inverting Eq. (4.71). However, for later cases with more complicated geometry, $w(\Delta)$ cannot be easily inverted. As shown in [23], a more general method is to apply integration by parts. This requires us to find the function u such that $\partial u/\partial s' = w(s-s')$. Since both w and Δ are functions of the independent variable θ, we can compute:

$$\frac{du}{d\theta} = \frac{\partial u}{\partial s'}\frac{ds'}{d\theta} = -w\frac{d\Delta}{d\theta} = \frac{-4ke^2}{R\theta^2}, \tag{4.72}$$

in which the minus sign is present because $\Delta = s - s'$. Integration over θ gives $u = 4ke^2/R\theta$, which turns out to be the same as the normalization factor A in case A (see Eq. (4.23)). Note that the limit of integration is $(s - \Delta_{\text{max}}) < s' < s$, in which $\Delta_{\text{max}} = \Delta(\theta = \theta_{\text{max}}) = R\theta_{\text{max}}^3/24$. When $\theta = \theta_{\text{max}}$, the point P' is located at the entrance of the magnet. One can also interpret θ_{max} as the entrance angle of the observation point P, which is exactly the "θ" defined in case A. For

$s' < (s - \Delta_{\max})$, one needs to use results from part A. It follows that:

$$W(s) = (u\lambda)\Big|_{s-\Delta_{\max}}^{s} - \int_{s-\Delta_{\max}}^{s} u\frac{\partial\lambda(s')}{\partial s'}ds' \tag{4.73}$$

$$= -4ke^2\left[\frac{\lambda(s-\Delta_{\max})}{R\theta_{\max}} + \int_{s-\Delta_{\max}}^{s}\frac{1}{R\theta}\frac{\partial\lambda(s')}{\partial s'}ds'\right], \tag{4.74}$$

which agrees with Eq. (6) in [23]. To apply this expression, it is required that $\gamma\theta \gg 1$, so the observation point P cannot be too close to the magnet's entrance. The expression overlooks the wake contributions from $\theta \sim 1/\gamma$ or even smaller θ. As discussed in case A, these contributions can be calculated numerically. For a very large γ these contributions can be ignored.

Case D

The geometry for case D is shown in Fig. 4.7. The point P' is located at an angle θ measured from the $exit$ of the magnet.

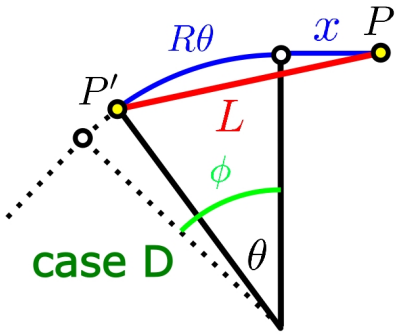

Figure 4.7: (Color) Geometry for case D. Note that the θ here is not the θ defined in either case A or B.

Since Case D is an extension of case B, we will apply a similar derivation process. Let us again choose $\mathbf{n} = \langle 1, 0, 0\rangle$, then $\mathbf{n}'$ and $\mathbf{a}'$ are the same as in case B, and:

$$\mathbf{L} = \langle (L_c\cos(\theta/2) + x), (L_c\sin(\theta/2)), 0\rangle. \tag{4.75}$$

Expanding in small θ gives:

$$L = L_s - \frac{R\theta^3}{24}\frac{(R\theta+4x)}{L_s}, \tag{4.76}$$

$$\mathcal{N}_a = \frac{-L_s}{2\gamma^2}\frac{\theta^2}{2} + \frac{\theta^4}{16}\frac{(R\theta+2x)^2}{(R\theta+x)}, \tag{4.77}$$

$$\mathcal{N}_v = \frac{L_s}{2\gamma^2} + \frac{(3R^2\theta^2+8R\theta x+4x^2)\theta^2}{8(R\theta+x)}, \tag{4.78}$$

$$\mathcal{D} = \frac{L_s}{2\gamma^2} + \frac{(R\theta+2x)^2\theta^2}{8L_s}, \tag{4.79}$$

in which $L_s = R\theta + x$ in case D. One can verify that as $x \to 0$, these quantities reduce to the ones in case B. It follows that:

$$\begin{aligned} w = 32ke^2\gamma^4 L_s^2 \Bigg[& \frac{(\gamma^2\theta^2(R\theta+2x)^2 - 4L_s^2)\theta^2}{[\gamma^2\theta^2(R\theta+2x)^2+4L_s^2]^3} \\ & + \frac{2}{\gamma^2}\left(\frac{\gamma^2\theta^2(3R^2\theta^2+8R\theta x+4x^2)+4L_s^2}{[\gamma^2\theta^2(R\theta+2x)^2+4L_s^2]^3} - \frac{9}{[\gamma^2\theta^2 R\theta(R\theta+4x)+12L_s^2]^2}\right)\Bigg], \end{aligned} \tag{4.80}$$

which agrees with Eq.(36) in [22]. If we set $x = 0$, the wake reduces to the one in case B. To focus on case D we assume $x > 0$ from now on. In the limit $\theta \to 0$, the wake vanishes:

$$w(\theta \to 0) = \left[0 + \frac{4\gamma^2}{x^2} - \frac{4\gamma^2}{x^2}\right] = 0, \tag{4.81}$$

regardless of the value of γ. As in case B, we are interested in the limit $\gamma\theta \gg 1$, for which the acceleration field term dominates:

$$w(\gamma\theta \gg 1) = 32ke^2\frac{(R\theta+x)^2}{\theta^2(R\theta+2x)^4}. \tag{4.82}$$

In a more strict limit of $\gamma^2 \gg (R\theta+x)/R\theta^3$ we have:

$$\Delta = \frac{R\theta^3}{24}\frac{(R\theta+4x)}{R\theta+x}. \tag{4.83}$$

To solve for $W(s)$ we need to find the function u such that $\partial u/\partial s' = w(s-s')$. Similar to case B, we have:

$$\frac{du}{d\theta} = \frac{\partial u}{\partial s'}\frac{ds'}{d\theta} = -w\frac{d\Delta}{d\theta} = \frac{-4ke^2R}{(R\theta+2x)^2}, \tag{4.84}$$

Integration over θ gives $u = 4ke^2/(R\theta + 2x)$. We again observe that u is the same quantity as the normalization factor A in case C. We are now ready to apply integration by parts to find $W(s)$. Note that the region of integration is $(s - \Delta_{\text{max}}) < s' < (s - \Delta_{\text{min}})$, in which $\Delta_{\text{max}} = \Delta(\theta = \theta_{\text{max}})$ and $\Delta_{\text{min}} = \Delta(\theta = 0) = 0$. Since θ in case D is measured from the $exit$ of the magnet, we have $\theta_{\text{max}} = \phi$, the total bending angle of the magnet. It follows that:

$$W(s) = (u\lambda)\Big|_{s-\Delta_{\text{max}}}^{s} - \int_{s-\Delta_{\text{max}}}^{s} u\frac{\partial\lambda(s')}{\partial s'}ds' \tag{4.85}$$

$$= -4ke^2\left[\frac{\lambda(s-\Delta_{\text{max}})}{R\phi + 2x} + \int_{s-\Delta_{\text{max}}}^{s}\frac{1}{R\theta + 2x}\frac{\partial\lambda(s')}{\partial s'}ds'\right]. \tag{4.86}$$

The result agrees with Eq. (15) [23]. Note that one of the boundary term $u\lambda$ ($s' \to s$) vanishes since $w(\theta \to 0) = 0$. One can check that if the observation point P is located at the exit of the magnet (i.e. $x = 0, \phi = \theta_{\text{max}}$), we recover the result of case B. For large x, the expression vanishes as expected. When using equation Eq. (4.86), one should abide to the limit $\gamma^2 \gg (R\theta + x)/R\theta^3$. This means for a very large x value, $W(s)$ can give inaccurate results.

Case F1

Fig. 4.8 shows the geometry for case F1. In terms of the location of the observation point, case F1 and E1 are the same. Similar to case E1, case F1 has two magnets bending in the same direction. For opposite bending directions, see case F2 in the following subsection. The geometry for case F1 is shown in Fig. 4.8.

Since case F is an extension of case D, we follow similar derivations. With

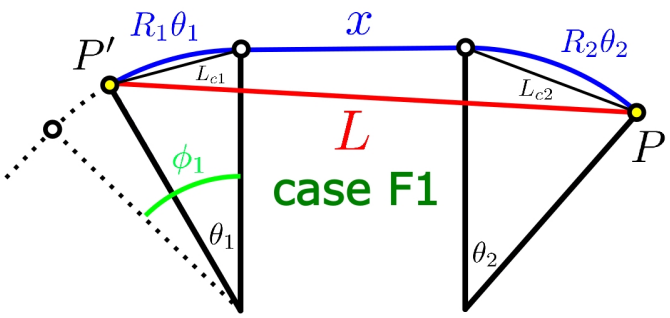

Figure 4.8: (Color) Geometry for case F1.

the coordinate system defined in case E1, we now have:

$$\mathbf{n} = \langle \cos\theta_2, -\sin\theta_2, 0 \rangle, \tag{4.87}$$

$$\mathbf{n}' = \langle \cos\theta_1, \sin\theta_1, 0 \rangle, \tag{4.88}$$

$$\mathbf{a}' = \frac{\beta^2 c^2}{R} \langle -\sin\theta, \cos\theta, 0 \rangle, \tag{4.89}$$

$$L_x = (L_{c1}\cos\frac{\theta_1}{2} + x + L_{c2}\cos\frac{\theta_2}{2}) \tag{4.90}$$

$$L_y = (L_{c1}\sin\frac{\theta_1}{2} - L_{c2}\sin\frac{\theta_2}{2}). \tag{4.91}$$

From case B and D we know for large γ the dominant term in w is the acceleration field term:

$$w = \frac{32ke^2\gamma^4 L_s^2}{R_1}(R_1\theta_1^2 + 2R_1\theta_1\theta_2 + 2x\theta_2 + R_2\theta_2^2)\times \\ \frac{\gamma^2(R_1\theta_1^2 + 2R_2\theta_1\theta_2 + 2x\theta_1 + R_2\theta_2^2)^2 - 4L_s^2}{[\gamma^2(R_1\theta_1^2 + 2R_2\theta_1\theta_2 + 2x\theta_1 + R_2\theta_2^2)^2 + 4L_s^2]^3}, \tag{4.92}$$

in which $L_s = (R_1\theta_1 + x + R_2\theta_2)$ for case F. Note that $w(x \to \infty) \propto 1/x \to 0$ as expected. Assuming R_1 and R_2 are on the same order of magnitude ($R_1 \approx R_2 \approx R$), then in the limits of $\gamma(\theta_1 + \theta_2) \gg 1$ we have:

$$w = \frac{32ke^2 L_s^2}{R_1}\frac{(R_1\theta_1^2 + 2R_1\theta_1\theta_2 + 2x\theta_2 + R_2\theta_2^2)}{(R_1\theta_1^2 + 2R_2\theta_1\theta_2 + 2x\theta_1 + R_2\theta_2^2)^4}, \tag{4.93}$$

Note that the numerator and denominator of w do *not* cancel. With a more strict

limit of $\gamma^2 \gg L_s/R(\theta_1+\theta_2)^3$ we have:

$$\Delta = \frac{1}{24L_s}[R_1\theta_1^3(R_1\theta_1+4x+4R_2\theta_2)+6R_1\theta_1^2R_2\theta_2^2+R_2\theta_2^3(4R_1\theta_1+4x+R_2\theta_2)], \tag{4.94}$$

To find $W(s)$ we again look for the function u such that $\partial u/\partial s' = w(s-s')$. It follows that:

$$\frac{du}{d\theta_1} = -4ke^2\frac{(R_1\theta_1^2+2R_1\theta_1\theta_2+2x\theta_2+R_2\theta_2^2)}{(R_1\theta_1^2+2R_2\theta_1\theta_2+2x\theta_1+R_2\theta_2^2)^2}, \tag{4.95}$$

$$u = \frac{4ke^2(\theta_1+\theta_2)}{R_1\theta_1^2+2R_2\theta_1\theta_2+2x\theta_1+R_2\theta_2^2}. \tag{4.96}$$

Again, we see that u equals to A in the pairing case E1. Integration by parts gives:

$$\begin{aligned} W(s) = -4ke^2\Bigg[&-\frac{\lambda(s-\Delta_{\text{min}})}{R_2\theta_2} \\ &+\frac{(\phi_1+\theta_2)\lambda(s-\Delta_{\text{max}})}{R_1\phi_1^2+2R_2\phi_1\theta_2+2x\phi_1+R_2\theta_2^2} \\ &+\int_{s-\Delta_{\text{max}}}^{s-\Delta_{\text{min}}}\frac{(\theta_1+\theta_2)}{R_1\theta_1^2+2R_2\theta_1\theta_2+2x\theta_1+R_2\theta_2^2}\frac{\partial\lambda(s')}{\partial s'}ds'\Bigg], \end{aligned} \tag{4.97}$$

in which $\Delta_{\text{max}} = \Delta(\theta_1=\phi_1,\theta_2)$ and

$$\Delta_{\text{min}} = \Delta(\theta_1=0,\theta_2) = \frac{R_2\theta_2^3}{24}\frac{R_2\theta_2+4x}{R_2\theta_2+x}. \tag{4.98}$$

The first term in $W(s)$, which corresponds to the integration boundary at $\theta_1 = 0$, might look physically invalid since it diverges for $\theta_2 \to 0$ and does *not* vanish for $x \to \infty$. However due to the required limit of $\gamma^2 \gg L_s/R(\theta_1+\theta_2)^3$, one simply can *not* apply Eq. (4.97) with a very small θ_2 or large x. For $\theta_2 \to 0$, one should simply apply case D. For $x \to \infty$ we know the wake vanishes, and the two magnets should be considered "decoupled". To test the validity of Eq. (4.97), let us consider a case with $x = 0$ and $R_1 = R_2 = R$. This equivalently merges

the two magnets into one, and the point P is located $(\phi_1 + \theta_2)$ into the merged magnet. To compute the $W(s)$ at point P due to the merged magnet, we need to add the contribution from the first sub-magnet using case F and the second sub-magnet using case B. Applying Eq. (4.97) and Eq. (4.74) respectively gives:

$$\begin{aligned} W(s) &= W_{\mathrm{B}}(s, \theta_{\mathrm{max}} = \theta_2) + W_{\mathrm{F1}}(s, x = 0) \\ &= -4ke^2 \left[\frac{\lambda(s - \Delta_{\mathrm{B,max}})}{R\theta_2} + \int_{s-\Delta_{\mathrm{B,max}}}^{s} \frac{1}{R\theta} \frac{\partial \lambda(s')}{\partial s'} ds' \right] \\ &- 4ke^2 \left[-\frac{\lambda(s - \Delta_{\mathrm{F,min}})}{R_2\theta_2} + \frac{\lambda(s - \Delta_{\mathrm{F,max}})}{R(\phi_1 + \theta_2)} + \int_{s-\Delta_{\mathrm{F,max}}}^{s-\Delta_{\mathrm{F,min}}} \frac{1}{R(\theta_1 + \theta_2)} \frac{\partial \lambda(s')}{\partial s'} ds' \right], \end{aligned} \tag{4.99}$$

The quantity θ here denotes the angle measured from point P backward, so $\theta_1 = (\theta - \theta_2)$ in W_{F1}. Since $\Delta_{\mathrm{F,max}}(x = 0) = R(\phi_1 + \theta_2)^3/24 = \Delta_{\mathrm{B}}(\theta = \phi_1 + \theta_2)$, the two integrals can be merged into one. Also, since $\Delta_{\mathrm{F,min}}(x = 0) = R\theta_2^3/24 = \Delta_{\mathrm{B,max}}(\theta_{\mathrm{max}} = \theta_2)$, the first term in W_{F1} cancels with the boundary term in W_{B} (since they have the opposite sign), giving:

$$W(s) = -4ke^2 \left[\frac{\lambda(s - \Delta_{\mathrm{B}}(\theta = \phi_1 + \theta_2))}{R(\phi_1 + \theta_2)} + \int_{s-\Delta_{\mathrm{B}}(\theta=\phi_1+\theta_2)}^{s} \frac{1}{R\theta} \frac{\partial \lambda(s')}{\partial s'} ds' \right]. \tag{4.100}$$

As expected, we have recovered case B for the merged magnet with an entrance angle of $(\phi_1 + \theta_2)$. This validates our wake expression for case F1, and the first boundary term in Eq. (4.97) is necessary in this formulation. Without this term to cancel the boundary term in case B, one could generate free wakes by splitting the magnet into small magnets, which is not physical.

Case F2

Similar to E2, the two magnets now bend in the opposite direction. With the same derivation procedure as in case F1, we obtain:

$$W(s) = -4ke^2\left[-\frac{\lambda(s-\Delta_{\min})}{R_2\theta_2} + \frac{(\phi_1-\theta_2)\lambda(s-\Delta_{\max})}{R_1\phi_1^2 + 2R_2\phi_1\theta_2 + 2x\phi_1 - R_2\theta_2^2} + \int_{s-\Delta_{\max}}^{s-\Delta_{\min}} \frac{(\theta_1-\theta_2)}{R_1\theta_1^2 + 2R_2\theta_1\theta_2 + 2x\theta_1 - R_2\theta_2^2}\frac{\partial\lambda(s')}{\partial s'}ds'\right], \quad (4.101)$$

The result is very similar to case F1, again with $\theta_2 \to -\theta_2$ and $R_2\theta_2$ unchanged.

Case H1 and H2

Similar to case F, there are two subcases in case H depending on the two bending directions. Fig. 4.9 shows the geometry for case H1 in which the two magnets bend in the same direction. The observation point P is located at a distance x_2 down the second magnet, just like in case G.

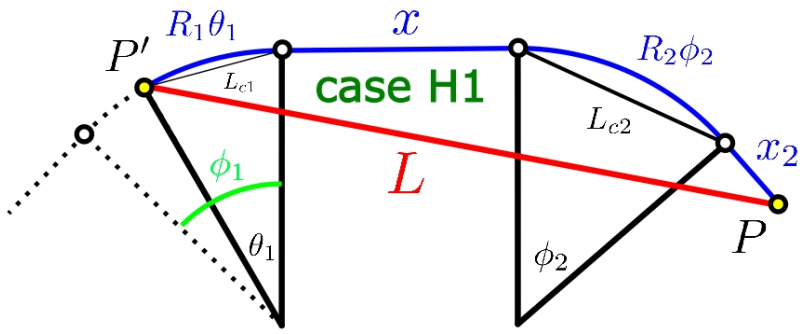

Figure 4.9: (Color) Geometry for case H1.

We follow the same derivation procedure as in case F1 and F2. In the limit of $\gamma^2 \gg L_s/R(\theta_1+\phi_2)^3$ we have:

$$\Delta = \frac{1}{24L_s}[R_1\theta_1^3(R_1\theta_1 + 4x + 4R_2\phi_2 + 4x_2) \pm 6R_1\theta_1^2\phi_2(R_2\phi_2 + 2x_2) + R_2\phi_2^3(4R_1\theta_1 + 4x + R_2\phi_2) + 4x_2\phi_2^2(3R_1\theta_1 + 3x + R_2\phi_2)], \quad (4.102)$$

$$w = \frac{32ke^2L_s^2(R_1\theta_1^2 \pm 2R_1\theta_1\phi_2 \pm 2x\phi_2 \pm R_2\phi_2^2)}{R_1(R_1\theta_1^2 + 2R_2\theta_1\phi_2 + 2x\theta_1 \pm R_2\phi_2^2 + 2x_2(\theta_1 \pm \phi_2))^4}, \tag{4.103}$$

$$u(\theta_1) = \frac{4ke^2(\theta_1 \pm \phi_2)}{R_1\theta_1^2 + 2R_2\theta_1\phi_2 + 2x\theta_1 \pm R_2\phi_2^2 + 2x_2(\theta_1 \pm \phi_2)}. \tag{4.104}$$

Integration by parts gives:

$$W(s) = -\left[-u(0)\lambda(s - \Delta_{\text{min}}) + u(\phi_1)\lambda(s - \Delta_{\text{max}}) + \int_{s-\Delta_{\text{max}}}^{s-\Delta_{\text{min}}} u(\theta_1)\frac{\partial\lambda(s')}{\partial s'}ds'\right]. \tag{4.105}$$

Again, the $\pm$ sign denotes "$+$" for case H1 and "$-$" for case H2. Similar to case F, one cannot apply this expression for small ϕ_2 or large x. One can verify that for $x_2 = 0$, we recover the wake expressions for case E1 and E2.

4.2 Theory v.s Simulation

To test the formulas derived for all cases, we run CSR simulations in Bmad for four different beamlines (details on Bmad simulation and parameter choice are described in Section IV). Each beamline consists of only drifts and bending magnet(s) with lengths described by Table I.

Length (mm)	D0	B1	D1	B2	D2
Beamline A	60	500	600	X	X
Beamline B	60	133	600	X	X
Beamline C	60	133	70	500	X
Beamline D	60	133	70	122	600

Table 4.1: The length of each element in the four beamlines. In the element names,"D" denotes a drift, and "B" denotes a bending magnet. Each beamline starts with drift D0, followed by B1, D1, B2, then D2. The symbol "X" means that the element is absent.

In this section we redefine s to be the longitudinal position of the bunch center from the beginning of the beamline. The old s is replaced by symbol z

to avoid confusion. For each beamline we will track a Gaussian bunch ($\sigma_z = 1.078$ mm) and compare the evolution of the wakefield $W(z)$ with the theory. For easy comparison with other literature, we normalize $W(z)$ in all the plots by the characteristic CSR wake [28]:

$$W_0 = \frac{kQe}{(R^2\sigma_z^4)^{1/3}}, \tag{4.106}$$

in which Q is the bunch charge, and $N_p = Q/e$ is the number of electrons in the bunch. We choose a small bunch charge of $Q = 1.0$ pC so that the longitudinal distribution $\lambda(z)$ remains Gaussian during the transport. Note that in general $\int \lambda(z)dz = N_p$. The electron energy is chosen to be 42 MeV, which corresponds to $\gamma = 82.2$ for electrons. The two magnets bend in the $opposite$ direction, and the bending radii are $R_1 = 0.808$ m and $R_2 = 0.487$ m. With R set to R_1 in Eq. (4.106), we have $W_0 = 1.50 \times 10^{-17}$ J/m $= 93.7$ eV/m. To see the wake propagation over a reasonable length scale, the final element(s) in each beamline have been made sufficiently long. The length of the first drift D0 does not play a role since any drift before the first magnet is assumed to be infinitely long in the CSR simulation of Bmad.

4.2.1 Beamline A

The purpose of beamline A and B is to confirm that Bmad simulation agrees with the previously published formulas with one bending magnet (case A,B,C, and D). The magnet in beamline A is made long (500 mm) to allow studies of the wake propagation up to the steady state (s-s). As discussed in [23], the s-s occurs when the bunch center is $L_0 = R\theta \gg (24\sigma_z R^2)^{1/3}$ into the magnet. L_0 is called the overtaking distance, and is equal to 257 mm for magnet B1. The wake

in bend B1 has contributions from case A and case B:

$$W(z) = W_{\text{B,integral}}(z, \theta_1) + W_{\text{B,boundary}}(z, \theta_1) + W_{\text{A}}(z, \theta_1), \tag{4.107}$$

in which $\theta_1 = (s - 60 \text{ mm})/R_1$ is the angle of the observation point into magnet B1. Eq. (4.107) is often referred to as the entrance wake. Fig. 4.10 below shows the wake propagation in B1 by theory and Bmad simulations, which agree well. The steady state is reached when $s \approx 520$ mm, beyond which the contribution to $W(z)$ comes solely from the $W_{\text{B,integral}}$ term, and becomes independent of θ_1.

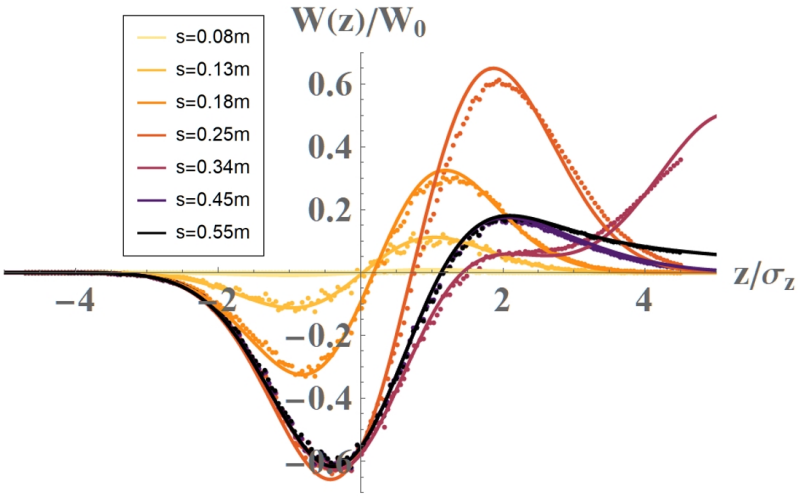

Figure 4.10: (Color) Evolution of $W(z)$ inside magnet B1 in beamline A. The curves are theory prediction using Eq. (4.107), and the dots are from Bmad simulation. The darkest curve at $s = 0.55$ m is the steady state CSR wake.

The wake in drift D1 has contributions from case C and case D:

$$W(z) = W_{\text{D,integral}}(z, x, \phi_1) + W_{\text{D,boundary}}(z, x, \phi_1) + W_{\text{C}}(z, x, \phi_1), \tag{4.108}$$

in which $x = (s - 560 \text{ mm})$ is the location of the bunch center into the drift D1. Since the s-s is already reached, the only contribution comes from the $W_{\text{D,integral}}$ term. This makes sense since for large ϕ_1 the other two terms vanish. Fig. 4.11 shows the wake propagation in D1 by theory and Bmad simulations, which again agree well. A similar benchmarking result has been shown in [26].

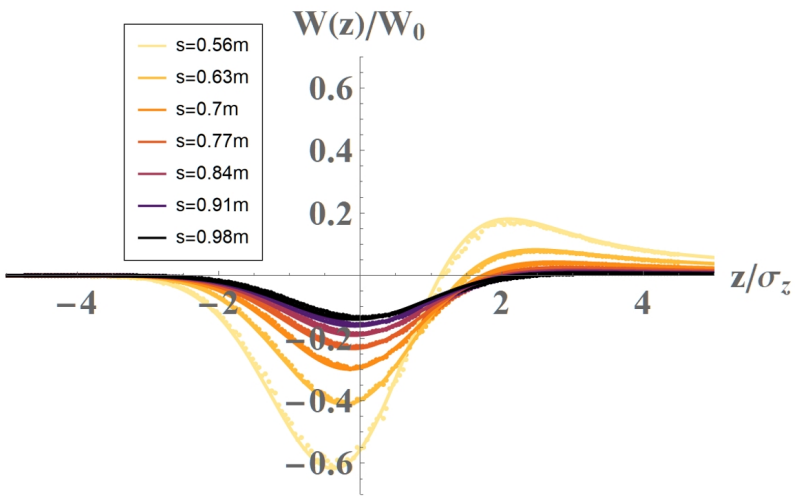

Figure 4.11: (Color) Evolution of $W(z)$ inside drift D1 in beamline A. The curves are theory prediction using Eq. (4.108), and the dots are from Bmad simulation.

4.2.2 Beamline B

In contrast to beamline A, the magnet's length in beamline B is shorter than the overtaking distance (i.e. $L_m < L_0$), so the s-s cannot be reached. This means all three terms in Eq. (4.108) contribute to the exit wake. The wake evolution in D1 is shown in Fig. 4.12 below, and we again observe agreement between theory and Bmad simulation.

4.2.3 Beamline C

The purpose of Beamline C is to test the new formulas for case E and F. The wake propagation up to D1 has been shown in beamline B, so here we will focus on $W(z)$ in B2 only. The drift length between the two magnets is made short (70 mm) so that the wake contribution from the first magnet remains significant in the second magnet. The short length also allows us to neglect the wake contribution from the drift itself, because it is the case of small y_m in Eq. (4.28). This

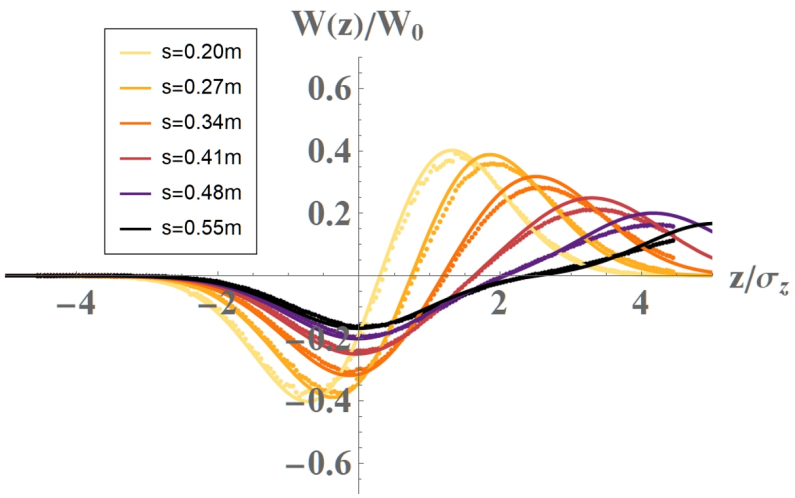

Figure 4.12: (Color) Evolution of $W(z)$ inside drift D1 in beamline B. The curves are theory prediction using Eq. (4.108), and the dots are from Bmad simulation.

neglected contribution corresponds to case A for the second magnet.

The contribution to the total $W(z)$ therefore consists of a total of six terms: 2 term from case B, 3 terms from case F2, and 1 term from case E2. Here we sort the terms into three groups:

$$W(z) = W_1(z) + W_2(z) + W_3(z), \tag{4.109}$$

$$W_1(z) = W_{\text{B,integral}}(z, \theta_2), \tag{4.110}$$

$$W_2(z) = W_{\text{B,boundary}}(z, \theta_2) + W^{\text{near}}_{\text{F2,boundary}}(z, \theta_2, x), \tag{4.111}$$

$$W_3(z) = W_{\text{F2,integral}}(z, \theta_2, x, \phi_1) + W^{\text{far}}_{\text{F2,boundary}}(z, \theta_2, x, \phi_1) + W_{\text{E2}}(z, \theta_2, x, \phi_1), \tag{4.112}$$

in which $\theta_2 = (s - 263\text{ mm})/R_2$ is the angle of the observation point into magnet B2, x is the length of drift D1, and ϕ_1 is the total bending angle of B1. $W_1(z)$ has only the integral term of case B for magnet B2. This term is responsible for the steady state CSR wake in magnet B2. $W_2(z)$ has the boundary term of case B and the $near$ boundary term of case F2. Recall that W_{F2} from Eq. (4.101) has two boundary terms. To distinguish them we call the one evaluated at $\theta_1 = \phi_1$

the $near$ term, and the one evaluated at $\theta_1 = \phi_1$ the far term. As discussed in case F, the near term and the boundary term from case B cancel each other if we merge the two magnets (i.e. $W_2(z) = 0$ if $x = 0$ and $R_1 = R_2$). $W_3(z)$ includes the rest of the contribution from magnet B1 and the long drift in front of it. One can identify all six terms in Eq. (4.112) based on their names using the tables in Appendix A.

Fig. 4.13, 4.14, and 4.15, respectively show the evolution of $W_1(z), W_2(z)$, and $W_3(z)$ in magnet B2 ($s > 263$ mm) as θ_2 increases. For comparison purposes, the three plots have the same scale, the curves are evaluated at the same longitudinal positions.

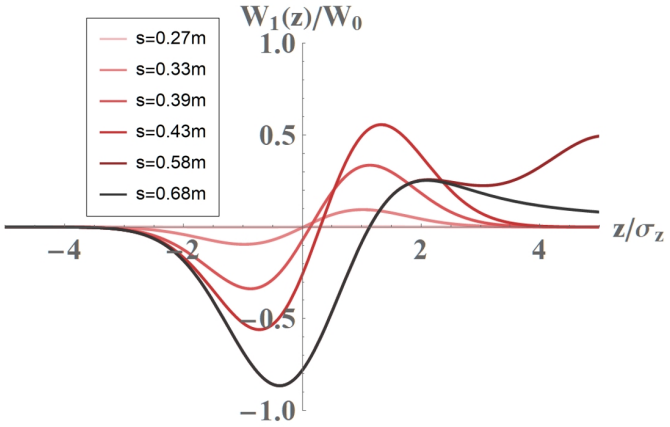

Figure 4.13: (Color) Evolution of $W_1(z)$ inside magnet B2 in beamline C by theory prediction (See Eq. (4.112).). The evolution is similar to Fig. 4.10 since they both show entrance wakes. The darkest curve at $s = 0.68$ m corresponds to the steady state wake in B2.

Fig. 4.16 shows the total wake $W(z)$ in B2 and the simulation results from Bmad. As s increases, the main contribution to $W(z)$ shifts from $W_3(z)$ to $W_2(z)$, then eventually to $W_1(z)$. This makes sense since the exit wake from B1 attenuates as the entrance wake from B2 builds up, and finally for $s = 0.68$ m the steady state wake is reached, which corresponds to the darkest curve in

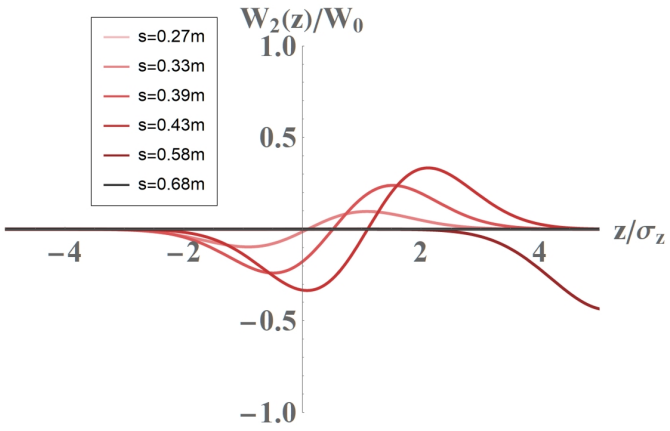

Figure 4.14: (Color) Evolution of $W_2(z)$ inside magnet B2 in beamline C by theory prediction (See Eq. (4.112).). As s increases the wake "moves" toward positive z. For the darkest curve at $s = 0.68$ m, the wake becomes insignificant for $z < 5\sigma_z$.

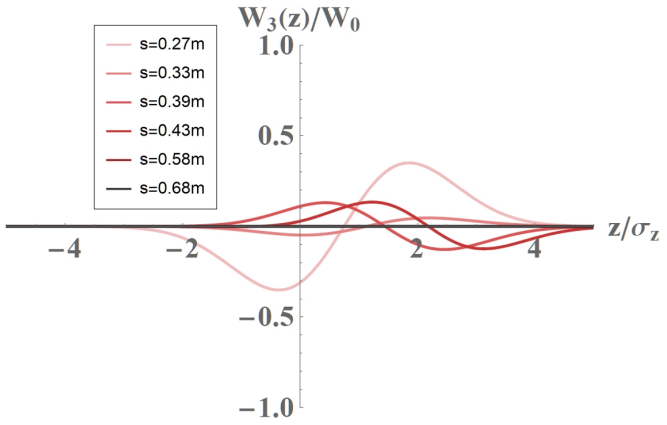

Figure 4.15: (Color) Evolution of $W_3(z)$ inside magnet B2 in beamline C by theory prediction (See Eq. (4.112).). The wake attenuates for large s since all three terms in W_3 come from the first magnet B1.

Fig. 4.13. Note that the normalization factor W_0 in all the plots depends on R_1, not R_2. This explains why the range of the steady state wake is different in Fig. 4.10 and Fig. 4.16.

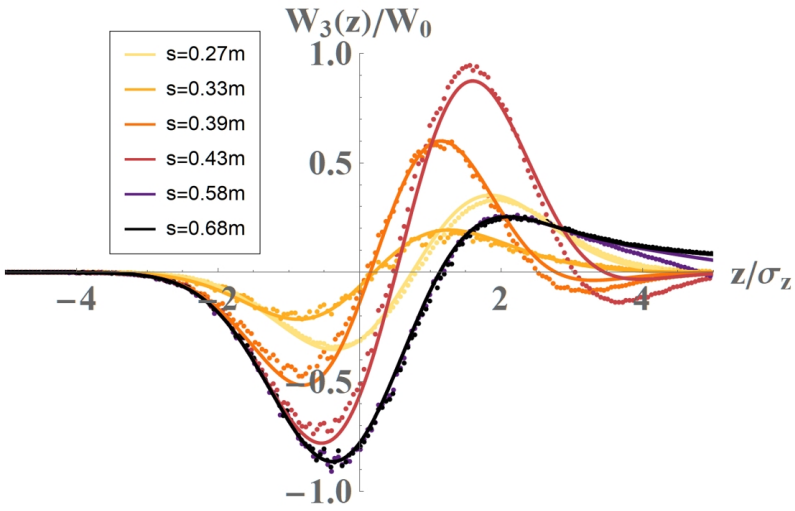

Figure 4.16: (Color) Evolution of $W(z)$ inside magnet B2 in beamline C. The curves are theory prediction using the sum of three wakes in Eq. (4.112), and the dots are from Bmad simulation.

4.2.4 Beamline D

The purpose of beamline D is to test the formulas for case G and H. Similar to beamline C, the total wake has contribution from six terms, grouped as:

$$W(z) = W_1(z) + W_2(z) + W_3(z), \tag{4.113}$$

$$W_1(z) = W_{\text{D,integral}}(z, x_2, \phi_2), \tag{4.114}$$

$$W_2(z) = W_{\text{D,boundary}}(z, x_2, \phi_2) + W^{\text{near}}_{\text{H2,boundary}}(z, x_2, \phi_2, x), \tag{4.115}$$

$$W_3(z) = W_{\text{H2,integral}}(z, x_2, \phi_2, x, \phi_1) \tag{4.116}$$

$$+W^{\text{far}}_{\text{H2,boundary}}(z, x_2, \phi_2, x, \phi_1) + W_{\text{G2}}(z, x_2, \phi_2, x, \phi_1), \tag{4.117}$$

in which $x_2 = (s - 385 \text{ mm})$ is the location of the bunch center into the drift D2, and ϕ_2 is the total bending angle of B2. The six terms are grouped in the same way as in Eq. (4.112), with the following changes in the case names: B $\to$ D, F2 $\to$ H2, and E2 $\to$ G2. Fig. 4.17, 4.18, and 4.19 respectively show the evolution of $W_1(z), W_2(z)$, and $W_3(z)$ in D2 ($s > 385$ mm) as x_2 increases.

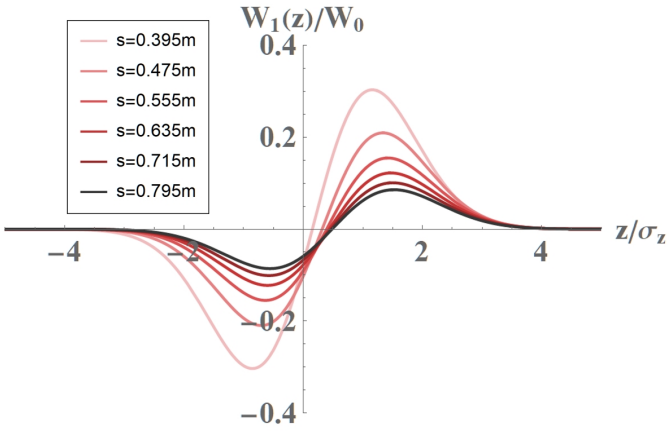

Figure 4.17: (Color) Evolution of $W_1(z)$ inside drift D2 in beamline D by theory prediction (See Eq. (4.117).). The exit wake attenuates like as expected.

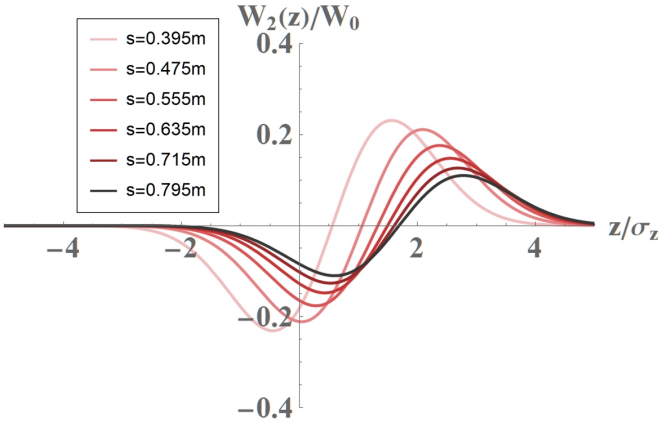

Figure 4.18: (Color) Evolution of $W_2(z)$ inside drift D2 in beamline D by theory prediction (See Eq. (4.117).). As s increases the wake "moves" toward positive z and attenuates.

Fig. 4.20 shows the total wake $W(z)$ in D2 and the simulation results from Bmad, which agree well. As s increases, the wake amplitude decreases as expected. However, one might note that the amplitude of $W_3(s)$ in Fig. 4.19 does *not* monotonically decrease for all s. This occurs because the denominator of $u(\theta_1)$ in Eq. (4.104) (and therefore $u(\phi_1)$ in Eq. (4.59) and Eq. (4.105)) changes signs as x_2 increases. This can only happen when the two magnets bend in the opposite direction, so that the denominator is not always positive and increasing with x_2.

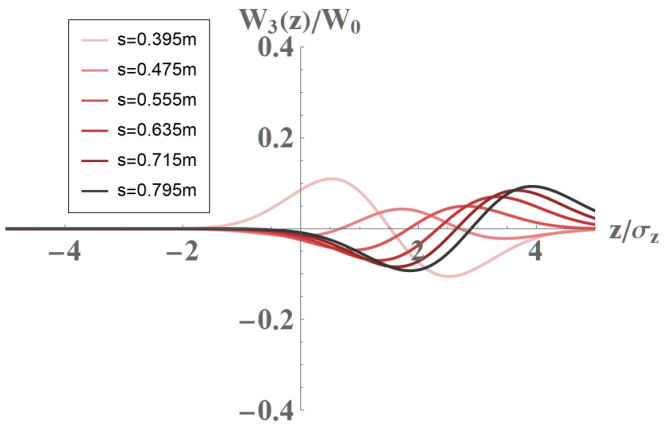

Figure 4.19: (Color) Evolution of $W_3(z)$ inside drift D2 in beamline D by theory prediction (See Eq. (4.117).). The wake eventually attenuates for large s (not shown).

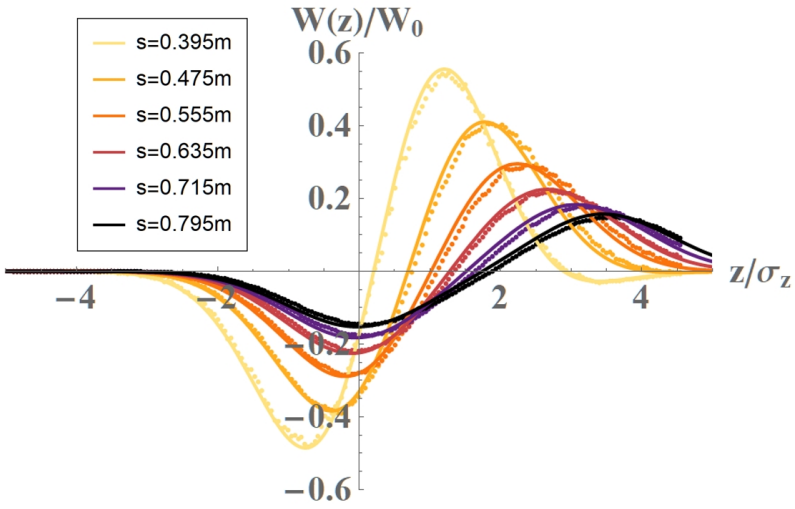

Figure 4.20: (Color) Evolution of $W(z)$ inside drift D2 in beamline D. The curves are theory prediction using the sum of three wakes in Eq. (4.117), and the dots are from Bmad simulation.

4.2.5 Discussion

Beamline A and B show that Bmad simulation agrees with the existing formulas for $W(z)$ with one bending magnet. Moreover, Beamline C and D show how to apply the new formulas for a system with two bending magnets, and agreements with simulation results support that these formulas work. Note that the

simplified formulas might give inaccurate results if γ or θ (the observation angle into either magnet) is too small, or if x (the drift length between the two magnets) is too large. In that case the un-approximated formulas have to be used. While CSR simulation in Elegant has implemented the formulas with one bending magnet, Bmad uses $none$ of these approximated formulas (See the section on CSR simulations for details.).

Rather than the traditional theory with only one magnet, the new theory has to be used whenever magnets are similarly close. In addition, one can use these formulas to calculate the energy loss $E_{\text{loss}} = \int W(z)\lambda(z)dz$ and the increase in energy spread due to CSR, as long as $\lambda(z)$ remains unchanged. In reality the longitudinal distribution $\lambda(z)$ might vary significantly due to a high bunch charge or transverse particle motions. This extension of CSR theory from one bend to two bends is essential for short-bend accelerators like CBETA. For more extreme systems with CSR extending over three or more bends, no approximated expressions have been derived using the Lienard-Wiechert formula, and numerical simulations are recommended. Alternatively, an exact 1D model using the Jefimenko's form of Maxwell's equations has been derived in [28].

4.3 Bmad CSR Simulation Overview

Subroutines have been established in Bmad to include CSR calculations [26]. Fig. 4.21 shows how Bmad divides a bunch of particles into a number of bins (N_b) in the longitudinal direction. During beam tracking, N_b is constant, and the bin width is dynamically adjusted at each time step to cover the entire bunch length. The contribution of a macro-particle to a bin's total charge is determined

by the overlap of the particle's triangular charge distribution and the bin. With Δz_b denoting the bin width and ρ_i denoting the total charge in the i^{th} bin, the charge density (λ_i) at the bin center is taken to be $\rho_i/\Delta z_b$. In between the bin centers, the charge density is assumed to vary linearly.

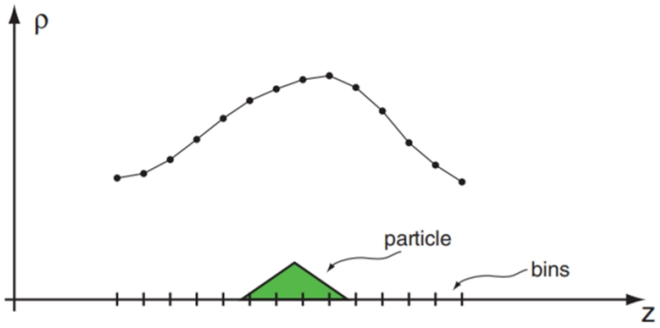

Figure 4.21: Bmad implementation of CSR. The bunch is divided into N_b bins in the longitudinal direction for calculation of CSR kicks.

With integration by parts the CSR wake seen by the bunch can be written as:

$$W(z) = \int_{-\infty}^{\infty} dz' \frac{d\lambda(z')}{dz'} I_{\text{CSR}}(z - z'), \tag{4.118}$$

in which

$$I_{\text{CSR}}(z - z') = -\int_{-\infty}^{z} w(z - z'')dz''. \tag{4.119}$$

The energy kick $\Delta\mathcal{E}$ received by a particle centered at the j^{th} bin, after travelling for a distance Δs, is therefore modelled in Bmad as [26]:

$$\Delta\mathcal{E} = \Delta s \sum_{i=1}^{N_b} (\lambda_i - \lambda_{i-1}) \frac{\hat{I}_{\text{CSR}}(j - i) + \hat{I}_{\text{CSR}}(j - i + 1)}{2}, \tag{4.120}$$

in which $\hat{I}_{\text{CSR}}(j) \equiv I_{\text{CSR}}(z = j\Delta z_b)$.

CSR calculations in Bmad within one bending magnet have been benchmarked with CSR theory and other simulation codes including A&Y, GPT, and elegant [26]. Additional benchmarking with a system of two magnets have been

shown in the previous sections. Bmad CSR simulation also allows users to include the space charge calculation for high energy and the one dimensional vacuum shielding effect. In 2017 the Bmad library was further developed, which can now handle the case when the design orbit of the beam does not follow the reference orbit of the lattice [27]. This is exactly the case for the FFA beamline in CBETA, which consists of displaced quadrupole magnets.

Given a bunch with fixed charge Q, the two most important parameters in CSR simulations are the number of particles (N_p) and bins (N_b). A large N_p generally increases the simulation accuracy at the cost of computation time. It is usually recommended to have $Np \geq$ 100k, but a beamline with more or longer curved trajectories may require more. Choosing N_b is not as straightforward as N_p. A small N_b can result in inaccurate calculation of CSR kicks due to low longitudinal resolution. However, if N_b is too large, the number of particles per bin might become too small, resulting in numerical noise. A proper choice of N_b therefore depends heavily on N_p, the bunch parameters, and the lattice itself. For the four test beamlines in the last section we have chosen $N_p = 400k$ and $N_b = 200$. For a large lattice like CBETA, convergence tests with these parameters are recommended to produce convincing results.

4.4 CBETA Simulation Results

The subsections below show the CSR simulation results with the CBETA 1-turn and 4-turn mode for various CSR parameters. We track the bunch starting at the end of the LINAC pass 1 (42 MeV) to the end of pass 8 for 4-turn mode (or pass 2 for 1-turn mode, 6 MeV). The initial bunch distribution used is either the

GPT beam or a Gaussian beam. The GPT beam has been pre-simulated using GPT tracking up to the end of the LINAC pass 1 (42 MeV) to account for the space charge effect at low energy [1]. The Gaussian beam is generated by Bmad to have the same beam optics as the GPT beam. Unless being varied or specified otherwise, the default CSR parameters used are $N_p = 10^6$, $N_b = 2500$, $Q = 5$ pC, and GPT beam as the initial bunch distribution.

4.4.1 4-turn with varying N_p

As discussed, CSR simulation results can vary significantly based on the choice of numerical parameters, especially for a large lattice like CBETA. To ensure the results are physically representative, we perform a convergence test on N_p in this section. Fig. 4.22 shows the longitudinal phase space distribution recorded at the end of LINAC pass 8 (6 MeV) with N_p varying from 10^3 to 10^6. Fig. 4.23 and Fig. 4.24 show the corresponding number of particle loss (out of 10^6) and the final rms energy spread σ_δ decrease as N_p increases. The energy spread σ_δ converges from more than 0.014 at $N_p = 100k$ to about 0.009 for $N_p > 800k$. This particular convergence test indicates that with $N_b = 2500$, $N_p > 800k$ is required to produce legitimate results for CBETA's 4-turn.

In general there can be multiple CSR parameters, and multi-dimensional convergence tests may be required to produce the most physically representative results. The following subsection shows a test on N_b for 4-turn. For more examples, see [33].

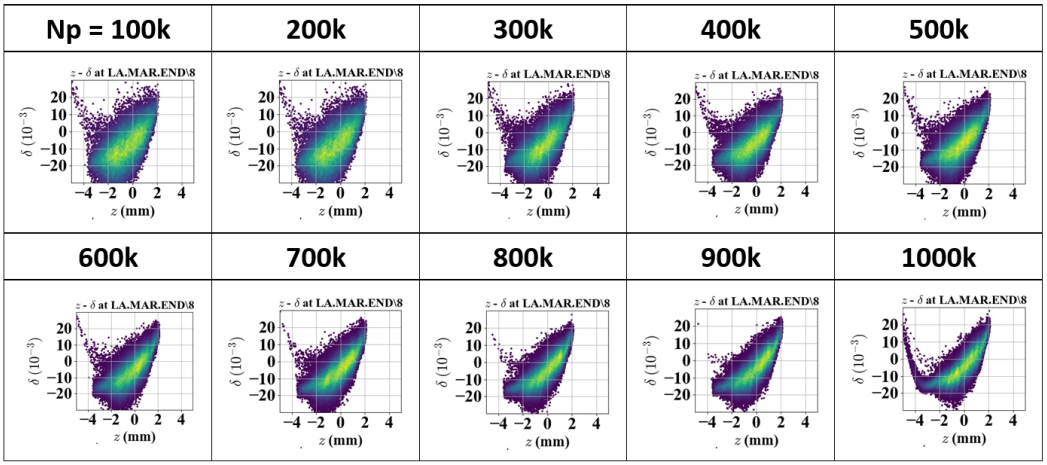

Figure 4.22: The longitudinal phase space distribution at the end of LINAC pass 8 for the 4-turn CSR simulation, with N_p ranging from 10^3 to 10^6.

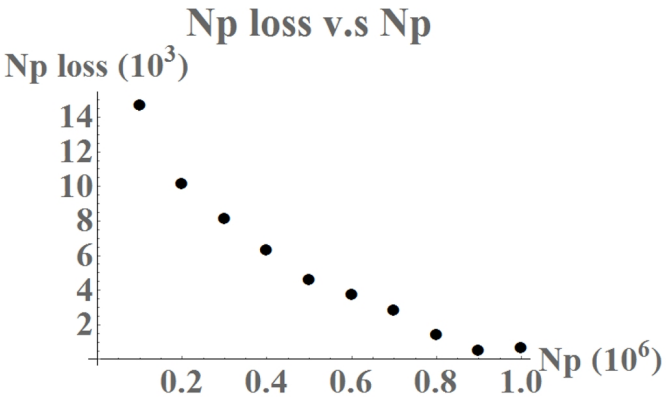

Figure 4.23: The total particle loss (out of 10^6) for the 4-turn CSR simulation, with N_p ranging from 10^3 to 10^6.

4.4.2 4-turn with varying N_b

The last subsection shows the convergence test on N_p, with N_b fixed at 2500. Here we instead vary N_b and fix N_p at 10^6. Fig. 4.25 shows the longitudinal phase space distribution recorded at the end of LINAC pass 8 (6 MeV) with N_b varying from 500 to 4000. Fig. 4.26 shows the corresponding change in the important physical quantities. Although the final energy spread is similar for different N_b, the number of particle loss increases from hundreds to almost four thousand

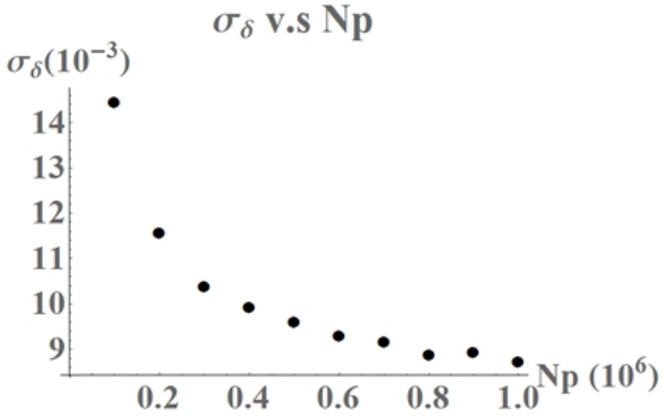

Figure 4.24: The final rms energy spread for the 4-turn CSR simulation, with N_p ranging from 10^3 to 10^6.

as N_b increases. As discussed before, a large N_b might increase numerical noise due to a decreased N_p per bin. Since one can not determine whether the extra particle loss is a numerical effect or due purely to CSR, it is difficult to determine the optimal choice of N_b in this case. More N_p might be required for a significant range of N_b to give physically equivalent results.

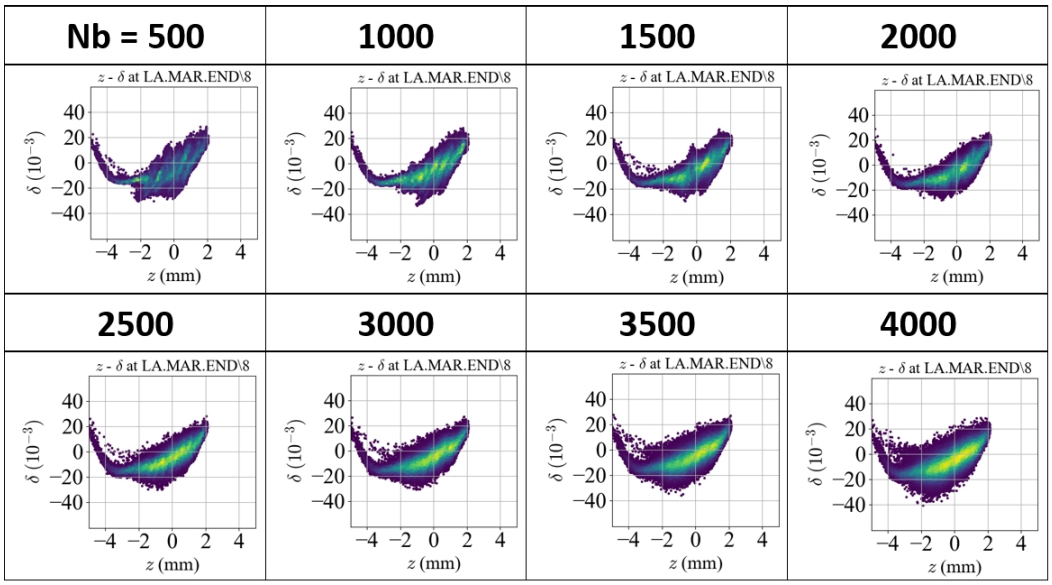

Figure 4.25: The longitudinal distribution at the end of LINAC pass 8 for the 4-turn CSR simulation, with N_b ranging from 500 to 4000.

Nb	500	1000	1500	2000	2500	3000	3500	4000
Np LOSS	265	315	528	407	658	1414	3082	3913
σ_x (mm)	1.46	1.26	1.26	1.28	1.42	1.56	1.72	1.97
σ_δ (E-3)	9.91	9.21	8.84	8.89	8.72	8.82	9.05	9.55
Max |δ| (%)	4.92	5.14	5.07	4.99	5.31	4.77	4.85	6.89

Figure 4.26: The important physical quantities corresponding to the results in 4.25.

4.4.3 4-turn with varying Q

Unlike N_p and N_b which are numerical parameters, the bunch charge Q is a physical parameter. One primary objective of CSR simulations is to determine the maximum allowed Q for CBETA.

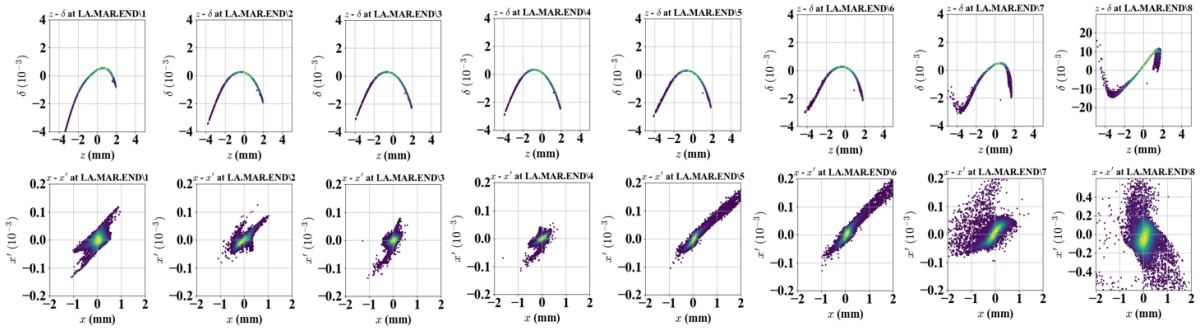

Figure 4.27: The $x - x'$ and $z - \delta$ distributions after each of the 8 LINAC passes for CBETA 4-turn with no CSR.

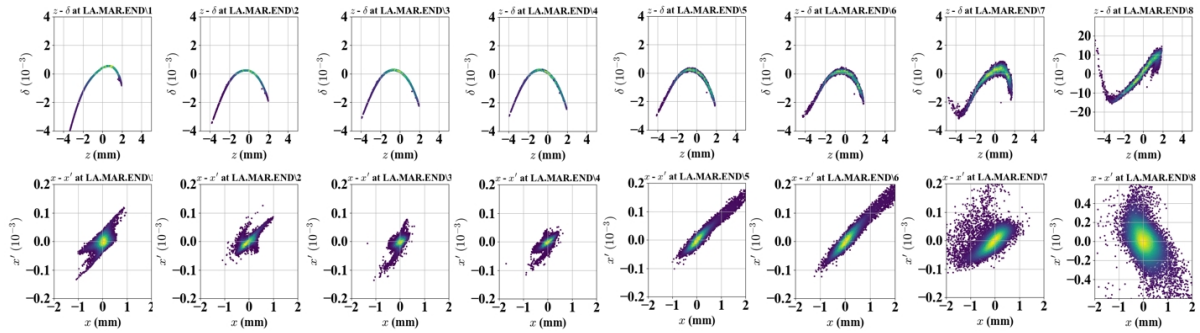

Figure 4.28: The $x - x'$ and $z - \delta$ distributions after each of the 8 LINAC passes for CBETA 4-turn with $Q = 1$ pC.

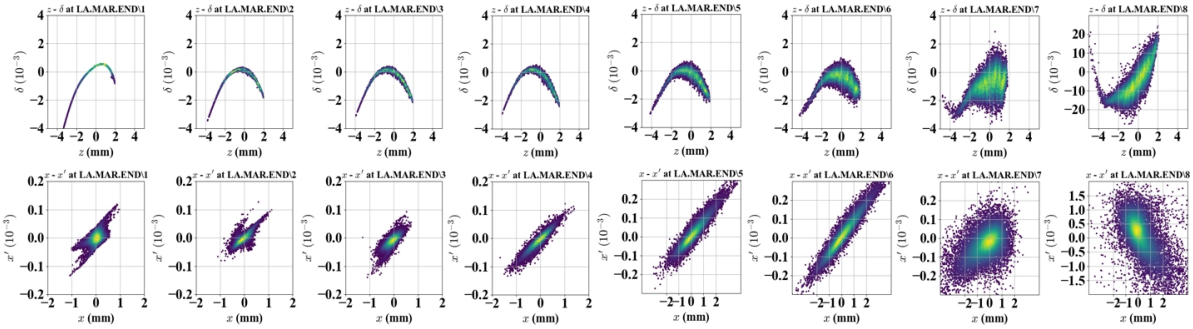

Figure 4.29: The $x - x'$ and $z - \delta$ distributions after each of the 8 LINAC passes for CBETA 4-turn with $Q = 5$ pC.

Fig. 4.27 shows the longitudinal and horizontal phase space distributions of the tracked bunch at the end of $each$ LINAC pass, from 1 to 8, with no CSR effects. Fig. 4.28 and Fig. 4.29 show the corresponding results with CSR effects, for $Q = 1$ pC and 5 pC respectively. As expected, both the energy spread and beam emittance increase as Q increases. Moreover, the energy spread builds up over the recirculation passes. Note that both x' and δ are dimensionless quantities normalized by the reference momentum of each pass, which explains why the spreads increase more severely during the four decelerating passes than the four accelerating passes.

For $Q = 1$ pC, 215 out of a 10^6 particles have been lost during the final two decelerating passes. However, all the surviving particles have a final energy spread of less than $\pm 7\%$, which is the acceptance limit of the CBETA beam stop assuming no halo and other undesired effects. For $Q = 5$ pC, 658 out of a 10^6 particles have been lost for N_b= 2500. As discussed in the previous subsection, the particle loss can come from numerical effects. These results show that, as long as the particle loss can be dealt with (potentially by varying beam optics in the splitter sections), it is promising for the 4-turn machine to reach its low design current of 1 mA, which requires $Q \geq 3$ pC at the maximum repetition

rate of 325 MHz. During the decelerating passes, micro-bunching structures can be seen in the longitudinal phase space. To what extent this is a physical or a numerical effect requires further study.

4.4.4 1-turn with varying Q

Fig. 4.30 shows the final longitudinal phase space distributions, where the beam has returned to 6 MeV, for different Q. Fig. 4.31 shows the corresponding particle loss and increase in energy spread. There is no particle loss up to $Q = 75$ pC, and all the surviving particles have an energy spread within the $\pm 7\%$ limit. With the maximum repetition rate of 1.3 GHz, this corresponds to a beam current of 97.5 mA, well exceeding the high design current of 40 mA. As Q further increases, the CSR effect becomes more significant, causing greater increase in energy spread and eventually significant beam loss.

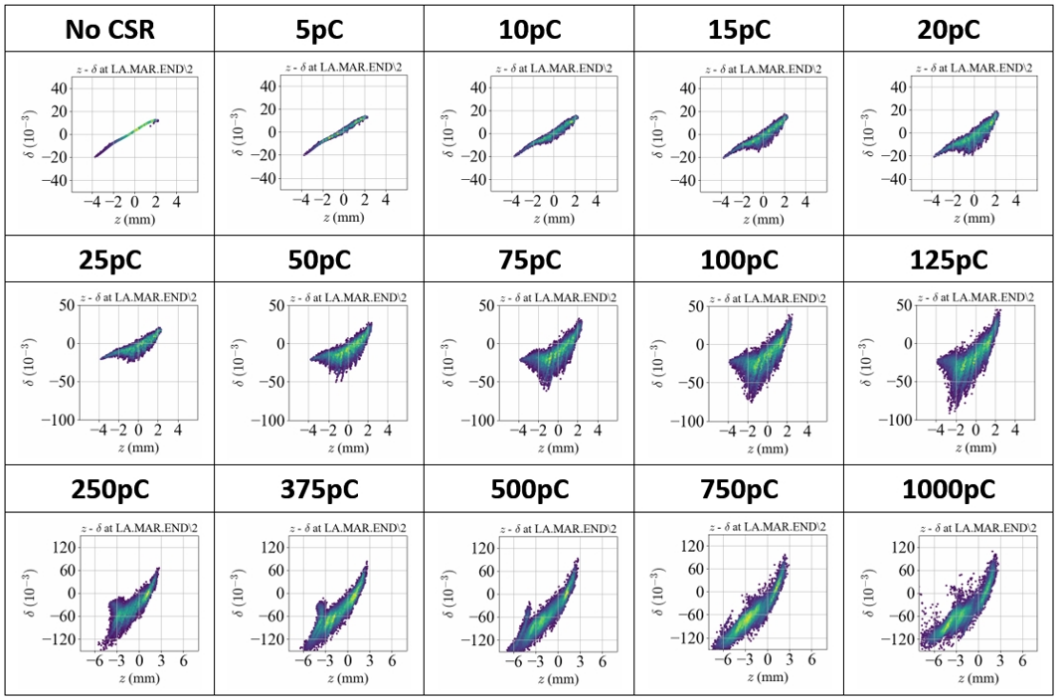

Figure 4.30: The $z - \delta$ distribution at the end of LINAC pass 2 for CBETA 1-turn with various Q.

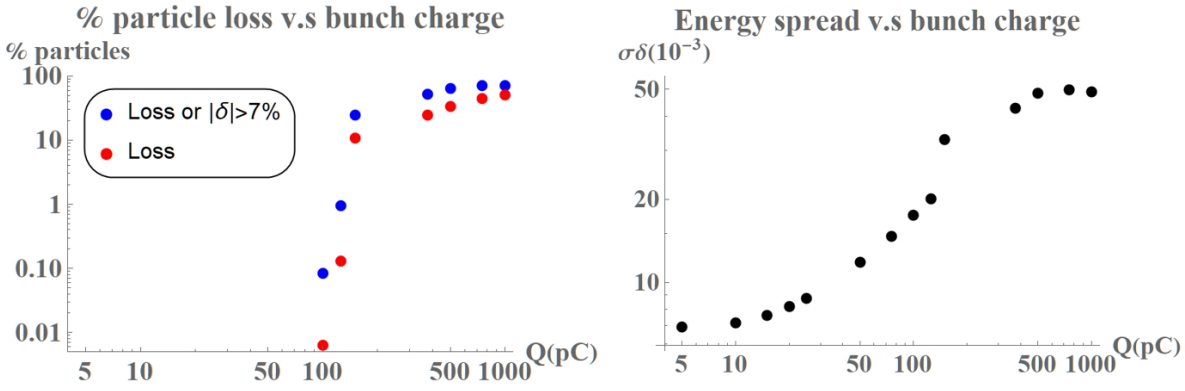

Figure 4.31: (color) The % particle loss (left, red dots) and the final rms energy spread (right) with Q ranging from 5 pC to 1000 pC. The blue dots indicate % particles with energy spread greater than $\pm 7\%$.

4.4.5 1-turn with varying Q, Gaussian beam

The purpose of tracking a Gaussian beam is to compare with the GPT beam results regarding potential microbunching effects. Fig. 4.32 shows the longitudinal phase space distributions of the tracked bunch at the end of LINAC pass 2 for different Q. Fig. 4.33 shows the corresponding particle loss and final energy spread.

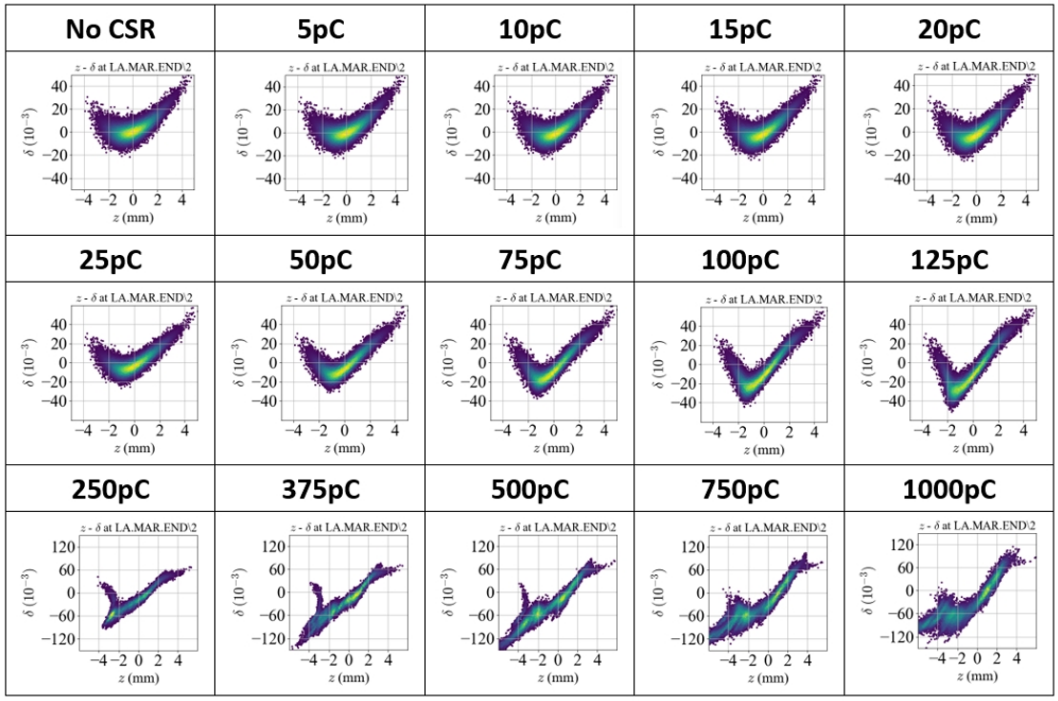

Figure 4.32: The $z - \delta$ distribution at the end of LINAC pass 2 for CBETA 1-turn with a Gaussian beam for various Q.

Comparison between Fig. 4.31 and Fig. 4.33 shows that the final energy spreads increases with Q in a similar way for both GPT and Gaussian beam. For Gaussian beam the particle loss occurs at $Q = 125$ pC, higher than the 75 pC for GPT beam. However a small fraction of the particles in Gaussian beam exceed the $\pm 7\%$ limit even at low Q (see the blue dots in Fig. 4.33), which is due likely to mismatched beam optics. At high Q the longitudinal microbunching

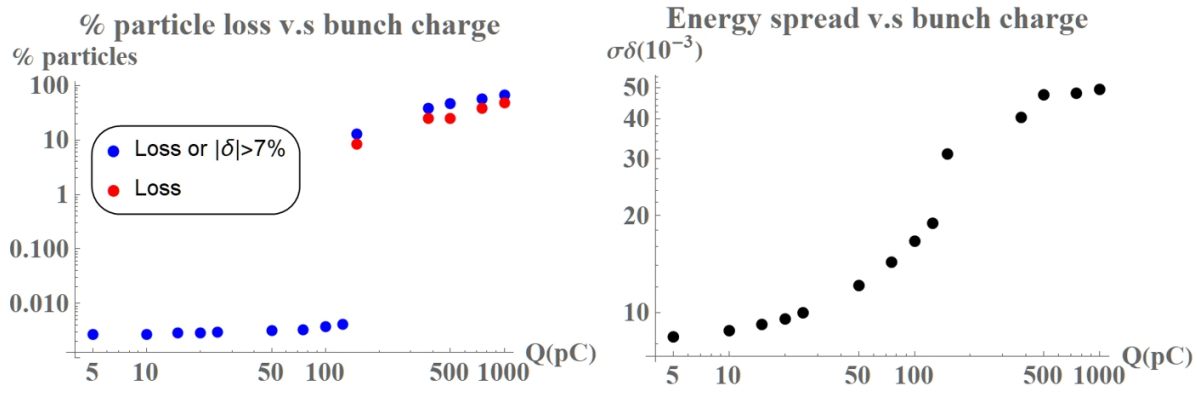

Figure 4.33: (color) The % particle loss (left, red dots) and the final rms energy spread (right) with a Gaussian beam, with Q ranging from 5 pC to 1000 pC. The blue dots indicate % particles with energy spread greater than $\pm 7\%$.

structure is significant for the GPT beam yet not for Gaussian beam. The structure likely comes from the initial microbunching structure of the GPT beam. The similarity in energy spreads between the two beams imply that microbunching instability is not driven by CSR severely to cause additional energy spread.

4.4.6 1-turn with varying bunch length, Gaussian beam

According to CSR theory, the characteristic CSR energy kick scales with longitudinal bunch length σ_z as $\sigma_z^{-4/3}$ (see Eq.(4.106)). This means a longer bunch length could reduce CSR effects, and simulations with varying σ_z are run to confirm this prediction. Both GPT beam and Gaussian beam used before this section has an initial σ_z of 1.0 mm. Fig. 4.34 shows the final longitudinal phase space distributions with a Gaussian beam for different σ_z at $Q = 250$ pC. Fig. 4.35 shows the corresponding % particle loss and final energy spread. As σ_z increases the beam distribution becomes less distorted, and for σ_z larger than 1.5 mm there is no longer particle loss. However the energy spread does not monotonically decrease as σ_z increases. The increasing energy spread for $\sigma_z > 2.0$ mm likely

comes from the extra RF curvature picked up during deceleration. Overall the results implies that increasing σ_z can greatly mitigate the CSR effects for CBETA 1-turn at least up to $Q = 250$ pC.

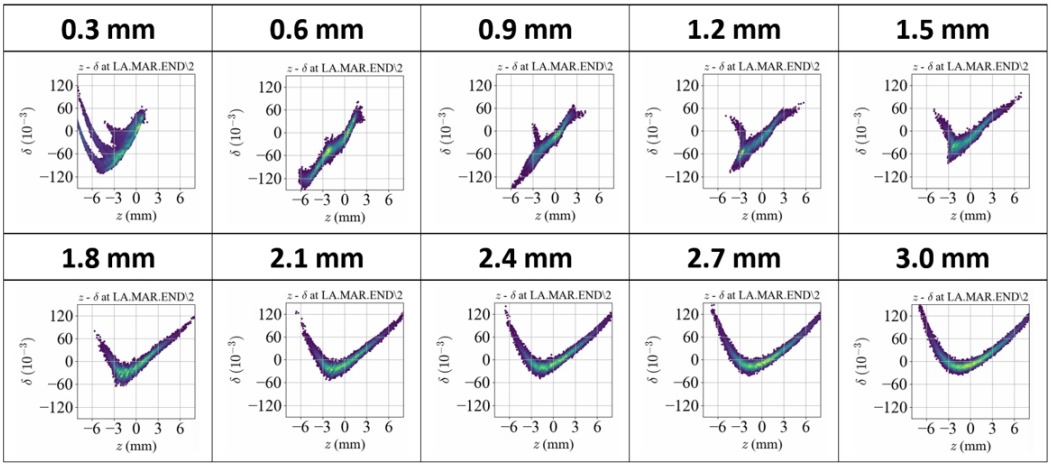

Figure 4.34: The final $z - \delta$ distribution for CBETA 1-turn with various σ_z.

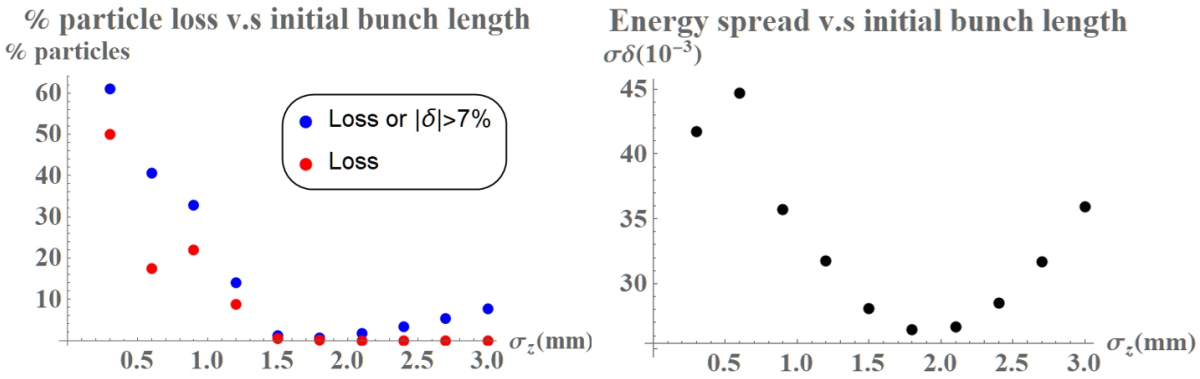

Figure 4.35: (color) The % particle loss (left, red dots) and the final rms energy spread (right) with σ_z ranging from 0.3 mm to 3.0 mm. The blue dots indicate % particles with energy spread greater than $\pm 7\%$.

4.4.7 Conclusion

The ultra-relativistic CSR wake expressions with one bending magnet formulated in [22] and [23] have been rederived and extended to a system with two

bending magnets, and can now be applied for the case when the wake from the first magnet leaks into the second magnet. This can occur to beamlines with magnets placed close to each other, such as the FFA beamline of CBETA. We show that the new terms for wake leakage from one magnet to the next are very relevant. The derived formulas have been compared with Bmad CSR simulation, and agreements have been observed.

Bmad CSR simulations have been run for the CBETA 1-turn and 4-turn lattice, and increase in energy spread with the bunch charge and the number of recirculation passes have been observed. For the 1-turn mode the bunch charge can be raised up to 75 pC without particle loss or severe increase in the energy spread. For the 4-turn mode at 5 pC, there is less than 0.1% particle loss, but the energy spread is acceptable. More convergence tests on the CSR numerical parameters are required to study whether the particle loss is a numerical or physical effect. Mitigation to the CSR effects including increasing the bunch length and introducing metal shielding have been proposed. While the former has been simulated and gives promising results, the latter requires significant computational power.

CHAPTER 5

ORBIT CORRECTION AND TOLERANCE STUDY

Besides BBU and CSR, additional work has been performed to study the optical tolerance of the CBETA lattice under various random errors. The goal here is to calculate above what error magnitude the beam emittance becomes unacceptable even after multipass orbit correction.

5.1 FFA Orbit Correction Example

This section describes an example of Bmad correcting the FFA orbits using SVD optimization with a set of random quadrupole field error introduced to all the FFA magnets. The details on how SVD optimization works can be found in [35], and are not covered here. The top half of Fig. 5.1 shows the distorted orbits when all the FFAG quadrupole magnets incur a 0.5% Gaussian random error in their b1 gradient. Clearly the orbits are distorted, and becomes non-periodic in FA and non-zero in ZA. The bottom half of Fig. 5.1 shows the recovered orbits after correction using all the horizontal correctors.

The recovered orbits are not the same as the design orbits for two main reasons. First, the orbit correction algorithm can fix the orbits only at the location of BPMs, and is insensitive to orbit distortions $between$ the BPMs. Second, for each FFA cell there are 4 horizontal orbit values to correct, yet only one horizontal corrector to vary (same for the vertical orbits). This means the system is mathematically over-constrained, and the orbits cannot be fully corrected back to zero residues in general. Besides introducing extra correctors, one way to improve the correction results is to assign relative weights to the correctors [35].

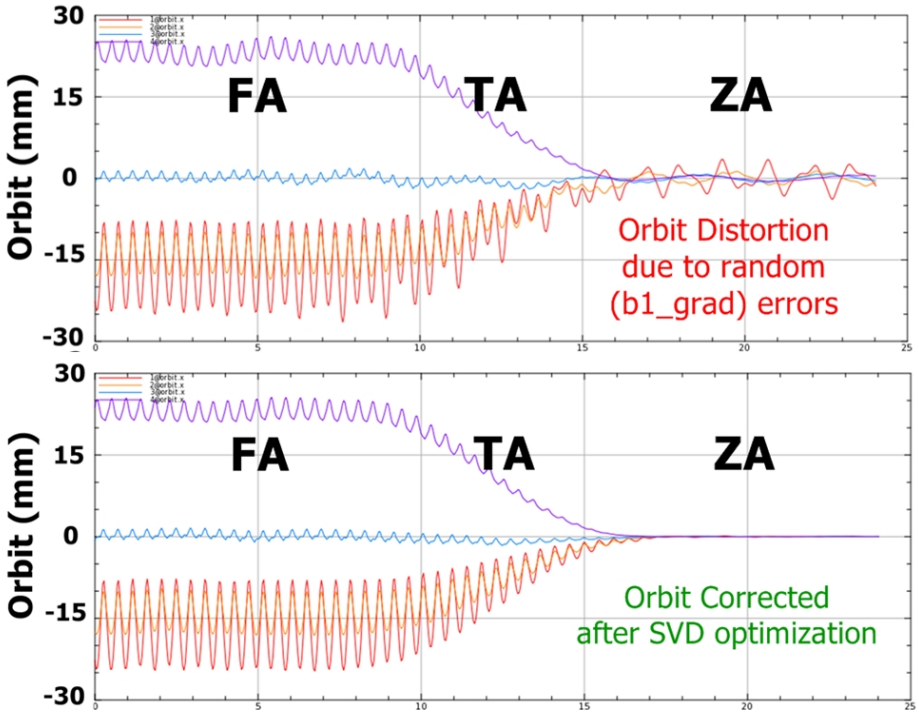

Figure 5.1: The top half shows the orbit distortion with all FFA quad magnets subjected to a 0.5% Gaussian random error in their b1 gradient. The bottom half shows the recovered orbits after SVD orbit correction.

This method involves further study in the SVD optimization.

5.2 Result statistics

For the rest of this chapter, the orbit correction process to a particular assignment of errors, like the example shown in the last section, is referred to as "one simulation". To determine the tolerance of the lattice subjected to certain error, many simulations are required to obtain representative statistics. Fig. 5.2 illustrates the general procedure to study the tolerance of a particular error source, and Fig. 5.3 describes the procedure in details, including the numerical definition of "individual limit".

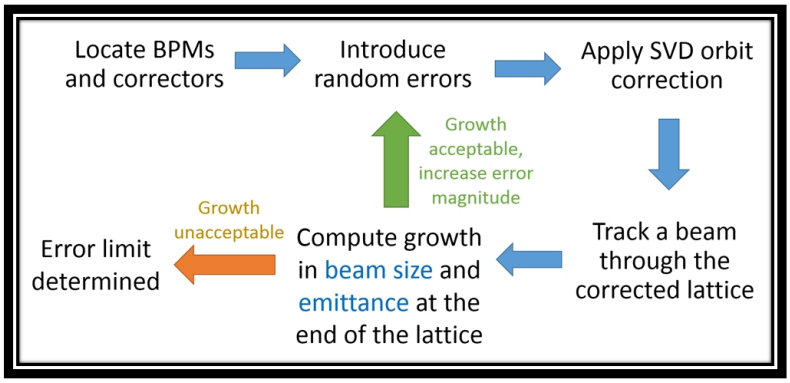

Figure 5.2: A schematic diagram to determine the tolerance of a lattice under particular error source(s).

(1) Choose a type of error(s)
(2) Choose a (reasonable) error magnitude
(3) Introduce random errors (Gaussian distribution) to the FFAG quads
(4) Decide which BPMs and correctors are to be used (usually all of them)
(5) Run the SVD optimizer to correct the orbit
(6) Track a beam through the lattice and record the X/Y emittance and beam_size at the end element (if no particle lost)
(7) Repeat (3) to (5) N times to calculate **"μ + 1σ"** in X/Y emittance/beam_size.
(μ + 1σ characterizes how bad emittance/beam_size could increase to)
(N>50 required for good statistics)
(8) Repeat (2) to (7) with different error magnitudes.
(9) Determine at which magnitude is any of the four "μ + 1σ" 10% greater than that of the no-error case. This is the **individual limit** of this error type.

Figure 5.3: The detailed procedures to determine the individual limit of a particular error.

For a chosen error type and magnitude we run N=100 simulations to obtain a statistically representative "$\mu+1\sigma$" (See Fig. 5.3 for details). We call this quantity the "1σ increase" in X (or Y) emittance (or beam size). Fig. 6 shows that the 1σ increase in X emittance of the 42 MeV beam grows with the error magnitude of b1 gradient. At 0.66% error in b1 gradients, the 1σ increase in X emittance reaches 10%. However, we also need to check the growth in the Y emittance and transverse beam sizes. Table 5.1 summarizes the required error magnitude

for each 1σ increase to hit 10%. It turns out that the 1σ increase in Y beam size reaches 10% at 0.27% error in b1 gradient, earlier than the other three quantities. So the individual limit of b1 gradient error, by our definition, is 0.27%.

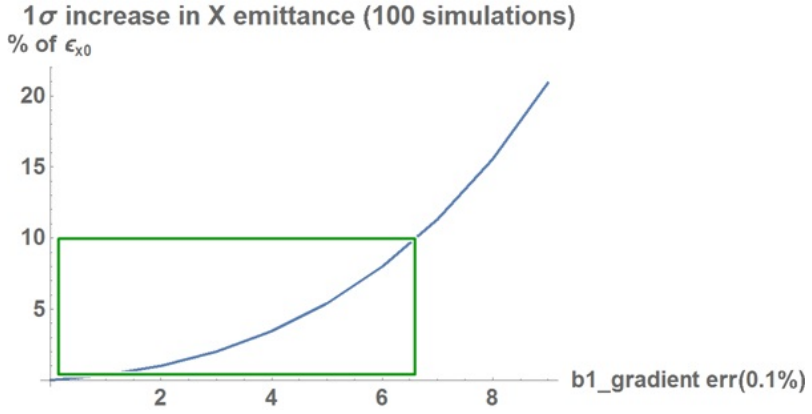

Figure 5.4: The growth of 1σ increase in X emittance of the 42 MeV beam as the error magnitude in b1 gradient increases. The green rectangle shows that 10% increase is reached when b1 gradient magnitude hits 0.66%.

Quantity (42 MeV beam)	Error magnitude in b1 gradient to hit 10% 1σ increase
X emittance	0.66%
Y emittance	0.90%
X beam size	0.37%
Y beam size	0.27%

Table 5.1: The tolerance of the FFA beamline subjected to b1 gradient error.

Note that these individual limits for FFA change if we look at the beam at a different design energy. We choose the 42 MeV beam because a lower energy beam is more subjected to field errors. However, as described before, all four orbits are accounted for during orbit correction. Since the beam only experiences dipole and quadrupole fields in the FFA beamline, one might wonder why the beam emittances increase as field error increases, even after correction. The reason is that orbit correction schemes implemented so far only fix the orbits, not

the beam optics and dispersion. Since the beam has an energy spread, the uncontrolled dispersion function due to field errors causes increase in emittances and beam sizes.

5.3 Individual limits of Various error types

Similar to the b1 gradient error, 100 simulations were run to find out the individual limit of other error types. Table 5.2 shows the individual limits of a few common error sources. All these limits are above the design specification of CBETA, implying great tolerance of the design lattice.

Error Type		Individual limit
FFAG Magnets	Gradient	0.27%
	X offset	0.5 mm
	Y offset	> 0.5 mm
	tilt	6.5 mrad
BPM reading error		0.2 mm

Table 5.2: The individual limit of common error types for the FFA beamline.

It's also important to find out the tolerance for higher order multipole fields, defined in Bmad as:

$$B_x + iB_y = \frac{b_n + ia_n}{L}(x + iy)^n, \tag{5.1}$$

in which b_n and a_n are the strength of normal and skew multipole fields for $n \geq 2$. For instance, b_1 is the normal quadrupole gradient, and a_2 is the skew

sextuple field strength. L is the length of the magnet, and x and y are measured from the pipe center. For physically meaningful comparison, we normalize the multipole strengths using a dimensionless unit u_0:

$$b_n = \left[10^{-4}\frac{GL}{r_0^{n-1}}\right] u_0, \tag{5.2}$$

in which G is the quadrupole gradient of either QF or BD, and r_0 is chosen to be 25 mm (about the extent of the highest and lowest energy orbit from the pipe center). Table 5.3 shows the individual limit of all the normal and skew multipoles for the FFA beamline, reported in u_0.

Normal multipole	Individual limit (u_0)	Skew multipole	Individual limit (u_0)
b2	37	a2	140
b3	30	a3	90
b4	26	a4	80
b5	21	a5	65
b6	21	a6	63
b7	19	a7	58
b8	21	a8	56
b9	18	a9	53

Table 5.3: The individual limit of normal and multipole up to 20-pole, reported in the normalized unit u_0.

5.4 Combined limit of multipole field errors

In reality multiple sources of errors coexist, and the individual limits are insufficient to capture the combined effect. Therefore we need a define a statistically meaningful "combined limit". For now we consider just the 16 multipole field errors in table 5.3. In the simulation we assign each FFA magnet a 16-vector:

$$\mathbf{v} = \left(\frac{b_n}{\text{lim\_}b_n}, \frac{a_n}{\text{lim\_}a_n}\right), n = 2, 3...9, \tag{5.3}$$

in which lim_b_n and lim_a_n are the individual limits from table 5.3 which serve as relative weightings between the multipoles. The value of each element in **v** is chosen randomly from the normal Gaussian distribution ($\mu = 0, \sigma = 1$). Since there are 16 errors present, the combined error must be scaled down properly. A number u is chosen randomly from the uniform distribution $(0, 1]$, and the magnitude of **v** is scaled down to be $u^{(1/16)}$. This allows **v** to point at a uniformly random point in the 16-D hyper-sphere with radius one. We further introduce a unitless quantity "error scale" which scales all the elements in **v** by the same factor. By definition, the magnitude of **v** also scales by the same factor, so we can use the magnitude as a measure of the combined error.

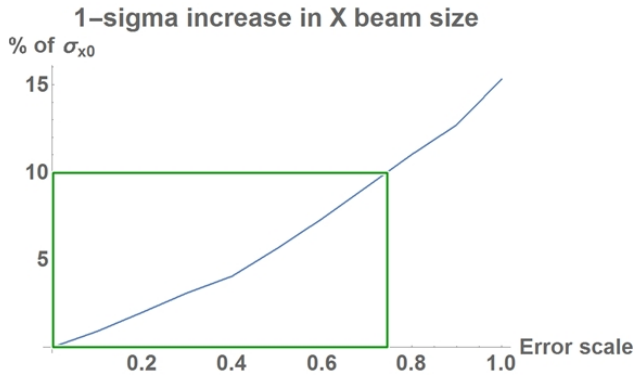

Figure 5.5: The growth of 1σ increase in X beam size as the combined error scale of 16 multipoles increases. The green rectangle shows that 10% increase is reached when the error scale hits 0.75%.

Fig. 5.5 shows the 1σ increase in X beam size grows with the error scale increases from 0 to 1 at a step of 0.1. For each error scale, 1000 simulations were run to obtain representative statistics. At an error scale of 0.75, 1σ increase in X beam size reaches 10%, earlier than the other three quantities of interest. So the combined limit for FFA multipole field error is reported as:

$$\sqrt{\Sigma_n \left(\frac{b_n}{\text{lim\_}b_n}\right)^2 + \left(\frac{a_n}{\text{lim\_}a_n}\right)^2} < 0.75. \tag{5.4}$$

The tolerance studies provides a quantitative figure of merit for the actual components in the accelerators. For instance, Fig. 5.6 shows the measured combined multipole error of 214 manufactured FFA magnets before and after tuning [36]. The average error scale is 0.094 after tuning, which is well below the simulated tolerance of 0.75. This indicates acceptable field quality along the FFA beamline.

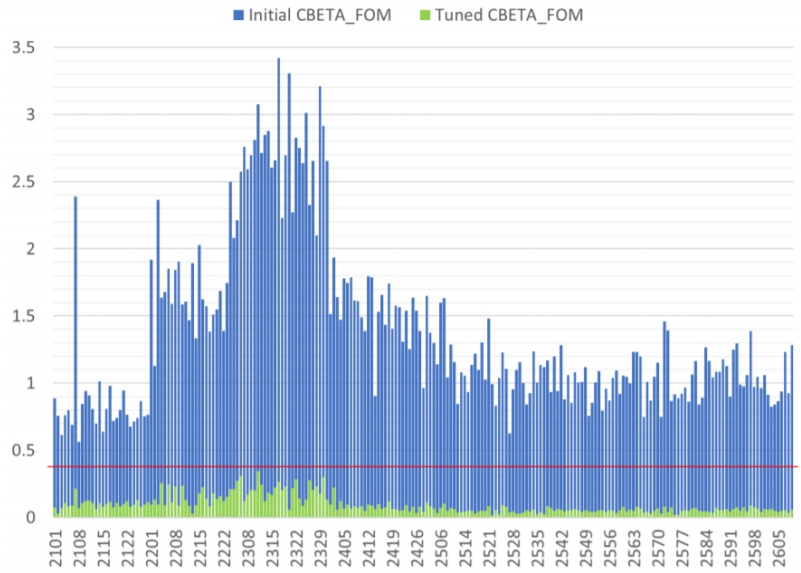

Figure 5.6: (Color) Measured combined multipole error (i.e. magnitude of the vector **v** in Eq. 5.3) of 214 FFA magnets before and after tuning. The errors reduce significantly after tuning (green bars). The red line indicates an error of 0.375, half of the simulated tolerance of 0.75.

5.5 Future studies

Tolerance studies with other orbit correction schemes can still be performed for the CBETA lattice. One important proposal is to use the entire 4-turn lattice with one design orbit, instead of using only the FFA beamline with four independent orbits. Although this better simulates the reality, it generally makes optimiza-

tion computationally more intensive. For instance, each BPM in the FFA beamline would have, instead of four, $seven$ orbit readings to be corrected, which constrain the system even more. Since errors propagate from early passes to later passes, it is recommended to correct the orbit sections by sections. This has been performed in reality when CBETA operators manage to guide the beam through the sections. Correctors in the splitter sections are particularly useful in this procedure since they affect the orbit of each pass more independently.

APPENDIX A

DERIVED FORMULAS FOR THE 2-BEND CSR THEORY

The two tables below summarizes the important formulas derived in the four odd cases and four even cases in the CSR chapter.

Case	$A(\times 4ke^2)$	y_p	$\Delta(y=y_p)$	$W(s)$
A	$1/(R\theta)$	$\frac{1}{2}\gamma R\theta^2$	$\frac{1}{6}R\theta^3$	$A\times\lambda\left(s-\Delta(y=y_p)\right)$
C	$1/(R\phi+2x)$	$\frac{1}{2}\gamma(R\phi+2x)\phi$	$\frac{1}{6}(R\phi+3x)\phi^2$	
E	$(\phi_1\pm\theta_2)/(R_1\phi_1^2+2x\phi_1$ $+2R_2\phi_1\theta_2\pm R_2\theta_2^2)$	$\frac{1}{2}\gamma(R_1\phi_1^2+2x\phi_1$ $+2R_2\phi_1\theta_2\pm R_2\theta_2^2)$	$\frac{1}{6}[(R_1\phi_1+3x)\phi_1^2$ $+R_2\theta_2(3\phi_1^2\pm 3\phi_1\theta_2+\theta_2^2)]$	
G	$(\phi_1\pm\phi_2)/(R_1\phi_1^2+2x\phi_1$ $+2R_2\phi_1\phi_2\pm R_2\phi_2^2+2x_2(\phi_1\pm\phi_2))$	$\frac{1}{2}\gamma(R_1\phi_1^2+2x\phi_1+2R_2\phi_1\phi_2$ $\pm R_2\phi_2^2+2x_2(\phi_1\pm\phi_2))$	$\frac{1}{6}[(R_1\phi_1+3x)\phi_1^2+R_2\phi_2(3\phi_1^2$ $\pm 3\phi_1\phi_2+\phi_2^2)+3x_2(\phi_1\pm\phi_2)^2]$	

Table A.1: The normalization factor A, the y_p which approximately maximizes $w(y)$, and the wake expression $W(s)$ for odd cases. The "$\pm$" sign indicates "$+$" if the two magnets bend in the same direction, and "$-$" if opposite. Note that the expressions for $W(s)$ can only be applied if the drift length before the (first) magnet is much longer than y_p.

Case	$u(\times 4ke^2)$	Boundary term(s) of $W(s)$	Integral term of $W(s)$
B	$1/(R\theta)$	$-u(\theta=\theta_{\max})\lambda(s-\Delta_{\max})$	$-\int_{s-\Delta_{\max}}^{s-\Delta_{\min}} u\frac{\partial\lambda(s')}{\partial s'}ds'$
D	$1/(R\theta+2x)$	$-u(\theta=\phi)\lambda(s-\Delta_{\max})$	
F	$\frac{(\theta_1\pm\theta_2)}{R_1\theta_1^2+2x\theta_1\pm 2R_2\theta_1\theta_2\pm R_2\theta_2^2}$	$u(\theta_1=0)\lambda(s-\Delta_{\min})$ $-u(\theta_1=\phi_1)\lambda(s-\Delta_{\max})$	
H	$\frac{(\theta_1\pm\phi_2)}{R_1\theta_1^2+2x\theta_1\pm 2R_2\theta_1\phi_2\pm R_2\phi_2^2+2x_2(\theta_1\pm\phi_2)}$		

Table A.2: The function u and the wake expression $W(s)$ for even cases. Note that for case B and D there is one boundary term, and for case F and H there are two boundary terms (the near one at $\theta_1=0$ and the far one at $\theta_1=\phi_1$).

BIBLIOGRAPHY

[1] G. H. Hoffstaetter, D. Trbojevic, C. Mayes, N. Banerjee, J. Barley, I. Bazarov, A. Bartnik, J. S. Berg, S. Brooks, D. Burke, *et al.*, arXiv:1706.04245.

[2] R. Milner (ed.), Roger Carlini (ed.), Frank Maas (ed.), *Proceedings, Workshop to Explore Physics Opportunities with Intense, Polarized Electron Beams up to 300 MeV*, (AIP Conference Proceedings: Cambridge, USA, 2013).

[3] D. Androic, D. S. Armstrong, A. Asaturyan, T. Averett, J. Balewski, J. Beaufait, R. S. Beminiwattha, J. Benesch, F. Benmokhtar, J. Birchall, *et al.*, arXiv:1307.5275.

[4] F. Albert, S. G. Anderson, D. J. Gibson, R. A. Marsh, S. S. Wu, C. W. Siders, C. P. J. Barty, and F. V. Hartemann, Phys. Rev. ST Accel. Beams, Vol. 14, 050703 (2011).

[5] D. Trbojevic, S. Bellavia, M. Blaskiewicz, S. Brooks, K. Brown, C. Liu, W. Fischer, C. Franck, Y. Hao, G. Mahler *et al. CBETA - Cornell University Brookhaven National Laboratory Electron Energy Recovery Test Accelerator*, (Proceedings, 8th International Particle Accelerator Conference (IPAC2017): Copenhagen, Denmark, 2017) TUOCB3.

[6] K.E. Deitrick *et al.*, *STATUS OF THE CBETA CORNELL-BNL ERL PROTOTYPE*, (Proceedings, North American Particle Accelerator Conference (NAPAC2019): Lansing, MI, USA, 2019) THYBA1.

[7] G. H. Hoffstaetter, I.V. Bazarov, Phys. Rev. ST Accel. Beams, Vol. 7, 054401 (2004).

[8] D. Sagan, *Bmad Simulation Software*, `https://www.classe.cornell.edu/bmad/`

[9] N. Valles, Ph.D., Cornell University (2014), `https://www.classe.cornell.edu/rsrc/Home/Research/GradTheses/Valles_Nicholas.pdf`

[10] D.G. Myakishev and V. P. Yakovlev, *CLANS2 - a code for Calculation of Multipole Modes in Axisymmetric Cavities with Absorber Ferrites*, (Proceedings of the 1999 Particle Accelerator Conference (PAC1999), pages 2775-2777: New York, 1999)

[11] W. Lou, G. H. Hoffstaetter *Beam-Breakup Studies for the 4-pass Cornell-Brookhaven Energy-Recovery Linac Test Accelerator*, (Proceedings, 9th International Particle Accelerator Conference (IPAC2018): Vancouver, Canada, 2018) THPAF022.

[12] R. Rand, T. Smith, Particle Accelerator, Vol. 2, 1 (1980).

[13] C. D. Tennant, K. B. Beard, D. R. Douglas, K. C. Jordan, L. Merminga, E. G. Pozdeyev, T. I. Smith. Phys. Rev. ST Accel. Beams, Vol. 8, 074403 (2005).

[14] D. R. Douglas, K. C. Jordan, L. Merminga, E. G. Pozdeyev, C. D. Tennant, H. Wang, T. I. Smith, S. S. Simrock, I. V. Bazarov, G. H. Hoffstaetter, Phys. Rev. ST Accel. Beams, Vol. 9, 064403 (2006).

[15] R. Kazimi, *et al.*, *Observation and Mitigation of Multipass BBU in CEBAF*, (Proceedings, 11th European Conference, EPAC 2008, Genoa, Italy, 2008), WEPP087.

[16] V. N. Litvinenko, Phys. Rev. ST Accel. Beams, Vol. 15, 074401 (2012).

[17] G. H. Hoffstaetter, I. V. Bazarov, C. Song, Phys. Rev. ST Accel. Beams, Vol. 10, 044401 (2007).

[18] V. Volkov, J. Knobloch, A. Matveenko, Phys. Rev. ST Accel. Beams, Vol. 14, 054202 (2011).

[19] B. C. Yunn, Phys. Rev. ST Accel. Beams, Vol. 8, 104401 (2005).

[20] E. Pozdeyev, Phys. Rev. ST Accel. Beams, Vol. 8, 054401 (2005).

[21] J. Rosenzweig, L. Serafini, Phys. Rev. E, Vol. 49, 1599 (1994).

[22] E. L. Saldin, E. A. Schneidmiller, and M. V. Yurkov, Nucl. Instrum. Methods Phys. Res., Sect. A 398, 373 (1997)

[23] G. Stupakov and P. Emma, *CSR Wake for a Short Magnet in Ultrarelativistic Limit* (Proceedings, 8th European Particle Accelerator Conference (EPAC2002), Paris, France, 2002).

[24] C.-Y. Tsai, S. Di Mitri, D. Douglas, R. Li, and C. Tennant Phys. Rev. Accel. Beams 20, 024401 (2017).

[25] J. D. Jackson, Classical Electrodynamics, 3rd ed., Wiley, New York, p. 678 (1999)

[26] D. Sagan *et al.*, Phys. Rev. ST Accel. Beams 12, 040703 (2009).

[27] D. Sagan and C.Mayes, *Coherent Synchrotron Radiation Simulation for off-axis beams using Bmad toolkit*, (Proceedings, 8th International Particle Accelerator Conference (IPAC2017): Copenhagen, Denmark, USA, 2017) THPAB076.

[28] C. Mayes and G.H. Hoffstaetter, Phys. Rev. ST Accel. Beams 12, 024401 (2009).

[29] W. Lou, G. H. Hoffstaetter, D. Sagan, C. Mayes *CSR Phase Space Dilution in CBETA*, (Proceedings, North American Particle Accelerator Conference (NAPAC2019): Lansing, MI, USA, 2019) WEXBA3.

[30] W. Lou, A. Bartnik, J. A. Crittenden, C. Gulliford, G. H. Hoffstaetter, D. Sagan, J. S. Berg, S. Brooks, F. Meot, D. Trbojevic, N. Tsoupas *The Beam Optics of the FFAG Cell of the CBETA ERL Accelerator*, (Proceedings, 8th International Particle Accelerator Conference (IPAC2018): Vancouver, Canada, 2018) THPAF023.

[31] I. Bazarov and Tsukasa Miyajima *Calculation of Coherent Synchrotron Radiation in General Particle Tracer*, (Proceedings, 11th European Particle Accelerator Conference (EPAC2008), Genoa, Italy, 2008)

[32] V. Yakimenko *et al.*, PRL 109, 164802 (2012).

[33] C.-Y. Tsai and R. Li, Simulation of coherent synchrotron radiation induced microbunching gain using ELEGANT, Report No. JLAB-TN-14-016.

[34] N. Banerjee, G. Hoffstaetter, M. Liepe, P. Quigley, Z. Zhou, arXiv:1902.05122.

[35] A. Ballado, Analysis and Optimization of Singular Value Decomposition Orbit Correction Schemes,
`https://www.classe.cornell.edu/rsrc/Home/StudentOpportunities/ReuReports2010/Ballado_report.pdf`

[36] S. Brooks, CBETA Halbach Magnet Production Run, CBETA machine note #35.